Synthesis of Organic Layer-Coated Metal Nanoparticles in a Dual-Plasma Process

Cao Qin

Department of Chemical Engineering
McGill University, Montréal

Dr. Sylvain Coulombe, Supervisor

A thesis submitted to McGill University in partial fulfillment of the requirements of the degree of Doctor of Philosophy

McGill University
Montréal, Canada

September 2007

Library and
Archives Canada

Published Heritage
Branch

395 Wellington Street
Ottawa ON K1A 0N4
Canada

Bibliothèque et
Archives Canada

Direction du
Patrimoine de l'édition

395, rue Wellington
Ottawa ON K1A 0N4
Canada

Your file Votre référence
ISBN: 978-0-494-38630-9
Our file Notre référence
ISBN: 978-0-494-38630-9

NOTICE:
The author has granted a non-exclusive license allowing Library and Archives Canada to reproduce, publish, archive, preserve, conserve, communicate to the public by telecommunication or on the Internet, loan, distribute and sell theses worldwide, for commercial or non-commercial purposes, in microform, paper, electronic and/or any other formats.

The author retains copyright ownership and moral rights in this thesis. Neither the thesis nor substantial extracts from it may be printed or otherwise reproduced without the author's permission.

AVIS:
L'auteur a accordé une licence non exclusive permettant à la Bibliothèque et Archives Canada de reproduire, publier, archiver, sauvegarder, conserver, transmettre au public par télécommunication ou par l'Internet, prêter, distribuer et vendre des thèses partout dans le monde, à des fins commerciales ou autres, sur support microforme, papier, électronique et/ou autres formats.

L'auteur conserve la propriété du droit d'auteur et des droits moraux qui protège cette thèse. Ni la thèse ni des extraits substantiels de celle-ci ne doivent être imprimés ou autrement reproduits sans son autorisation.

In compliance with the Canadian Privacy Act some supporting forms may have been removed from this thesis.

While these forms may be included in the document page count, their removal does not represent any loss of content from the thesis.

Conformément à la loi canadienne sur la protection de la vie privée, quelques formulaires secondaires ont été enlevés de cette thèse.

Bien que ces formulaires aient inclus dans la pagination, il n'y aura aucun contenu manquant.

Canada

Résumé

Un procédé innovateur faisant usage de deux sources à plasmas pour effectuer la synthèse de nanoparticules métalliques recouvertes d'une couche organique est présenté. Les nanoparticules métalliques sont générées en évaporant la surface d'une cathode métallique au moyen d'un arc pulsé opérant à basse pression. Ensuite, une fine couche organique est déposée en vol sur la surface des particules par polymérisation plasma d'un hydrocarbure monomérique gazeux dans un plasma soutenu par couplage radio-fréquentiel (RF) capacitif. Le système est simple d'opération et peut être optimisé pour augmenter le taux de production. La combinaison des procédés de synthèse et de traitement de surface des nanoparticules métalliques empêche la contamination des particules métalliques par l'environnement ambiant.

Une source de tension pulsée auto-oscillante a été construite pour le procédé d'évaporation par arc de la cathode métallique. La stabilité du système à arcs pulsés et le taux d'érosion de la cathode sont discutés. L'inductance présente dans la boucle de décharge a un effet stabilisant sur la continuité des arcs. Il a été démontré que le taux d'érosion dépend fortement du courant d'arc puisque davantage de macroparticules sont émises à fort courant; l'effet du courant d'arc est moins important au niveau du rendement en nanoparticules.

Les nanoparticules de cuivre recouverte d'une couche organique déposée dans un plasma d'argon/éthane (Ar/C_2H_6) ont été caractérisées par microscopie électronique à balayage (acronyme anglais *FE-SEM*) et à transmission (acronyme anglais *TEM*), par spectroscopie infra-rouge (acronyme anglais *FT-IR*) et par spectroscopie photo-électronique par rayon X (acronyme anglais *XPS*). Il a été découvert que les nanoparticules ont un cœur métallique ayant un diamètre de moins de 50 nm et que l'épaisseur de la couche organique varie de 3 à 10 nm. Les plus petites nanoparticules ont une structure cristalline alors que le recouvrement organique a une structure macromoléculaire à comportement hydrophobe. Les résultats XPS ont démontré que la couche mince générée par polymérisation plasma est adsorbée chimiquement sur la surface des nanoparticules de cuivre.

Les effets des conditions d'opération du réacteur, telles la pression et le débit de gaz inerte, sur la grosseur moyenne des nanoparticules de cuivre non-recouvertes ont été étudiés. Il a été démontré qu'il y a une dépendence directe entre la pression dans le réacteur et le diamètre des nanoparticules, et ce, peu importe le débit de gaz inerte.

Il a été découvert que la morphologie de la couche organique dépend fortement de la puissance dissipée dans le plasma RF, de la pression de la chambre et du débit de gaz inerte. Deux types de couche organique ont été produits : un film polymérique dense, uniforme et lisse et un film de polymère liquide. Suite à plusieurs expériences, une « carte caractéristique » pour la polymérisation par plasma en vol au moyen du monomère C_2H_6 sur des nanoparticules du cuivre a été élaborée. Un mécanisme simplifié à base de radicaux libres est proposé pour la polymérisation par plasma à l'aide de l'éthane.

D'autres métaux, tels le fer et l'aluminium, ont été utilisés comme cathode. Les analyses par TEM ont confirmé la production de nanoparticules recouvertes d'une couche et ayant une morphologie semblable au particules produites à l'aide de la cathode de cuivre. Finalement, des vapeurs d'éthylène glycol ont été introduites dans la région de polymérisation par plasma à titre d'alternative à l'éthane comme source de monomères. Une couche non-uniforme a été observée sur la surface des nanoparticules métalliques.

Abstract

A novel dual-plasma process for the synthesis of organic layer-coated metal nanoparticles is presented. Metal nanoparticles are synthesized by the low-pressure pulsed arc evaporation of a metal cathode surface, followed by the in-flight deposition of a thin organic layer by capacitively-coupled radio-frequency (CCRF) plasma polymerization from a gaseous hydrocarbon monomer. The system is simple to operate and can be designed for high throughput. The combination of the synthesis and surface treatment of metal nanoparticles in the whole system avoids newly produced metal nanoparticles from being contaminated by surrounding environment.

A home-made self-oscillatory pulsed power supply has been designed and built for the arc evaporation of metal sources. The stability of the pulsed arc system and the cathode erosion rate are discussed. The inductor present in the discharge loop is shown to have a stabilizing effect on the train of pulsed arcs. It was shown that the erosion rate was strongly dependent on peak arc currents due to the increased emission of macroparticles with peak arc currents, and the yield of metal nanoparticles was found to be slightly influenced by the peak arc current.

The produced coated copper nanoparticles were characterized by field emission scanning electron microscopy (FE-SEM), transmission electron microscopy (TEM), Fourier-transform infrared spectroscopy (FT-IR), and X-ray photoelectron spectroscopy (XPS). It was revealed that the coated copper nanoparticles have a metal core of size ranging from a few to 50 nm, and that the thickness of the organic layer ranges from 3 to 10 nm. The smallest copper nanoparticles are crystalline, while the organic coating has a macromolecular structure and shows a hydrophobic behavior. The XPS results showed that the plasma polymer film is chemically adsorbed onto the surface of the copper nanoparticle.

The effects of operating conditions such as reactor pressure and inert gas flow rate on the average size of the produced bare copper nanoparticles were studied. It was

demonstrated that the metal nanoparticle size tends to decrease with decreasing reactor pressure, while inert gas flow rate has little influence on the mean nanoparticle size.

The morphology of the plasma polymer coating was revealed to be strongly dependent on the RF plasma power, reactor pressure, and inert gas flow rate. Two kinds of organic films were produced: a smooth, uniform and dense polymer film and a liquid polymer film. Based on a series of experiments, a "characteristic map" for the in-flight plasma polymerization from the C_2H_6 monomer generating an organic layer onto the Cu nanoparticles was developed. A simplified free-radical mechanism was proposed for the plasma polymerization from ethane.

Other metal sources such as iron and aluminum were used as cathodes in the arc evaporation reactor. Transmission electron microscopy confirmed the production of coated nanoparticles similar in morphology to the ones obtained with the copper cathode. Lastly, ethylene glycol vapor were introduced as an alternative monomer into the plasma polymerization region. A non-uniform coating was observed on the metal nanoparticle surface.

Acknowledgements

I wish to acknowledge my supervisor, Professor Sylvain Coulombe, for his support over the last three years. Professor Coulombe provided me with helpful suggestions and scientific direction. He taught me a great deal about data analysis, the design of reactors and experiments, and the scientific method.

I also want to thank Professor Jean-Luc Meunier and Professor Richard J. Munz for their useful suggestions and fruitful discussions during the Ph.D. proposal defence.

I want to thank my wife, Yanrong Fan, for her support, love and patience during my Ph.D. study, and my parents, Junzhou Qin and Lanzhen Ma, for their love and encouragement.

The students of the plasma research group, Valérie Léveillé, Amna Tariq, Alexandre Ouimet-Storrs, Jason Tavares, David Harbec, Liping Guo, Nadine El-Mallah, Ian Castillo, Ramona Turcu and Lakshminarayana Rao, helped me with my scientific research activities and maintained a cordial and friendly atmosphere in the laboratory.

I would also like to thank Alain Gagnon, Frank Caporuscio, Luciano Cusmich, Walter Greenland, Charles Dolan, Csaba Szalacsi and Roberto Tariello for their technical support; Professor Hojatollah Vali, S. Kelly Sears, Helen Campbell, Suzie Poulin (at École Polytechnique) and Professor Sasha Omanovic for their assistance with the characterization work.

Finally, I acknowledge the financial support provided by the Natural Sciences and Engineering Research Council of Canada (NSERC), the Fonds québécois de la recherche sur la nature et les technologies (FQRNT), and McGill University.

Table of contents

List of figures

List of tables

Chapter 1
Introduction

The application of metal nanoparticles can be traced back 2,000 years ago when they were used to give colors to glasses. The Lycurgus cup (4th century A.D.) in the British Museum is an amazing example of the early use of metal nanoparticles embedded in glasses (Figure 1-1). The glass contains silver and gold nanoparticles, giving the cup a red color under light transmission and a green color under light reflection [1]. In the early applications of glass pigments, the physical basis of the color caused by the presence of different metal nanoparticles was not known until Faraday, who studied aqueous solutions of gold particles, postulated that the red color of the solutions was due to finely divided gold particles. In 1908, Gustav Mie presented a first rigorous theoretical explanation for the optical properties of spherical metal nanoparticles [3]. Thereafter, the optical properties as well as other properties of metal nanoparticles have drawn the ever-increasing attention of researchers and technologists.

Figure 1-1. Photography of the Lycurgus cup: the cup appears green in daylight (light reflection), but red when it is illuminated from inside (light transmission) [2].

Generally, the term nanoparticle is used in the field of materials science to define particulate materials having a linear extent smaller than 100 nm in at least one direction. However, in most applications, the particle size is less than 50 nm [4]. The small size of metal nanoparticles leads to unusual properties (e.g. electrical, optical, electronic, magnetic, thermal, chemical and mechanical properties) with respect to the bulk metals, making them suitable for many new applications, such as catalysts [3], solid additives to propellants [5], optoelectronic nanodevices [6, 7], magnetic ferrofluids [8], nanofluids [9] and polymer nanocomposites [10]. In recognition of their tremendous potential as a platform for developing novel materials and unique applications, several nations around the world are now conducting research and development activities with the aim to gain a better understanding of the unique properties of nanoparticles as well as developing new synthesis and assembling processes [11].

The main objective of this Ph.D. thesis was the synthesis and characterization of organic layer-coated metal nanoparticles. This was achieved through the development of a novel dual-plasma process whereby metal nanoparticles are synthesized via arc evaporation/condensation of the desired metal source and in-flight plasma polymerization from simple hydrocarbon monomers. Copper was chosen as the metal source since copper nanoparticles are of great interest for large-scale applications such as heat transfer enhancement in nanofluids and an extensive amount of work on the erosion behavior of copper cathodes has been accomplished by researchers of the McGill plasma group, and researchers around the world. Other metals such as aluminum and iron have also been tested, but to a lesser extent. Ethane (C_2H_6), a simple saturated hydrocarbon, was used as the gaseous monomer source for the plasma polymerization because this monomer is known to form plasma polymer films over a wide range of plasma processing conditions, and it involves relatively simple gas-phase products whose chemistry is relatively well understood. The produced nanoparticles were characterized with various analytical means such as field emission scanning electron microscopy (FE-SEM), transmission electron microscopy (TEM), Fourier-transform infrared spectroscopy (FT-IR) and X-ray photoelectron spectroscopy (XPS).

The Ph.D. thesis is presented in seven chapters.

Chapter 2 presents a literature review on the various synthesis methods used for producing metal nanoparticles and for modifying their surface. In particular, more attention has been paid to the principles of the cathodic arc evaporation in low pressure gases, the homogeneous nucleation of oversaturated metal vapors and the plasma polymerization processes, which are the basic processes involved in the synthesis of organic layer-coated metal nanoparticles for this Ph.D. project.

Chapter 3 presents the main design considerations and features of the dual-plasma reactor. The details of the experimental setup and auxiliary components, as well as the collection methods used to collect the produced nanoparticles are also presented.

Chapter 4 is devoted to the synthesis of bare copper nanoparticles. In the first part, the experimental procedure and experimental conditions are stated. Next, the stability of the homemade pulsed power supply is studied; the erosion rate of the cathode materials and the net production rate of metal vapors are estimated; and the radius of the expanding metallic plasma and density of metal vapors within the plasma are calculated. Then, the produced metal nanoparticles are characterized. Finally, the effects of operating conditions such as reactor pressure and inert gas flow rate on the properties of the produced metal nanoparticles are investigated.

Chapter 5 is devoted to the synthesis of plasma polymer-coated metal nanoparticles. The effects of experimental conditions such as RF power level, reactor pressure and inert gas flow rate on the products of the plasma polymerization from the ethane monomer are analyzed and a "characteristic map" for the plasma polymerization from ethane is presented. The mechanism of plasma polymerization from ethane is discussed on the basis of the experimental results and information available from the literature.

Complementary experiments aimed at testing the versatility of the dual-plasma process are presented in Chapter 6. The first section of the chapter reports on the synthesis of metal nanoparticles from other metal sources, namely iron and aluminum. The second section reports on the plasma polymerization from ethylene glycol vapors onto the surface of the produced copper nanoparticles.

Chapter 7 presents the concluding statements, original contributions to knowledge and engineering, and recommendations for the further development of the project.

Chapter 2

Literature review

2.1. Introduction

In 1959, Feynman's revolutionary presentation at the American Physical Society's annual meeting motivated the scientific community to explore the realm of nanostructured materials and phenomena (A part of Feynman's presentation is included in a Science article [12]). Since then, considerable efforts have been applied to the synthesis of metal nanoparticles, and many excellent reviews and books have been presented on this subject [4, 13-16]. Various kinds of metal nanoparticles can be prepared by a variety of methods. Depending on the environment in which metal nanoparticles are formed, the synthesis methods can be divided into two main categories: liquid-phase processes and gas-phase processes. That is, the techniques involving the formation of nanoparticles in colloidal systems by means of chemical reduction, thermolysis or photolysis are defined as liquid-phase processes, while the gas-phase processes generally are based on homogeneous nucleation of supersaturated metal vapors and subsequent condensation and coagulation.

Both the liquid-phase process and gas-phase process for metal nanoparticle synthesis are reviewed in this chapter. Especially, the synthesis of metal nanoparticles in the gas phase has received more attention due to its inherent advantages over liquid-phase processes. The involved steps for synthesizing metal nanoparticles, such as the formation of metal vapors, the homogeneous nucleation of the produced metal vapors and the passivation of the generated metal nanoparticles, are reviewed. Finally, important processes related to this Ph.D. project, namely, the cathodic arc evaporation, the homogeneous nucleation and the plasma polymerization are described in detail.

2.2. Metal nanoparticle synthesis

2.2.1. Liquid-phase processes

The various liquid-phase processes for the synthesis of metal nanoparticles share the same characteristics that organometallic compounds or metal salts are employed as precursors and that the formation of metal nanoparticles is the result of their decomposition or reduction. The nanoparticle formation process is influenced by the surrounding environment, temperature, concentration of reagents, diffusive and sorption characteristics of colloid systems and stabilizing substances [4]. Several approaches have been used for the decomposition of organometallic compounds and the reduction of metal salts, namely: chemical reduction [17-19], thermolysis [20, 21], photolysis [22, 23] and radiolysis [24, 25].

Although metal nanoparticles produced by liquid-phase processes have well-controlled shapes, sizes and structures, these approaches are limited by issues related to impurities [13] and the use of expensive or even toxic organometallic reagents. Additionally, the liquid-phase processes are carried out in discrete batches with batch time ranging from hours to days. They are also characterized by numerous aftertreatment steps such as the separation of the produced nanoparticles from the liquid phase and the drying of the products. Gas-phase approaches appear more promising than liquid-phase approaches because of several inherent advantages: the high purity of the produced nanoparticles, the operation in continuous or quasi-continuous mode, the ease of controlling the process parameters, and the use of simple collection methods.

2.2.2. Gas-phase processes

In gas-phase synthesis, the establishment of supersaturation conditions for metal vapors is required. That is, the generated metal vapors must be cooled down efficiently either by mixing the vapors with a cold inert gas stream, by heat exchange to the surroundings, or by high-speed expansion. Supersaturation of metal vapors can also be achieved by the chemical reaction of gas-phase organometallic molecules to form a condensed phase. When the degree of supersaturation reaches a high value, homogeneous nucleation occurs and metal nanoparticles form.

Most gas-phase synthesis processes can be classified as either physical or chemical in nature. For physical methods, precursors are vaporized into a background gas, and then the generated metal vapors are cooled down to form metal nanoparticles. For chemical gas-phase methods, precursors are delivered into the reactor as vapors (by a sublimation or bubbler system if necessary) or very small droplets of precursor solutions by using a nebulizer. The decomposition/chemical reaction of these precursors is induced in the gaseous phase to generate metal vapors. The features of the physical and chemical methods are discussed next.

2.2.2.1. Physical methods for gas-phase synthesis

With physical methods of producing metal nanoparticles in the gaseous phase, considerable amounts of metal atoms are generated from metal sources by intensive energy inputs and then, these atoms are cooled down, forming nanoparticles of the desired size, shape and composition. For example, numerous bulk solid metals can be eroded or evaporated by heating to generate metal atoms. Variants of the physical methods differ in the evaporation method used.

Perhaps the most straightforward method of producing metal vapors from a bulk metal is the direct evaporation of the metal when placed in a heated crucible. Wegner et al. [26] presented a detailed experimental investigation of this method when used for the preparation of bismuth nanoparticles. Bismuth vapors were produced in an externally heated crucible containing the melt. In their approach, the transport of the metal vapors by an argon carrier gas jet is followed by the rapid quenching of the metal vapors with a second argon stream in a diluter. Bi nanoparticles with an average size ranging from 12 to 37 nm were produced by controlling the process parameters such as quenching gas flow rate and reactor pressure. Along the same line of thought, Mahoney and Andres [27] developed the aerosol synthesis of metal nanoparticles (Figure 2-1). The evaporation of the desired metals is achieved by heating a tungsten basket containing the metal to be vaporized using DC arcs, and the metal vapors are carried away by an upward argon flow and quenched with a second argon stream. Mean metal nanoparticle diameters in the 1-100 nm range have been achieved. Furthermore, they reported that nanostructured metallic oxides and nitrides can been formed by addition of reactive gases into the high temperature evaporation region or into the cooler quench region.

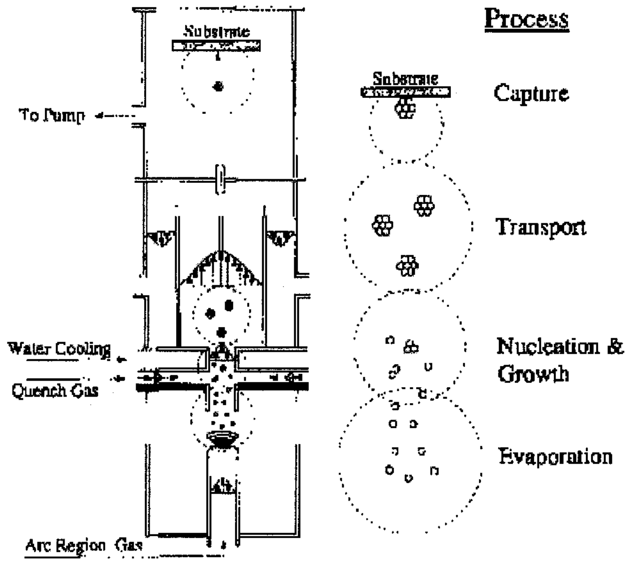

Figure 2-1. Schematic diagram of the direct evaporation process developed by Mahoney and Andres [27].

A laser ablation process has also been developed to vaporize high-melting-point materials. Ayers et al. [28] used a laser-ablation cluster source, which uses a 100 Hz KrF (248 nm) excimer laser for the high-repetition-rate laser vaporization of metal targets, combined with a fast flowtube reactor for the production of ligand-coated titanium metal clusters. An argon stream was used for cooling down the laser-generated vapors. Laser ablation in the presence of a reactive gas such as oxygen or nitrogen is also highly suitable for synthesizing ultrafine metallic oxides or nitrides with high-melting points. Titania nanoparticles were synthesized by Harano et al. [29] using the pulsed laser ablation of titanium rods in an O_2/He atmosphere. Marine et al. [30] described the basic principles of this method and presented theoretical developments for the condensation of nanoparticles. However, the laser ablation method implies the use of expensive and bulky high-energy lasers and special focusing optics making this synthesis process fairly expensive.

Ion sputtering is another method of vaporizing materials via bombardment with high-velocity ions of an inert gas. Hahn and Averback [31] prepared a wide range of nanocrystalline particulates made of materials such as Al, Mo, $Al_{52}Ti_{48}$ and ZrO_2, with diameters in the 7-50 nm range by a DC/RF magnetron sputter source. Urban et al. [32] recently demonstrated the feasibility of synthesizing metal nanoparticles from the magnetron sputtering of metal targets. However, this process is normally carried out in high-vacuum systems ($< 10^{-3}$ Torr), which constraint hinders the aftertreatment of the nanoparticles in the aerosol form (e.g. the *in-situ* deposition of an organic layer).

Another gas-phase physical method used for the generation of metal vapors is the direct arc evaporation of the bulk metal. A high-current arc maintained between two electrodes, with one being made of the desired metal, is used to produce metal vapors. Ermoline et al. [5] proposed that a high-energy density electron flux, formed in a pulsed microarc discharge (Figure 2-2 (A)), vaporizes a thin layer of the consumable aluminum anode, thus producing aluminum nanoparticles of well-controlled sizes. Schwyn et al. [33] developed an aerosol generator producing metal nanoparticles by electrode atomization using a spark discharge (Figure 2-2 (B)). This method has the advantage of being quite universal with respect to the choice of the metal material, and extremely simple. Weber et al. [34] used the same technique to prepare nickel nanoparticles for studying the downstream heterogeneous catalytic reactions on these gasborne nanoparticles. Rao et al. [35] have used an atmospheric pressure magnetically-driven DC arc to thermally erode a copper cathode and produce copper nanoparticles.

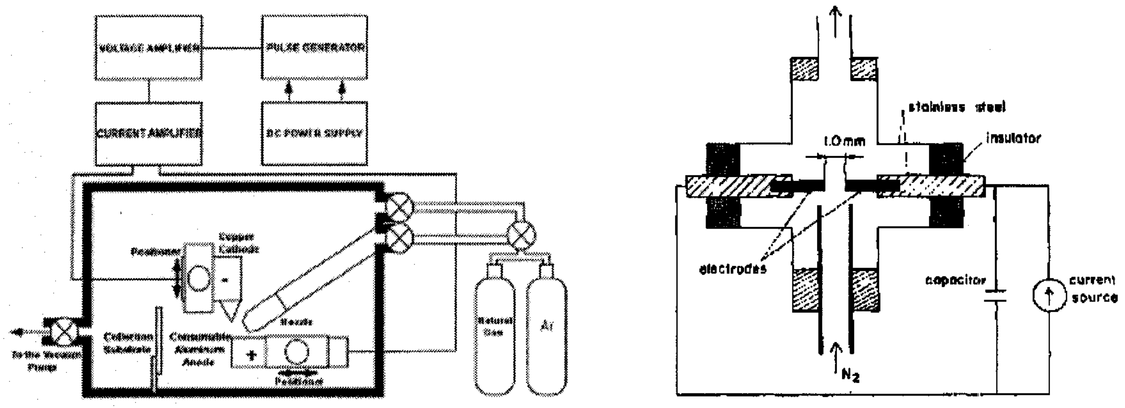

(A)

(B)

Figure 2-2. Schematic diagrams of the arc evaporation processes developed by Ermoline et al. (A) [5] and Schwyn et al. (B) [33].

2.2.2.2. Chemical methods for gas-phase synthesis

The gas-phase chemical reaction of precursors such as organometallic compounds can be used as an alternate method to synthesize metal nanoparticles. The thermally-induced or chemical reaction-induced decomposition of the organometallic compounds leads to the formation of metal vapors with extremely high supersaturation ratios, thus producing metal nanoparticles. Various strategies have been used to induce the decomposition of organometallic compounds and to form the desired metal nanoparticles. Some examples of the application of this approach to the synthesis of metal nanoparticles are presented next.

Magnusson and Deppert [36] produced single-crystal tungsten nanoparticles in the 15-60 nm size range by thermal decomposition of tungsten hexacarbonyl in a cracking furnace at temperatures up to 1000 °C, and by sintering the small primary particles in a second furnace operating at a temperature of 1900 °C. Using the same method, Nasibulin et al. [37] produced crystalline copper nanoparticles with the precursor of copper acetylacetonate at a furnace temperature around 500 °C. Copper nanoparticles were also produced by Kim et al. [38] by the chemical reduction of a copper salt precursor, namely, copper nitrate [$Cu(NO_3)_2 \cdot 2.5\ H_2O$].

Some organometallic precursors can be heated by absorption of laser energy to induce chemical reactions leading to the formation of metal vapors. This method enables a localized heating since only the precursor molecules are selectively heated while the carrier gas is only indirectly heated by the collisions with the reactant molecules. For example, the decomposition of $Fe(CO)_5$ molecules induced by a transversely excited atmospheric pressure CO_2 laser led to the formation of Fe nanoparticles [39]. A plasma can be used as another means for delivering the energy required to initiate chemical reactions. Bapat et al. [40] produced crystalline silicon nanoparticles with the decomposition of silane in a low-pressure, inductively-coupled plasma.

2.2.3. Stabilization of metal nanoparticles

Due to their enormous specific surface area (e.g. ~100 $m^2\ g^{-1}$ for 10 nm-diameter Cu particles), nanoparticles possess a large surface energy and thus, are thermodynamically unstable, favoring spontaneous processes. For example, metal nanoparticles agglomerate together as a result of their high surface free energy. Because of their high chemical reactivity, they are readily oxidized or become contaminated upon exposure to surrounding environments such as air and moisture, which processes alter their properties. In addition, without proper surface treatments, the bare metal nanoparticles may be incompatible with host materials, which limits their range of applicability as dispersed phases in nanocomposites. Therefore, a major challenge associated with the synthesis of metal nanoparticles is their stabilization (or passivation). Since the synthesis methods involve either liquid-phase or gas-phase processes, their stabilization can also be achieved by two different kinds of strategies: the adsorption in the liquid phase of stabilizers such as polymeric ligands [19, 23, 24] or surfactants [17, 20, 21] on the metal nanoparticle surface, and the formation of protective coatings such as organic [28], graphite [5], silica [41], or ceramic layers [42] around metal nanoparticles in the gas phase.

Klug et al. [41] synthesized silica-coated nickel nanoparticles by combining the nickel nanoparticle synthesis via arc evaporation with the coating formation by the decomposition of tetraethyloxysilane (TEOS) in a chemical vapor deposition furnace (Figure 2-3).

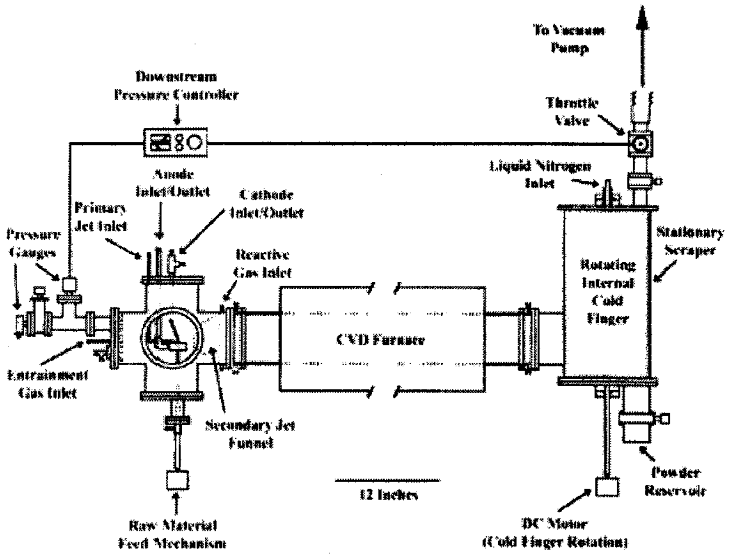

Figure 2-3. Schematic of the coated nanoparticle synthesis reactor developed by Klug et al. [41]

Ayers et al. [28] investigated the formation of ligand-coated titanium nanoparticles by generation of titanium clusters via laser ablation of titanium rods followed by the coating formation from ethylenediamine in a flowtube reactor. Vollath and Szabó [42] produced finely dispersed Al_2O_3-coated ZrO_2 nanoparticles and plasma polymer-coated Fe_2O_3 nanoparticles in a continuous flow dual microwave plasma process. Though versatile and applicable to the direct synthesis of metal nanoparticles coated with protective layers, these processes involve the use of harmful metal precursors such as ferrocene organometallics and TEOS.

A combined arc evaporation/condensation and plasma polymerization process for the synthesis of plasma polymer-coated metal nanoparticles has been developed in this Ph.D. project. This dual-plasma process might offer several important features such as the one-step synthesis of coated metal nanoparticles, the convenience of the operation, the ease of controlling the process parameters, and the versatility to use numerous metal sources and organic monomers. The following literature review outlines the basic principles of the cathodic arc evaporation, homogeneous nucleation and plasma polymerization from saturated hydrocarbons, which processes are used in this Ph.D. project.

2.3. Individual steps associated with the synthesis of plasma polymer-coated metal nanoparticles

2.3.1. Cathodic arc evaporation

Electric arcs are self-sustaining discharges maintained between two electrodes in presence of gases and/or vapors produced from the erosion of the cathode. Such discharges are characterized by relatively high current levels (>1 A) and minimum sustaining voltages which are not much larger than the first ionization potential of the plasma gas. The cathode of the electric arc is responsible for the emission of electrons which in turn, are responsible for the production of ions and the maintenance of the conductive path in the otherwise neutral inter-electrode gap. The positive ions also play the important role of main heating agent for the cathode surface, and are thus indirectly responsible for the (thermionic) electron emission process from which they originate. At very high ion density, these ions also contribute to the maintenance of a high electric field at the cathode surface, thus causing an enhanced electron emission by the thermo-field effect. Hot cathodes, which are made of a refractory material (e.g. W), feature electron emission mostly by thermionic emission and over a large surface area of the cathode. The arc attachment is said to be "diffuse" in such a case. Accompanying the electron emission process is the material evaporation, which can be used for nanoparticles synthesis if the generated metal vapor cloud is rapidly supersaturated. With non-refractory cathode materials (e.g. Cu, Fe and Ni) or in the absence of a plasma gas in the case of refractory cathodes, the arc attachment point on the cathode must constrict to a small surface area in order to maintain conditions leading to strong electron emission. Such a constricted attachment region is called the cathode spot.

Cathode spots provide not only the emitted electrons for the current continuity, but the medium for the arc discharge under low pressure conditions. They are in the range of 10-100 μm in diameter on the cathode surface [43]. The concentrated current flow in cathode spots causes very high local temperatures, strong local electric fields and correspondingly high local metal vapor densities which in turn, can be used as precursor materials for the efficient production of metal nanoparticles. Several researchers have studied the features of the cathode spots in great detail [43-45], though a complete understanding is still lacking. It is however well-known that the self-sustaining operation of arc discharges at low pressures unavoidably involves cathode spots [46, 47]. Thus, such systems are convenient sources of metal vapors.

2.3.1.1. Structure of the cathode spot

A representative schematic of the cathode spot structure in a vacuum arc plasma is shown in Figure 2-4 (the third chapter in [45]) and [43]. The cathode spot vicinity is divided into several zones: cathode surface, cathode sheath, heavy particle relaxation zone, electron beam relaxation zone and plasma expansion zone. The cathode surface is heated and evaporated in a localized circular area with a 10-100 μm radius. At the cathode surface, the emission of electrons, evaporation of neutral atoms and impact of back-flowing ions are key processes in the heat, mass and current transfers. Next to the cathode surface there exists a thin zone, the cathode sheath, with an extent of 1-10 nm. Created mainly by the space charge of ions, a strong electric field is present in the cathode sheath, accelerating the electrons away from and the back-flowing ions towards the cathode surface. Electrons and ions pass through the cathode sheath without collisions.

Emitted atoms from the cathode surface collide amongst themselves and with the back-flowing heavy particles (e.g. ions and atoms) in the relaxation zone of heavy particles, which extends a distance of a few times the heavy particle mean free path from the cathode surface. Similarly, emitted electrons suffer numerous collisions with neutral atoms, ions and other "newly" produced electrons in the relaxation zone of the electron beam, which extends from the cathode surface and is defined by the requirement for the energy of emitted electrons from the cathode surface to equilibrate with the energy of the electrons created by electron-impact ionization within this zone. This distance is typically a few hundred times larger than the mean free path for the ionization of the atom. Because of the high pressure in this zone, the recombination of electrons and ions also happens. Behind the electron beam relaxation zone exists the plasma expansion zone, where the metallic plasma cloud expands into vacuum until contacting the anode or another solid surface.

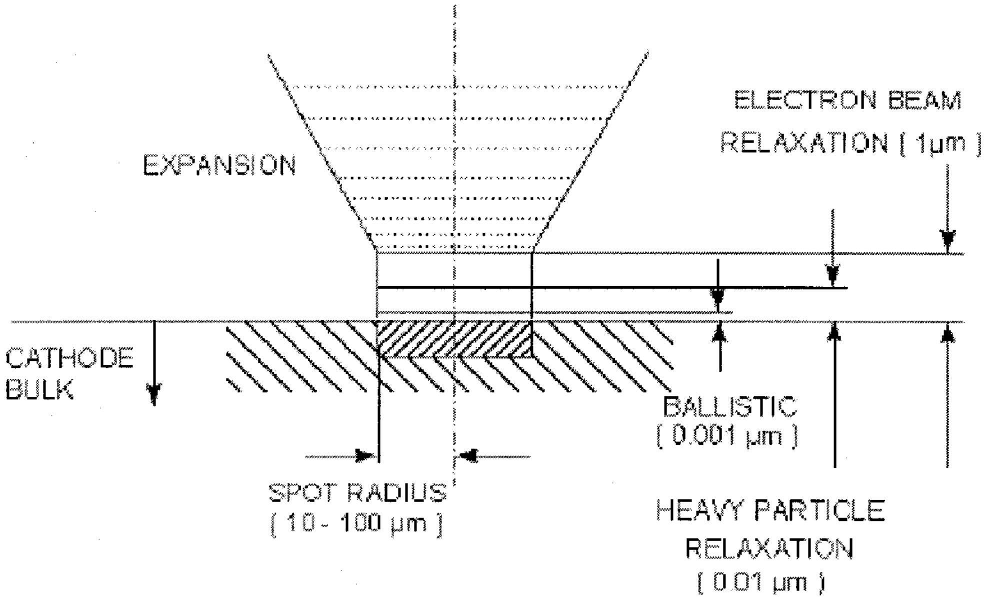

Figure 2-4. Schematic diagram of vacuum arc cathode spot structure [43, 45].

2.3.1.2. Expansion of cathodic arc plasma in low pressure background gases

The cathodic arc plasma in low pressure gases has been investigated by many researchers such as Kimblin [48], Emtage [49], and Drouet and Meunier [50-53]. Experimental evidences suggested that the cathode spots of low current arcs over a wide pressure range up to atmospheric pressure are indeed similar to the vacuum arc cathode spots [48], except that the expansion of the cathodic arc plasma is confined by the background gas.

The cathodic arc plasma produced by the erosion of the cathode surface expands with velocities reaching approximately 10^4 m s^{-1} in vacuum [48, 50, 54]. While in low pressure background gases, the expansion of the metallic plasma is hindered by the background gas once a minimum threshold pressure is reached. The value of this minimum pressure depends on the chemical composition of the background gas, gases with larger atomic mass having lower required minimum pressures [52].

Meunier and Drouet [50-53] investigated the effect of background gases on the expansion of metallic plasmas and found that the metallic plasma and the ambient gas are separated into two distinct regions when the pressure is above a given threshold, and that a shock wave acts as a boundary between them. The plasma/gas boundary expands with an initial vacuum expansion velocity (e.g. 10^4 m s^{-1}), then rapidly decays to zero when the expansion velocity of the metallic plasma equals the sound velocity of the ambient gas. It is claimed that there is no matter exchange between the metallic plasma and the ambient gas during the expansion of the plasma/gas boundary. When the boundary reaches a steady-state position, the diffusion rate of metal vapors out of the plasma volume equals their generation rate from the erosion of the metal surface. This situation is kept unchanged until the end of the cathodic arc plasma.

The pressure of the background gas has a strong effect on the expansion velocity of the plasma/gas boundary and the final volume of the confined metallic plasma. The higher the background gas pressure, the faster the decrease of the metallic plasma expansion velocity, and the smaller the volume of the confined metallic plasma. Typically, it takes several to tens of μs for the plasma/gas boundary to reach a steady-state position [50-53].

A snow-plow expansion model was developed to describe the expansion of the metallic plasma confined in low pressure gases and to predict the radius of the metallic plasma steady-state volume [50-52]. According to Meunier [53], the final radius R_c can be expressed by

$$R_c^{\beta} f = E_r \tag{2-1}$$

with $f = \dfrac{2\pi\rho_g}{3\tau_c I}\left(\dfrac{C^2 + \dfrac{2kT}{M_g}}{V_0^2 - \dfrac{C^2}{3}}\right)$

where E_r is the vacuum erosion rate of the cathode materials, f is a characteristic function of both the background gas and arc current used, and the exponent β varies between 2.1 and 2.5. kT, M_g and ρ_g are the temperature (times the Boltzmann constant), atomic mass and mass density of the background gas, respectively. I is the arc current, V_0 is the vacuum expansion velocity of the metallic plasma, and τ_c is the plasma expansion time for the boundary reaching the sound velocity C of the background gas.

2.3.1.3. Material loss from the cathode surface

As a consequence of the high local cathode surface temperature associated with the concentration of the applied power (up to 10^{10} W m^{-2}) [55], the cathode surface under the cathode spot is severely eroded, creating a conducting medium necessary for sustaining the arc discharge. The erosion products consist of ions, atoms and liquid droplets which, upon ejection from the cathode surface, lead to the formation of macroparticles (>100 nm in diameter). The erosion rate is conveniently defined as the mass loss per transported charge. The reported erosion rate of vacuum arcs on copper cathodes ranges from 40 to 140 μg C^{-1} [56]. The erosion rate and the distribution amongst its constituents (vaporization and liquid droplet ejection) depend on the arc current, discharge duration, cathode material and its purity, cathode temperature and gas pressure. High arc currents, high temperatures under the cathode spot and low working gas pressures all favor the evaporation of metal atoms [45].

The ion flux distribution is peaked in the forward direction of cathodic arc plasma [57, 58]. For non-refractory metals, such as Pb, Zn and Cd, most of the ions are singly charged, whereas for refractory metals, such as Ta and Mo, the charge number of the multiply charged ions may be as high as 5 or 6 [58]. It has been determined that the ion current is in the range of 7-10% of the arc current for a wide range of metals such as Cd, Zn, Cu, C, Mo and W [59]. This ion current fraction is independent of the electrode spacing, electrode sizes, and the dimensions of the vacuum chamber in which the arc burns [58]. And, it is also kept content for a wide range of currents (up to kA) and arcing times (milliseconds to seconds).

There exist arguments on the origin of the metal vapors emitted from the cathode spot. A common view is that the total mass flux emitted from the cathode spot consists mainly of metal vapors, which is partly ionized to sustain the arc plasma. However, Jenkins [60] and Tuma [57] stated that the most likely source of the metal vapor is the evaporation of emitted macroparticles during their flight.

The ejection of macroparticles from beneath the cathode spots represents a major source of cathode material loss. The size of the macroparticles varies from 100 nm up to about 100 μm [45, 61]. These macroparticles originate from the plasma-solid interaction under the cathode spots. Jüttner [62] explained that the formation of macroparticles is caused by the local plasma pressure acting on the melted cathode materials (Figure 2-5).

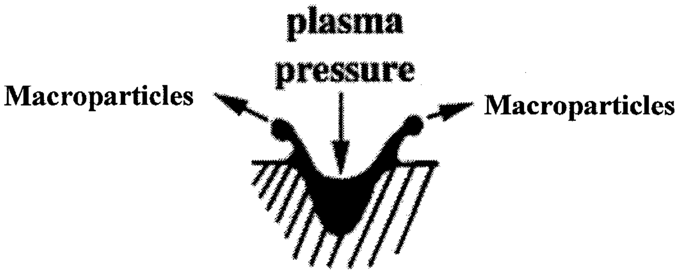

Figure 2-5. Macroparticle formation from the cathode spots: the melted cathode material is pushed by plasma pressure [62].

The very high local temperature causes the formation of a molten pool at the cathode surface, and the rapid removal of the liquid metal by the high plasma pressure leads to macroparticle ejection. The production of macroparticles is therefore inherently linked to the activity of the cathode spot. McClure [63] developed a similar mechanism of macroparticle ejection by the action of local plasma pressure. Other processes such as expulsion of cathode materials by the local electric field and explosive evaporation of the cathode surface as a result of intense Joule heating may play partial roles in the ejection of macroparticles [55].

Macroparticles are by-products rather than active constituents of the cathode spots, because they are not necessary for the self-sustaining operation of the arc discharge and they do not influence the electric characteristic of the cathode spot [45]. However, when cathodic arc evaporation is used to produce metal nanoparticles, the presence of macroparticles mixed with metal vapors deteriorates the yield of produced metal nanoparticles. Therefore, it is usually desirable to reduce or even eliminate them.

2.3.1.4. Reduction of macroparticle ejection

The ejection of macroparticles can be reduced or even eliminated by the following methods: *(I)* decreasing the bulk cathode temperature [48]; *(II)* decreasing the arc current amplitude; *(III)* increasing the velocity of the cathode spots (e.g. through the use of magnetically steered arcs) [45]; *(IV)* working with pulsed arc discharges [64-66]. These methods are now briefly discussed. The decrease of the bulk cathode temperature can be achieved by the efficient cooling of the cathode. The arc current amplitude can be conveniently decreased, but this leads to a lower productivity for the arc evaporation process and in turn, to a lower production of metal vapors. Magnetically-driven cathode arc spots can generate fewer macroparticles by shortening the interaction time of the arc plasma with the cathode surface. However, the complication involved with the design of magnetic confinement techniques in such arc discharges hinders the popular adoption of this method [45].

The use of arc current pulses can strongly reduce the ejection of macroparticles while a high productivity of metal vapors is maintained. Büschel et al. [65] developed a pulsed arc process in which a small DC current of less than 50 A is superposed by current pulses of different shapes for depositing TiN and TiAlN layers onto metal substrates. The results showed high metal vapor production rates and a significant reduction of the number and size of the macroparticles ejected from the cathode spots. They also suggested that further reduction of the macroparticle ejection yield can be achieved by increasing the magnitude of the current pulse and decreasing the pulse time. A similar modified pulsed arc process was used by Engers et al. [66] to deposit metal nitride coatings on substrates. Recognizing the advantages of pulsed arc sources, this kind of electrical energy source is used in the present study.

2.3.2. Homogeneous nucleation

2.3.2.1. General description of the homogeneous nucleation process

The general scenario of metal nanoparticle formation within an oversaturated metal vapor can be described as follows [67-71]. Initially, a large number of metal atoms are generated from physical or chemical methods (described in Section 2.2.2.) and, at this stage, the temperature of the vapor cloud is high, preventing the nucleation of the metal vapors. As the temperature of the metal vapor cloud decreases due to the efficient transport and quenching by the inert gas, the saturation ratio of the metal vapors is correspondingly increased. - The saturation ratio is defined as the ratio of actual monomer concentration to the equilibrium monomer concentration based on the saturation vapor pressure at the same temperature. - Upon sufficient cooling, this ratio reaches such a high value (~1000) that homogeneous nucleation of the metal vapor takes place, thus forming nuclei of metal nanoparticles. The remaining metal atoms condense heterogeneously on the freshly nucleated particles, and the particles grow by coagulation. Figure 2-6 [68] shows the calculated value of the saturation ratio as the metal vapor is cooled for the base case: an iron vapor partial pressure of $5x10^{-4}$ atm (~50 Pa) is cooled down with a cooling rate of 30 000 K s^{-1} in a closed chamber. The thick line, labeled "nucleation suppressed", indicates that the saturation ratio would increase if metal particles larger than the equilibrium monomers are not allowed to form. The calculated saturation ratio follows this line until it reaches the peak value of about 280, then it drops rapidly. It levels off to unity at approximately 1400 K.

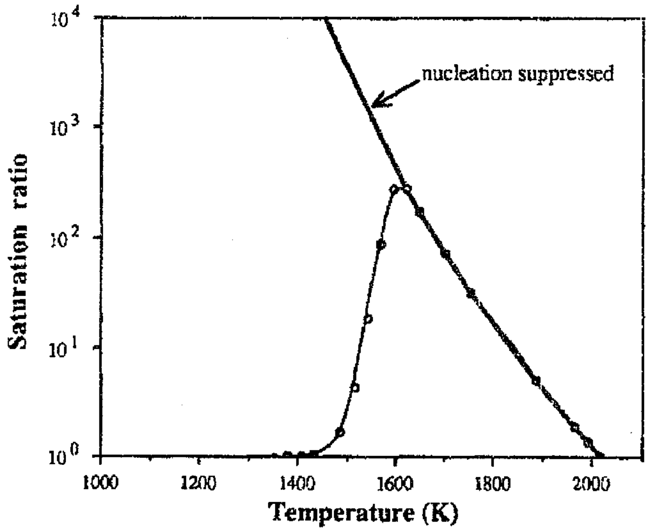

Figure 2-6. Calculated saturation ratio for the base case: an iron vapor partial pressure of $5x10^{-4}$ atm (~50 Pa) and a cooling rate of 30 000 K s^{-1}, which was developed by Girshick and Chiu [68].

To understand the effect of the saturation ratio, it is instructive to consider the critical size for a stable nucleus. At the critical size, the condensation rate of a nucleus equals its evaporation rate. The critical size for a stable nucleus, d^*, can be written as equation (2-2) [68]:

$$d^* = \frac{4\sigma\upsilon_1}{kT\ln S} \tag{2-2}$$

where σ is the surface tension of the nucleus (N m^{-1}), k the Boltzmann's constant, T the temperature, υ_l the monomer volume of metal vapors and S, the vapor saturation ratio. Particles smaller than the critical size tend to evaporate and larger ones continue to grow. During the beginning of the metal vapor cloud cooling process, the critical size is very large, so no stable particles can form. With the rapid increase of the saturation ratio, the critical size eventually drops to such a small value that a considerable amount of metal clusters whose size is equal or larger than $d*$ can condense to form metal nanoparticles.

The size control of metal nanoparticles condensed from the metal vapors has been studied by many researchers [5, 26, 27, 33, 68, 70]. In summary, the size of metal clusters obtained by the homogeneous nucleation process is governed by the cooling rate and the metal monomer concentration. Higher cooling rates and lower monomer concentrations lead to smaller metal clusters. The final size of the metal nanoparticles depends on the coagulation of condensed metal clusters, which process is itself affected by the density of metal clusters and the average residence time of the clusters in the quench region. Smaller densities of metal clusters and shorter average residence times in the quench region lead to lesser extents of coagulation. A high cooling rate combined with a rapid dilution of the produced aerosol and short average residence times lead to the production of smaller metal nanoparticles.

This general description of the homogeneous nucleation process is helpful for us to understand the fundamental features of the formation of metal clusters and particles within supersaturated metal vapors. However, this description can not be applied to the vapor/plasma plume generated by the cathodic arc evaporation in low pressure background gases because of both the rapid expansion of the cathodic arc plasma and the shock wave front created by the confinement of the metallic plasma expansion by the ambient gas. Special features of the nucleation of vapors and cluster formation in the confined cathodic arc plasma by low pressure gases are described next.

2.3.2.2 Nucleation of vapors and cluster formation within the expanding metallic plasma in low pressure gases

Meunier [53] studied the fullerene synthesis by the cathodic arc evaporation of graphite electrodes. With the snow-plow model of the cathodic arc plasma expansion, the author predicted that the stationary plasma/gas boundary volume and the volume just after this boundary are most likely the nucleation zones of larger carbon molecules. This postulate was confirmed by experimental measurements of the spatial distribution of the C_2 Swan band molecule emission for a 120 A cathodic carbon arc in 55 torr helium gas. Under these conditions, the extension of the nucleation zone was approximately 1 mm.

The expanding behavior of the metallic plasma and the effect of the background gas on the plasma expansion are very similar for the processes of cathodic arc evaporation of bulk solids and the laser ablation of bulk solids [50, 53]. Both processes involve the fast expansion of the plasma/vapor plume generated on a localized surface area of the target materials under the action of high-energy particles or laser pulses, and the formation of a shock wave front created by the confinement of the plasma/vapor plume in background gases. For the pulsed laser ablation process, the formation of clusters and nanoparticles within laser-generated plasma/vapor plumes has been extensively studied [30, 72-76].

Luk'yanchuk et al. [75] studied the strong non-equilibrium conditions within laser-generated silicon plasma/vapor plumes. They showed that the cooling rate and density of vapor-phase species are strongly non-uniform within the plume. As a consequence, the rate of nucleation and growth of clusters vary strongly within the plume. Marine et al. [30] described the basic principles of nanoparticle synthesis by conventional pulsed laser ablation. They stated that three different waves, that is, the saturation wave, the supercooling wave and the quenching wave, propagate through the expanding plasma/vapor plume from the periphery to the center (Figure 2-7). After the condensation and growth stages, the formed clusters follow a long stabilization period, where the stabilization of high-temperature nanoparticles is achieved through radiative, evaporative and collisional coolings. The typical time scales are 0.05-20 μs and 0.2-6 ms for the condensation-growth and stabilization stages, respectively.

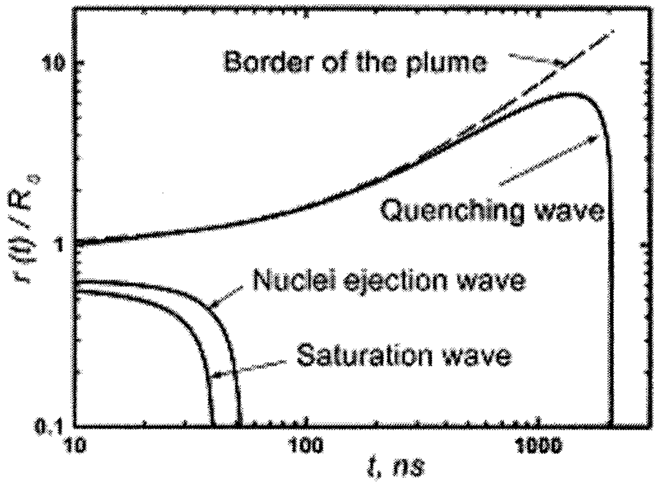

Figure 2-7. Propagation of saturation, nuclei ejection and quenching waves through the Si vapor plume [30]. Initial parameters of the vapor plume: velocity 6×10^5 cm s^{-1}, radium 0.1 cm, specific volume 300 cm^3 g^{-1}, temperature 7000 K, pressure 68.4 atm.

Geohegan et al. [77] reported that the chemical composition of the background gas strongly influences the dynamics of nanoparticle synthesis and transport in the process of pulsed laser ablation of *c*-Si into low pressure gases. Heavier Ar atoms can effectively stop and even reflect the Si atoms, resulting in the formation of a uniform and stationary nanoparticle cloud in the plasma/vapor plume, while lighter He atoms only gradually decelerate the expansion of the Si plume with a series of small-angle collisions, leading to a turbulent ring of clusters which propagates outward at 10 m s^{-1}. With the pulsed laser ablation of silicon into a flowing argon gas at 1 torr, the Si vapor/plasma plume was slowed down from initially 2×10^4 to 100 m s^{-1} within 20 μs while the onset time for silicon nanoparticle formation was 3 ms.

Pászti et al. [74] examined the pressure effects on the metal particle formation by laser ablation of Cu and Ag metals in argon gas. Individual Cu nanoparticles with diameters of 3-4 nm were generated in Ar in the 100-1000 Pa pressure range, while Ag nanoparticles of 4-6 nm were produced at 500 Pa in Ar as opposed to 8-15 nm at 1000 Pa. The observed results were explained by the different deceleration rates of the evaporated Cu and Ag atoms into the argon gas. The energy transfers between the outward Ag atoms and/or clusters and the Ar atoms are less efficient than in the case of Cu atoms because of the larger atomic mass difference between Ag and Ar atoms.

The nucleation of evaporated vapors and the cluster formation occur as a result of the quenching of the metal vapors/ions which diffuse from the confined metallic plasma to the low pressure inert gas. The nucleation time as well as the size and composition of the clusters depend on the cathodic arc plasma parameters and on the type and pressure of the ambient background gas [73]. With a higher pressure, the vapor/plasma plume is confined within a smaller region, resulting in the production of larger particles. At constant pressure, the average cluster size increases with the atomic mass of the background gas [73].

2.3.3. Plasma polymerization

Plasma polymerization refers to the formation of high-molecular-weight products under the effect of plasma [78]. It can be used for the preparation of ultrathin coatings on substrate surfaces such as metals, glasses, polymer films and papers. In fact, almost all solid surfaces can be coated with ultrathin films by plasma polymerization. One of the main advantages of the plasma polymerization process is that it can be used to deposit organic films with thicknesses ranging from several nanometers to several hundreds of nanometers [79]. In contrast to conventional polymerization, the monomer material used in plasma polymerization does not need to contain functional groups (e.g. a double bond). Furthermore, the deposited films, called plasma polymers, are significantly different from conventional polymers. In most cases, plasma polymers are highly branched, highly cross-linked and insoluble. These unique and advantageous features of the plasma polymerization process made many researchers choose it as the method for forming nanoscaled organic layers on desired surfaces.

Shi et al. [80] demonstrated the feasibility to deposit a uniform ultrathin (~2 nm) plasma polymer film onto Al_2O_3 nanoparticles by inductively-coupled radio-frequency (RF) plasma polymerization from pyrrole monomers. Kouprine et al. [81] developed a capacitively-coupled RF plasma (CCRF) process to deposit an amorphous, high-density thin (5-30 nm) hydrocarbon film onto SiO_2 nanoparticles. Both methane (CH_4) and ethane (C_2H_6) were used as the monomer. Kouprine et al. also used this system to produce ferromagnetic nanopowders encapsulated into a carbon/graphite matrix [82].

Vora and Moravec [83] obtained diamond-like carbon (DLC) coatings on polished KBr substrates via CCRF plasma deposition using hydrocarbon gases (C_4H_{10}, C_2H_6, C_3H_8 and CH_4). The DLC films were extremely hard, electrically insulating, chemically inert and optically transparent. Vanhulsel et al. [84] produced the same kind of DLC coatings from a magnetically confined inductively-coupled RF plasma using CH_4 monomers. Furthermore, they proposed that the characteristics of the deposited coatings can be changed from soft polymer-like films to hard DLC films by increasing the ratio of the RF power to the system pressure.

Fernandes et al. [85] treated aluminum alloys by depositing plasma polymer coatings from hexamethyldisiloxane (HMDSO) monomers in a CCRF plasma reactor. The coating provided good corrosion resistance and durable adhesion properties. A protective coating for infrared laser windows prepared by CCRF plasma polymerization from C_2H_6 monomers was reported by Akovali [86]. The plasma polymerization from some simple hydrocarbons such as C_2H_4, C_2H_6, CH_4 and C_3H_6 have also been studied by several researchers [87-93].

The wide-range applications of the plasma polymerization process are based on the unique properties of non-equilibrium plasmas, which can cause the physical and chemical reactions of monomers at relatively low temperatures.

2.3.3.1. Non-equilibrium properties of low-pressure plasmas

In most cases, plasma polymerization is carried out under low pressures, typically in the 10^{-2}-10 torr range [78]. For plasmas sustained in this pressure range, the degree of ionization ranges from 10^{-6} to 10^{-3} [94]. The physical and chemical processes in the low-pressure plasmas, especially those sustained in a mixture of molecular gases, are described as the following steps. First, electrons and ions, produced by the partial ionization of the gas molecules, gain energy from the external electric field. The electrons, being the lightest and most mobile species present in the plasma medium, are promptly accelerated by the external electric field, thus acquiring most energy from it. Unlike the electrons, the ions do not quickly acquire energy from the electric field because of their large mass, so they remain essentially "cold". The energetic electrons transfer the obtained energy to the molecules of gases and other heavy species by elastic and inelastic collisions. As a result of these collisions, excitation, dissociation and ionization of the heavy species take place, thus forming other plasma species such as free radicals, excited metastables and ions [95].

Due to the low degree of ionization (10^{-6}-10^{-3}) of low-pressure plasmas, the electron density is several (3 to 7) orders of magnitude lower than the density of molecules and other heavy species. Because of the low density and the low heat capacity of the electrons, the energy transferred through collisions with the heavy species (e.g., molecules, radicals and ions) is quite small. In fact, the electrons retain most of the energy they gain from the external electric fields. As a result, the temperature of the electrons (T_e) is much higher than that of the heavy species and $T_e >> T_i > T_g$, where T_i is the ion temperature and T_g, the gas temperature. T_e can reach values as high as 10^4-

10^5 K, while T_g can be as low as room temperature. In addition, short-living plasma species like free radicals, atoms and excited metastables exist in the plasma. When newly created by dissociative collisional processes, these short-living species receive a large mount of energy and their temperature may reach 10^4-10^5 K, but also quickly relax through other collisions [95].

Hence, low-pressure plasmas sustained in mixtures of molecular gases contain a significant density of molecules, atoms, radicals, electrons and ions. All these species are at various temperatures and in various energetic states. The local thermodynamic equilibrium is not reached between the electrons and the heavy particles, thus providing conditions favorable to the treatment of heat-sensitive materials.

2.3.3.2. Plasma chemistry in low-pressure plasmas

Due to the non-equilibrium nature of low-pressure plasmas, they are widely used for generating excited and ionized particles such as free radicals and ions, as well as chemically active atoms at low temperatures. These chemically reactive species can react with themselves or with the active points on the surface exposed to the plasma.

Because of the diversity and complexity of the elementary chemical reactions taking place in low-pressure plasmas, a complete understanding of the plasma chemistry is still far from being achieved. A few monographs [78, 94-98] discuss the fundamentals of plasma chemistry in low-pressure plasmas. The chemical reactions taking place near and at surfaces exposed to low-pressure plasmas can be classified in two categories: homogeneous and heterogeneous reactions. The homogeneous reactions involve the collisions among electrons, monomer molecules and other heavy plasma species present in the gas phase. As a result of these collisions, the excitation, dissociation, ionization and recombination of the heavy plasma species occur. A summary schematic of the different types of reactions is presented in Figure 2-8 [94]. The heterogeneous reactions happen between the plasma species and the exposed surfaces. Heavy plasma species may adsorb on the substrate surface or recombine with the species already on the surface to form stable compounds or plasma polymers. Conversely, ions with sufficient energy can sputter the substrate surface.

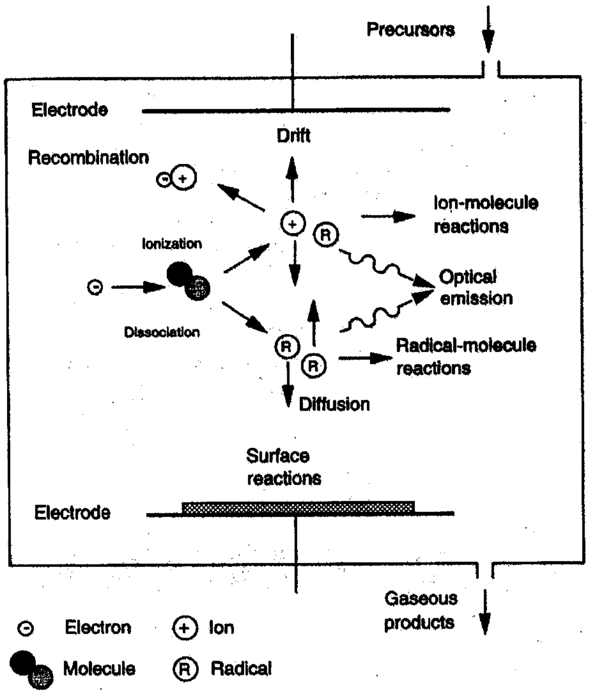

Figure 2-8. Schematic representation of chemical reactions taking place in a plasma reactor [94].

The whole chain of chemical processes taking place in low-pressure plasmas can be broken down into four main steps: initiation, propagation, termination and reinitiation [94, 99]. In the initiation stage, free radicals, atoms and other reactive species are formed by collisions involving energetic electrons and ions with the molecules present in the gas phase, adsorbed on the substrate surface, or chemically combined with the substrate surface. The propagation stage involves the combination of radicals among themselves or between radicals with molecules as well as other reactive species either present in the gas phase or on the substrate surface. In the termination stage, the chemical reactions are similar to those in the propagation stage, but they end with the formation of stable neutral products. However, these neutral products formed in the gas phase or deposited on the substrate surface are exposed to energetic electrons, ions and particles coming from the gas phase, forming radicals, atoms and other reactive species again, thus reinitiating the chemical reactions.

2.3.3.3. Capacitively coupled RF plasma reactor

Non-equilibrium low-pressure plasmas are usually generated by three different techniques: direct-current (DC), radio-frequency (RF) and microwave (MW) electrical discharges in gases. For many applications, it is of little importance which type of discharges is applied as long as nearly identical electron energies and gas temperatures can be obtained [98]. Various kinds of electrical discharges can lead to approximately the same results. Therefore, the choice of desired discharge reactors to generate low-pressure plasmas is based on practical considerations such as stable performance, flexibility, ease of construction and operation, process uniformity and costs. In this project, a capacitively coupled RF (CCRF) plasma is sustained in the mixture of an inert gas and a monomer gas under low pressures. In CCRF plasma reactors using external electrodes, the two electrodes are mounted outside the reactor and thus, do not participate in the plasma chemistry. The electrodes can be in the shape of two rings mounted around the reactors (Figure 2-9 (A)) or two plates placed along the reactor (Figure 2-9 (B)).

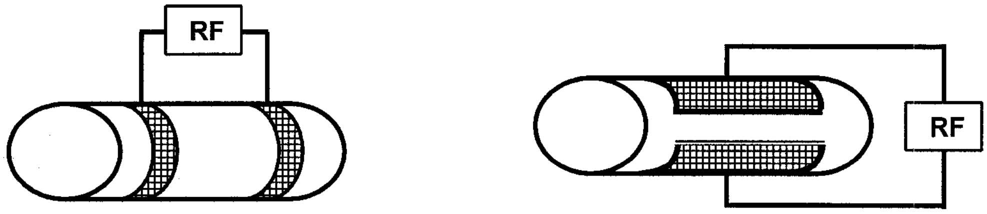

(A) (B)

Figure 2-9. Schematic representation of two kinds of CCRF plasma reactor.

CCRF plasma reactors are characterized by several advantages [81], mainly:

1. The CCRF plasma can be sustained with external electrodes, thus eliminating the contamination of the plasma with materials eroded from the electrodes.
2. The CCRF plasma reactor has the features of simplicity, stability and geometrical flexibility (e.g., capability to fill large-volume plasma chambers).

2.3.3.4. Plasma polymerization from simple hydrocarbon compounds

Plasma polymerization is a highly system-dependent process, meaning that the produced plasma polymers depend strongly on the reactor geometries and operating conditions such as reactor pressure, monomer gas flow rate and RF power. Accordingly, not a unique product can be identified as the plasma polymer from a determined monomer. In other words, depending on the operating conditions, a variety of deposits can be obtained from the same monomer. Also, similar products can be produced from various monomers. For these reasons, the properties of plasma polymers do not strongly depend on the actual source monomers. Several simple hydrocarbon gases such as CH_4 [83, 84, 87, 100], C_2H_2 [89], C_2H_4 [89, 90, 101], C_2H_6 [83, 86, 87, 89, 91, 102], C_3H_8 [83, 87] and C_4H_{10} [83, 87] have been used to produce plasma polymers due to their simple chemical structure and abilities to form *C:H* coatings on substrate surfaces. The produced plasma deposits vary from oily films and soft macromolecular films to extremely hard diamond-like carbon films, or even polycrystalline diamond films. Vora and Moravec [83] presented that the ratio of RF power to reactor pressure plays an important role in the transition from soft plasma polymers to hard plasma polymers. Small ratios lead to the formation of soft plasma polymers, and an abrupt transition in the deposit properties happens when this ratio reaches approximately 100 W $torr^{-1}$.

In the present project, ethane will be used as the source monomer. The plasma polymerization from ethane to form ultrathin solid films by CCRF plasma has been studied for a variety of reactor configurations, and abundant experimental data on the macrokinetic of plasma polymerization from ethane have been reported [83, 86, 87, 89, 91, 102]. However, the operating conditions vary over such a broad range that it is nearly impossible to make meaningful comparisons amongst these data.

Kouprine [103] formed C:H nanometer-thick films on the surface of SiO_2 nanoparticles using a CCRF plasma reactor. Based on the characterization of the coatings and a study of the conditions prevailing in the CCRF plasma reactor, a simplified mechanism for the formation of hydrocarbon coatings on nanoparticles was proposed. This mechanism is schematically presented in Figure 2-10.

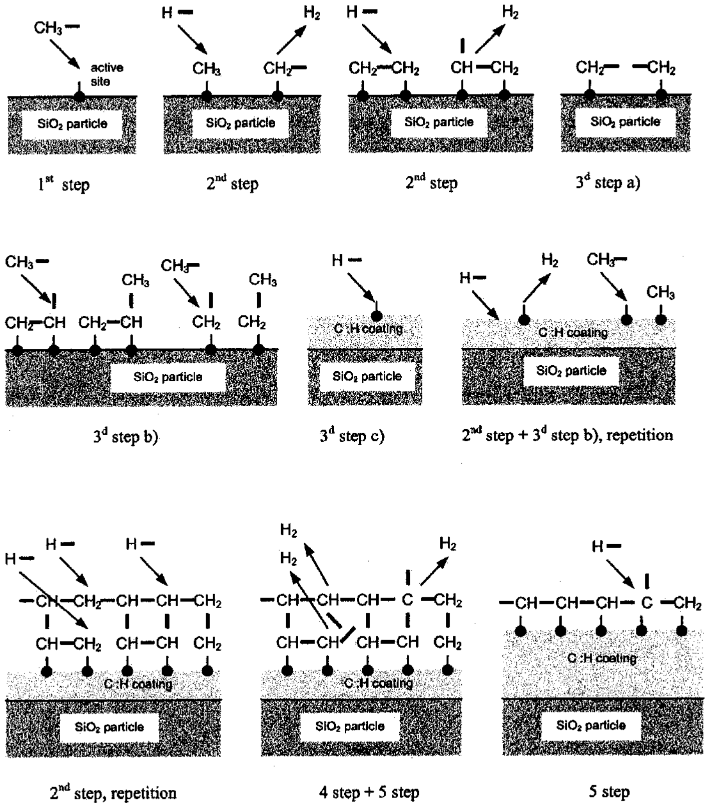

Figure 2-10. Schematic description of the process of plasma polymerization from C_2H_6 in CCRF plasma reactor [103].

Initially, free radicals, most of which are $\cdot CH_3$ radicals, are generated in the CCRF ethane plasma. These radicals then chemically adsorb on the nanoparticle's surface. The incident hydrogen atoms remove hydrogen atoms from the adsorbed radicals or from the already formed deposit via abstraction, thereby creating dangling bond sites on the surface. The adsorption of •CH_3 radicals at the dangling bond sites and the recombination of neighboring dangling bonds lead to the growth of plasma polymer films.

Jensen et al. [91, 92] developed a free-radical reaction mechanism for the deposition of plasma polymers from C_2H_6 monomers in a CCRF plasma. This mechanism includes the initiation, propagation and termination of free radicals both in the gas phase and at the surface of already deposited plasma polymer films. The main chemical reactions taking place in the plasma polymerization from C_2H_6 are summarized in Table 2-1 [92].

Table 2-1. The free-radical reaction mechanism for the plasma polymerization of C_2H_6 in CCRF plasma [92].

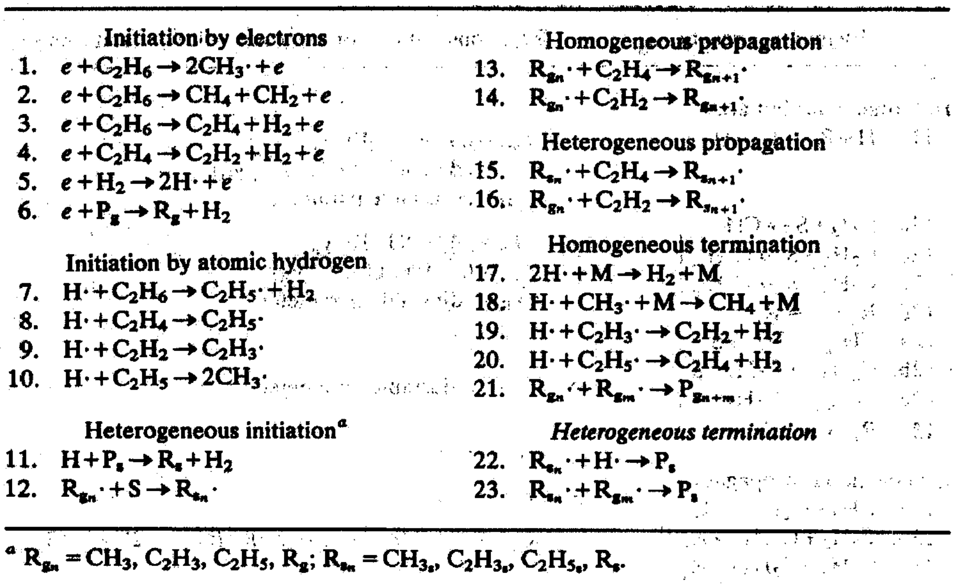

Initiation by electrons

1. $e + C_2H_6 \rightarrow 2CH_3\cdot + e$
2. $e + C_2H_6 \rightarrow CH_4 + CH_2 + e$
3. $e + C_2H_6 \rightarrow C_2H_4 + H_2 + e$
4. $e + C_2H_4 \rightarrow C_2H_2 + H_2 + e$
5. $e + H_2 \rightarrow 2H\cdot + e$
6. $e + P_g \rightarrow R_g + H_2$

Initiation by atomic hydrogen

7. $H\cdot + C_2H_6 \rightarrow C_2H_5\cdot + H_2$
8. $H\cdot + C_2H_4 \rightarrow C_2H_5\cdot$
9. $H\cdot + C_2H_2 \rightarrow C_2H_3\cdot$
10. $H\cdot + C_2H_5 \rightarrow 2CH_3\cdot$

Heterogeneous initiation[a]

11. $H + P_s \rightarrow R_s + H_2$
12. $R_{g_n}\cdot + S \rightarrow R_{s_n}\cdot$

Homogeneous propagation

13. $R_{g_n}\cdot + C_2H_4 \rightarrow R_{g_{n+1}}\cdot$
14. $R_{g_n}\cdot + C_2H_2 \rightarrow R_{g_{n+1}}\cdot$

Heterogeneous propagation

15. $R_{s_n}\cdot + C_2H_4 \rightarrow R_{s_{n+1}}\cdot$
16. $R_{g_n}\cdot + C_2H_2 \rightarrow R_{s_{n+1}}\cdot$

Homogeneous termination

17. $2H\cdot + M \rightarrow H_2 + M$
18. $H\cdot + CH_3\cdot + M \rightarrow CH_4 + M$
19. $H\cdot + C_2H_3\cdot \rightarrow C_2H_2 + H_2$
20. $H\cdot + C_2H_5\cdot \rightarrow C_2H_4 + H_2$
21. $R_{g_n}\cdot + R_{g_m}\cdot \rightarrow P_{g_{n+m}}$

Heterogeneous termination

22. $R_{s_n}\cdot + H\cdot \rightarrow P_s$
23. $R_{s_n}\cdot + R_{g_m}\cdot \rightarrow P_s$

[a] $R_{g_n} = CH_3, C_2H_3, C_2H_5, R_g$; $R_{s_n} = CH_{3_s}, C_2H_{3_s}, C_2H_{5_s}, R_s$.

Gas-phase free radicals are created both by electron-molecule collisions and by the chemical reactions of the produced hydrogen atoms with the monomer molecules such as C_2H_6 and with the produced unsaturated species such as C_2H_4 and C_2H_2. The free radicals at the plasma polymer film surface are created both by the adsorption of gas-phase free radicals and by hydrogen atom abstraction reactions. Numerous C_2H_4 and C_2H_2 molecules are also produced by the dissociation of C_2H_6 monomers and the produced C_2H_4 molecules. The addition of C_2H_4 and C_2H_2 molecules to the free radicals leads to the homogeneous free-radical chain growth in the gas phase and the heterogeneous free-radical chain growth on the already deposited film.

Hiratsuka et al. [87] studied the plasma polymerization from C_2H_6 monomers and obtained a “characteristic map” (Figure 2-11) for this process. They showed that, for their reactor configuration, the products of plasma polymerization are organic powders at low reactor pressures and low monomer gas flow rates, and films at moderately high reactor pressures and over a wide range of monomer gas flow rates. The increase in plasma power tends to enlarge the region inside which organic powders are formed and enhances the stability of the discharge.

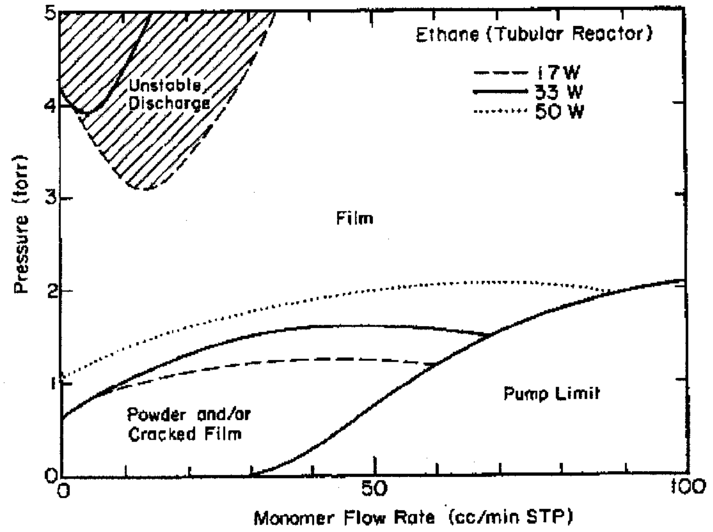

Figure 2-11. Characteristic map for plasma polymerization of ethane in Hiratsuka’s reactor [87].

Chapter 3

Dual-plasma system for the synthesis of organic layer-coated metal nanoparticles

A novel apparatus for synthesizing plasma polymer-coated metal nanoparticles was designed and constructed. Its design was based on a review of various synthesis methods for coated metal nanoparticles, previous modeling work related to the generation of metal nanoparticles by homogeneous nucleation from evaporated metal vapors [104], and in-house experience gained with the plasma polymerization from ethane [105]. Design considerations, system components and operating ranges are presented in this chapter.

3.1. Design considerations

In this project, the cathodic arc evaporation/condensation from a solid metal source combined with plasma polymerization from a simple hydrocarbon is selected as the method for generating metal nanoparticles coated with an ultrathin organic coating. The metal nanoparticle synthesis process is followed by the plasma polymerization process in a closed system to avoid contamination of condensed bare metal nanoparticles by unwanted sources (e.g. air or water vapors) and to achieve the low-pressure conditions required by both processes. The whole system is axisymmetric and set up vertically with the cathodic arc evaporation section located at the bottom while the plasma polymerization section rests above it. An inert gas flows through the whole system to transport the generated metal particles and possibly diffused metal vapors, to cool and condense them and to dilute the aerosol of the produced metal nanoparticles. Due to different constraints on the experimental conditions associated with the cathodic arc evaporation and plasma polymerization processes, design trade-offs had to be made to achieve a stable operation of the system and to obtain the desired product.

The system stability was a main consideration throughout the design and testing of the dual-plasma reactor. The stability of the pulsed DC arc plasma source and the CCRF plasma were investigated. Strategies to achieve the stable operation are discussed in the following sections. Other improvements for increasing the nanoparticle production yield, controlling the average size of produced nanoparticles, and generating smooth, uniform and dense plasma polymer films are made within the stable operating range.

Besides the system stability, reactor safety and flexibility considerations were also taken into account. High voltages (0-1000 V), high currents (0-200 A) and radio-frequency fields (13.56 MHz), which all represent significant dangers to the operator, are used within the system. Therefore, many precautions such as grounding the whole system and shielding the reactor were taken. As to the flexibility of the reactor, experimental components are intentionally designed so that they can be easily changed or adjusted according to the requirements of various experiments.

3.2. General description of the experimental set-up

Two photographs and a schematic of the final configuration of the dual-plasma reactor used for the synthesis of plasma polymer-coated metal nanoparticles are shown in Figure 3-1. The set-up features two main components: a low-pressure pulsed metal arc system for the synthesis of metal nanoparticles and an in-flight plasma polymerization system for the *in-situ* deposition of an organic layer onto the produced metal nanoparticles. Metal nanoparticles are produced from a solid source via the evaporation of the metal cathode of a low-pressure metal vapor arc system followed by the supersaturation/condensation of the generated metal vapors within the plasma/inert gas boundary zone (Ar in this study). The same inert gas is used to transport the produced metal nanoparticles into a capacitively-coupled RF (13.56 MHz) plasma where in-flight plasma polymerization of an organic layer from an organic monomer takes place. In this study, ethane (C_2H_6) is used as the gaseous monomer source because it is known to form plasma polymer films over a wide range of plasma processing conditions, and it involves relatively simple gas-phase products whose chemistry is relatively well understood.

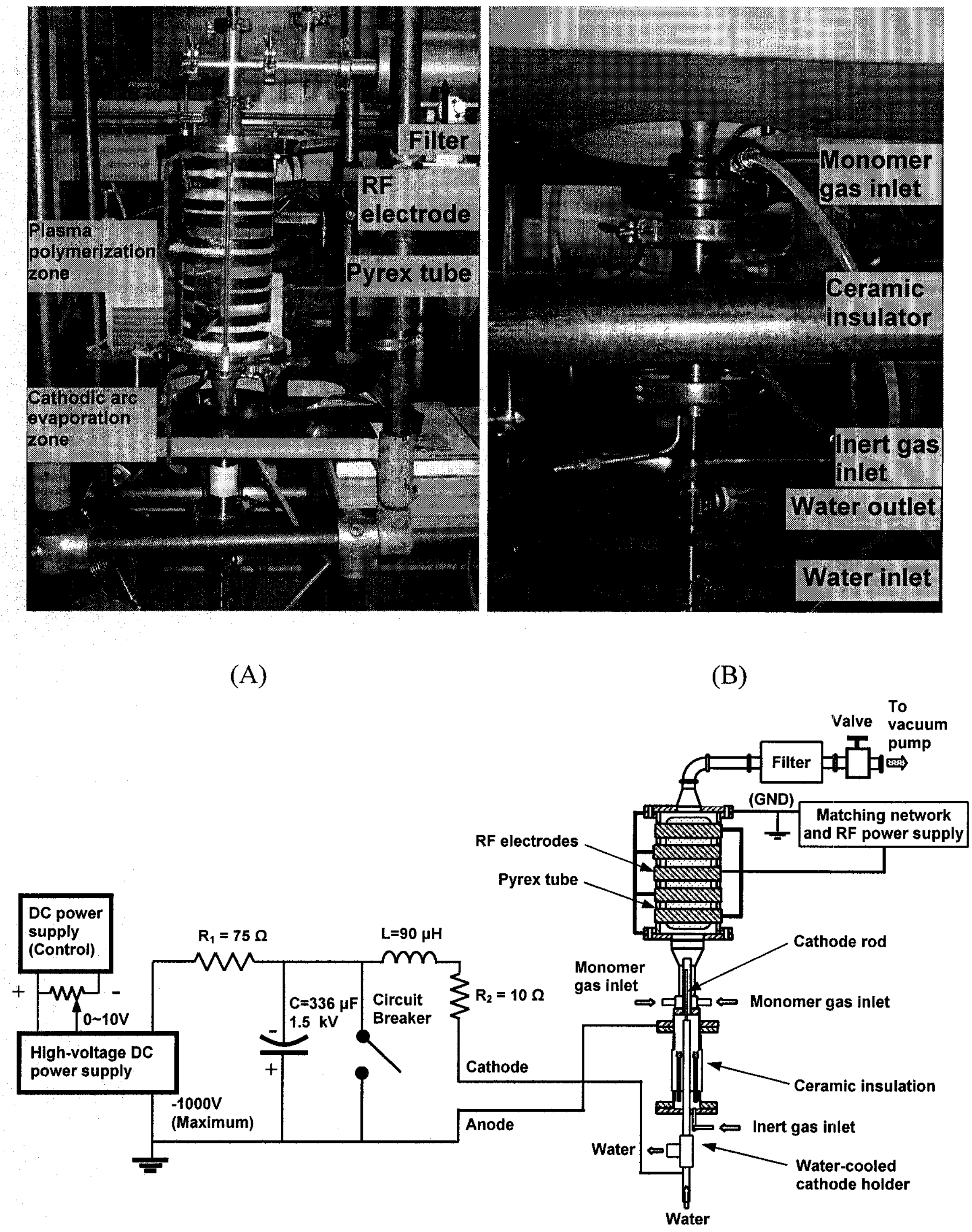

Figure 3-1. Photographs and schematic of the dual-plasma reactor. (A) Whole reactor. (B) Lower section of the reactor. (C) Schematic of the set-up with the electrical circuit. Numerical values for the electrical components are given.

The ability to perform both the metal nanoparticle synthesis and the coating formation processes in the same reactor limits the agglomeration of the bare metal nanoparticles as well as the contamination from the environment. The reactor pressure is maintained in the 1-20 torr range in order to accommodate the operating requirements of both processes. The produced nanoparticles are collected over various packings such as polymer and paper filters, and silica wool placed inside the flow line.

3.3. Cathodic arc evaporation/condensation section

A detailed schematic of the cathodic arc evaporation/condensation system is illustrated in Figure 3-2. In the cylindrical plasma reactor, a 0.25" (6.35 mm)-diameter by 1.25" (31.75 mm)-length metal rod (McMaster-Carr, 99.99% purity copper in the present study) is mounted along the axis as the cathode (metal precursor source) of the pulsed electric arc system, while a stainless steel tube assembly surrounding the metal cathode is used as the anode. Before arcing, the inter-electrode gap thickness is 1 mm. The cathode assembly is negatively charged while the anode assembly is grounded. The cathode and anode are electrically insulated from each other by a ceramic insulation tube. The inert gas (Argon, MEGS, ultra high purity 99.999%) is introduced through the bottom flange of the reactor and flows upward through the inter-electrode gap. An expansion zone connects the arc evaporation section and the downstream end of the plasma polymerization section. Since extremely hot cathode spots are formed on the cathode surface, a water-cooled cathode holder was designed to keep the cathode rod cool and to achieve high nanoparticle production yield. The temperature of the stainless steel anode assembly does not reach high values due to its relatively large volume (and correspondingly high surface area) and effective heat transfer through its surface.

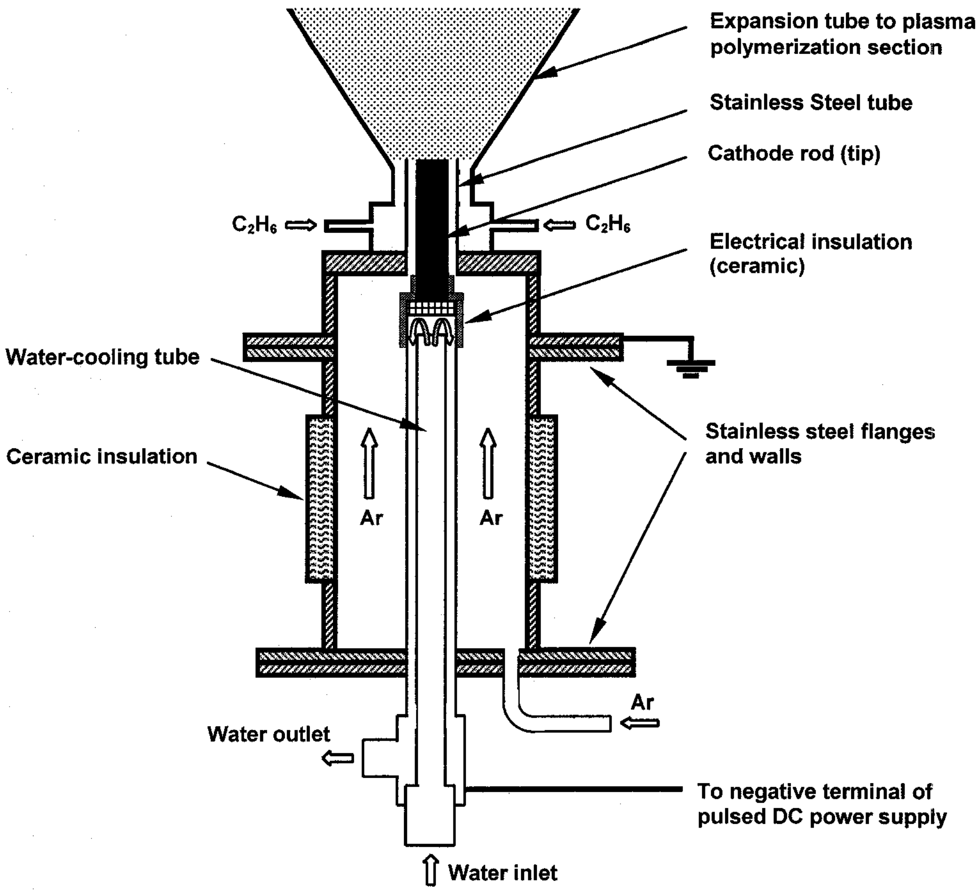

Figure 3-2. Schematic of the cathodic arc evaporation/condensation section making use of a water-cooled cathode holder. Argon (Ar) and ethane (C_2H_6) were used as the inert gas and monomer gas sources, respectively.

In practice, arc discharges occur in the gap defined by the cathode rod and the stainless steel sleeve anode. Pulsed arcs of millisecond duration, peak arc current levels up to 100 A, and repetition frequencies of 5 to 28 Hz are produced with a homemade self-oscillating pulsed power supply (section 3.4). For typical operating conditions (reactor pressure of 1-20 torr and peak arc current of 30 A), the estimated steady-state radius of the metallic plasma/vapor cloud is 4-5 mm (Section 4.4.3). Due to the decay of the arc current during a given current pulse (Figure 3-5 (C)), this radius eventually reduces to the one associated with the minimum current value needed to sustain the arc discharge between the two electrodes. Below this current threshold, the arc discharge stops.

Assuming the temperature of the metallic plasma is approximately 1 eV and the width of the plasma/argon boundary zone is approximately 1 mm [53], one estimates a value of 3×10^{9} K s^{-1} for the cooling rate in the boundary zone. When the steady-state radius of the metallic plasma expansion is smaller than the inter-electrode gap (~1 mm), the produced metal vapors homogeneously nucleate within the metallic plasma/gas boundary zone (Figure 3-3 (A)). When this radius is larger than the inter-electrode gap, the confined metallic plasma contacts the anode. As a result, the beam of high-energy metal ions/atoms within the metallic plasma bombards the anode inside surface, producing a metal coating and generating nanoparticles, most likely from the high surface mobility of the atoms [106]. However, within the remaining of the plasma/gas boundary zone which does not get into contact with the anode, homogeneous nucleation of the metal vapor happens. The metallic plasma expansion cloud and the expected zones of particle formation are schematically shown in Figure 3-3. In addition, it is likely that some metal vapors diffuse out of the metallic plasma into the inert gas, and subsequently cooled by the same gas to form metal nanoparticles within it. The airborne metal nanoparticles are transported upwardly into the plasma polymerization section by the inert gas.

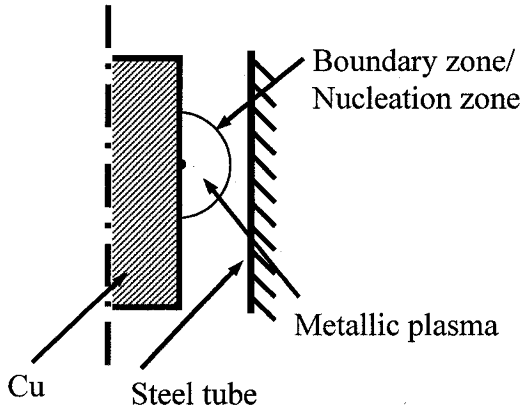

(A)

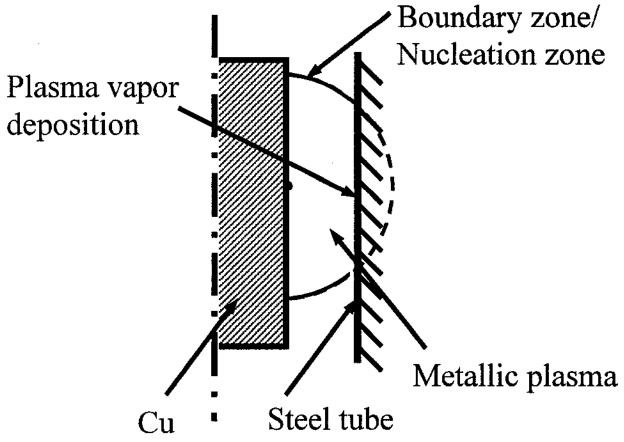

(B)

Figure 3-3. Schematic of the metallic plasma expansion cloud and the expected zones of particle formation. (A) The steady-state radius of the metallic plasma expansion is smaller than the inter-electrode gap; (B) The steady-state radius of the metallic plasma expansion is larger than the inter-electrode gap.

3.3.1. Electrical insulation

The main features of the electric circuit used for the cathodic arc evaporation/condensation section will be presented in section 3.4. All reactor walls and flanges are grounded, while the cathode assembly, including the water-cooling tubes and flanges, is connected to the negative terminal of the pulsed DC power supply. In this arrangement, only a small exposed section of the reactor system is not grounded, thus providing safe operating conditions. The electrical insulation between the cathode and anode electrodes is achieved by isolating the two assemblies with a ceramic to metal adapter (MDC Vacuum, model K200-CB), which features high-voltage insulation capabilities.

Since arc discharges tend to occur in the shortest inter-electrode gap, the cathode to anode distance in the cathodic arc evaporation section was kept minimal in the region defined by the cathode rod and the anode sleeve. On the other hand, it was found in preliminary experiments that arc discharges can form between the edge of the water-cooling tube (cathode) and the stainless steel sleeve (anode). Thus, an electrical insulation (ceramic tube) was added over the downstream end of the water-cooling tube to eliminate this problem.

3.3.2. Water-cooled cathode holder and cathode tip

Due to the small surface area of the cathode tip exposed to the surrounding cool inert gas, the concentrated input power of the cathode spots could not be effectively dissipated. As a result, the cathode tip was heated to high temperatures. Although a pulsed DC power supply (section 3.4) is used to decrease the average heat load imposed on the cathode tip, the tip melted when the system was operated at high pulsing frequencies and high arc peak currents. For this reason, a water-cooled cathode assembly has been designed to achieve efficient heat transfer from the cathode tip, yet maintaining high metal vapor production rates. The water-cooled cathode assembly, schematically illustrated in Figure 3-2, features a double-wall stainless steel tube arrangement with a stainless steel screw welded on its end to secure the changeable cathode tips. The inner diameters of the two tubes are approximately 5 mm and 7.5 mm, respectively. The length of the screw is 8 mm. Cold water enters the inner tube, reaches the holding screw before it leaves the assembly through the annular space defined by the two tubes. The typical water flow rate is 750 mL min^{-1}. Cathode tips are secured at the top of the water-cooled cathode holder.

3.3.3. Expansion and gas/nanoparticle contact zone

A stainless steel funnel connects the cathodic arc evaporation/condensation section to the plasma polymerization section. The inner diameters of the two ends of this expansion tube are 0.75" (19.05 mm) and 1.5" (38.1 mm), respectively while its length is 2" (50.8 mm). When initially condensed metal nanoparticles and possibly diffused metal vapors enter the expansion zone, their concentrations are reduced so as their collision rates, thus limiting the agglomeration of metal nanoparticles. A monomer gas (C_2H_6 in the present study, Matheson, chemically pure grade 99.0%) is vortically introduced at the base of the funnel and mixes with the condensed metal nanoparticles and the inert carrier gas. The mixture is formed in the expansion/condensation region before it reaches the plasma polymerization chamber.

3.4. Pulsed DC power supply

3.4.1. Motivation and operation principle

The necessity to use a pulsed DC power supply with the cathodic arc evaporation source has been explained in Chapter 2. In contrast to continuous arc operation, pulsed arc operation allows to maintain high arc evaporation rates while limiting the formation of liquid volumes under the cathode spots, which in turn leads to the formation of macroparticles even at relatively modest power levels. The operating principle of the pulsed DC power supply is based on the arc-triggered charging and discharging of a high-voltage capacitor whose terminals are connected with the cathode and anode of the arc evaporation reactor through a RLC circuit. The capacitor is charged by a high-voltage power supply until the voltage across the inter-electrode gap (i.e. capacitor voltage) reaches the breakdown level. Then, an arc discharge forms between the two electrodes, rapidly discharging the capacitor. Upon extinction of the arc plasma, the capacitor is charged again until a new breakdown event occurs. As a result, this process self-oscillates, leading to the formation of a periodic train of pulsed arcs.

3.4.2. Construction of the pulsed DC power supply

A schematic and photographs of the homemade pulsed DC power supply are shown in Figure 3-1 and Figure 3-4, respectively. A high-voltage capacitor (General Atomics, C=336 μF, 1.5 kV maximum) is being continuously charged by a 1.5 kW capacitor-charging power supply (Analog Modules, model 5723-1000N, maximum (negative) voltage of -1000 V). When the voltage across the inter-electrode gap (1 mm) reaches the breakdown level of the system (approximately -300 V at 10 torr), the capacitor discharges through the gap, forming an electric arc, which severely erodes the cathode surface due to the action of the cathode spots. Under nominal conditions, a 75 Ω resistor is used to limit the capacitor-charging current and pulsing frequency, while the discharging current is limited to a peak value of approximately 30 A by a 10 Ω ballast resistor. A homemade inductor (L=90 μH) placed in the discharging circuit loop is used to stabilize the train of pulsed arcs. The stability of the discharging circuit is discussed in Section 4.2.

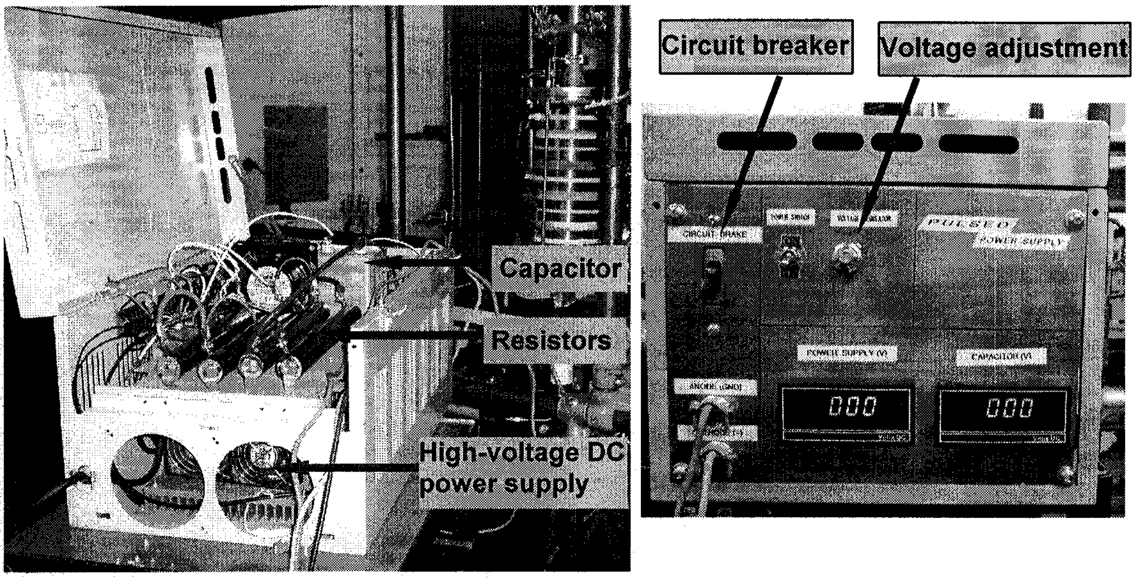

(A) (B)

Figure 3-4. (A) Photograph of the pulsed DC power supply. (B) Front panel.

The charging and discharging circuit resistances can be adjusted by a simple replacement of the power resistors. These resistors are cooled with the help of an electric fan mounted inside the power supply. All components of the pulsed DC power supply are enclosed in a metal box which is grounded. The output voltage of the capacitor-charging power supply is adjusted through a potentiometer. The values of the output voltage of the capacitor-charging power supply and voltage across the capacitor are displayed using LED displays mounted on the front panel, as shown in Figure 3-4 (B). A circuit breaker is used as an on-off switch to short the high-voltage capacitor.

When the circuit breaker is in the "OFF" position, the high-voltage capacitor is allowed to charge. When the circuit breaker is in the "ON" position, the high-voltage capacitor is shorted.

3.4.3. Arc voltage and current waveforms

Figure 3-5 shows typical arc voltage and current waveforms measured with a digital oscilloscope (Tektronix, model TDS2024) equipped with a high-voltage probe (Tektronix, model P6015A, 1000X) and a current transformer coil (Pearson electronics, model 411, 100 mV A^{-1}), respectively. The operating conditions were: cathode-anode gap of 1 mm, Ar flow rate of 400 sccm, pressure of 10 torr, charging resistance of 75 Ω and discharging resistance of 10 Ω. The slowly descending portion of the voltage pulse is associated with the charging process, while the rapidly ascending portion is associated with the discharging process. Under these conditions, the breakdown voltage of the system is approximately -300 V. The reported values of the breakdown voltage of argon in the geometry of plane-parallel copper electrodes are in the 200-300 V range for a *pd* product of 10 torr•mm (1.33 Pa•m) [107]. The breakdown voltage obtained in our system is in agreement with these numbers, though the electrode geometry is slightly different [108]. The current pulses (Figure 3-5 (B)) stand out of the base line with a frequency of approximately 10 Hz. Figure 3-5 (C) shows an enlarged view of a current pulse. The peak of the arc current is approximately 27 A, and the current pulse duration is approximately 3 ms. Due to the coupling effect caused by the current variation in the capacitor, inductor and the resistors, slight noises are found in the waveforms of the arc currents and voltages.

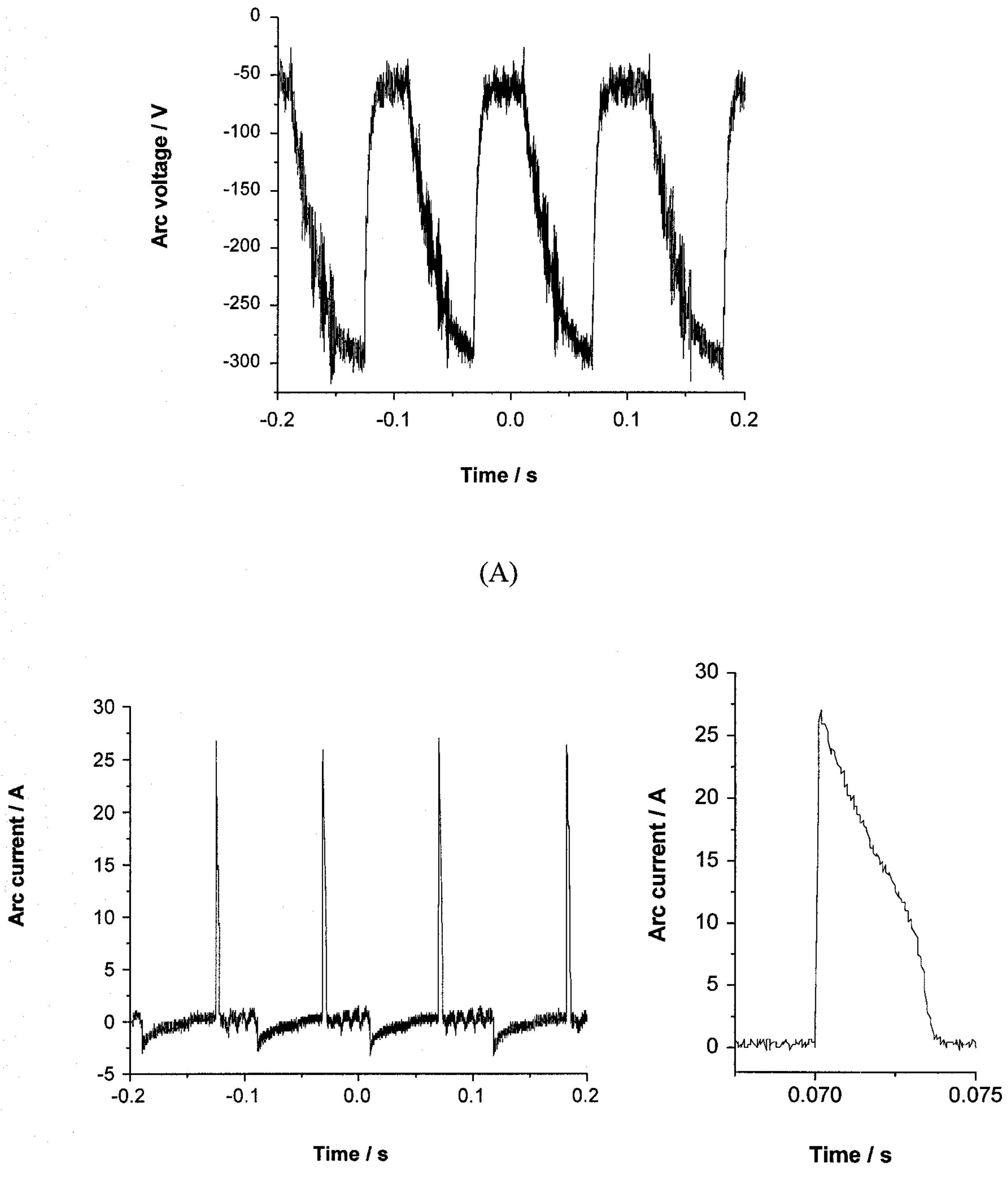

(A)

(B)

(C)

Figure 3-5. Typical charging capacitor voltage (A) and arc current (B) waveforms. Enlarged view of one current pulse (C).

3.5. Plasma polymerization reactor

A schematic of the plasma polymerization section is shown in Figure 3-1. The plasma confinement tube consists of a Pyrex tube (114 mm I.D. by 305 mm height), vacuum-sealed with two stainless steel end flanges, and wrapped with five thin copper sheets (38 mm wide). Both end flanges and two of the copper sheets are used as ground electrodes, while the other three copper sheets are used as RF electrodes. In the current arrangement, the live and grounded electrodes alternate with a spacing of approximately 12 mm to sustain a large and uniform plasma volume whose capacitive impedance falls in the tuning range of the RF matching network. A Dressler RF power supply (model Cesar 1312, 13.56 MHz, 0-1200 W, RF pulse frequency range of 1-30 kHz, RF pulse duty cycle range of 0-99%) connected with a matching network (Dressler, model VARIOMATCH) to produce the CCRF plasma. Ethane is used as the organic monomer source. The residence time of the monomer gas in the plasma polymerization reactor is in the 12-2.4 s range with the Ar flow rate ranging from 200 to 1000 sccm at a pressure of 10 torr. Since the calculated values of the Reynolds number of the gas flow in the Pyrex tube are less than 20 with gas flow rates in the 200-1000 sccm range and a reactor pressure lower than 10 torr, a laminar flow develops in the Pyrex tube.

3.5.1. RF electrodes

The RF electrodes are made of 38 mm-wide copper sheets wrapped around the Pyrex tube. The main concern about the arrangement of the RF electrodes was to make sure that a stable RF plasma filled the whole volume of the Pyrex tube. A capacitively-coupled RF plasma can be electrically represented as a diode, a resistor and a capacitor mounted in parallel, as shown in Figure 3-6 (A). A typical impedance-matching L-network using a fixed inductor and two variable capacitors is schematically shown in Figure 3-6 (B). The fixed inductor is connected in series with two variable capacitors, thus allowing to vary the inductance L by adding or subtracting an opposite reactance. The function of the impedance-matching network is to transform the resistive and capacitive characteristics of the CCRF plasma to a constant resistive value (e.g. 50 Ω).

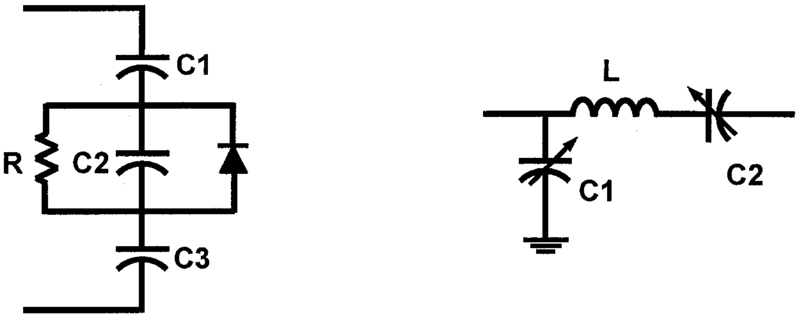

(A) (B)

Figure 3-6. (A) Simplified model of a capacitively-coupled RF plasma. (B) Schematic drawing of the impedance-matching network.

In exploratory experiments, one or three copper sheets were used, the impedance of the CCRF plasma inside the Pyrex tube could not be matched within the available range of the impedance-matching network (resistive part: 1.3 to 45 Ω and reactive part: -j220 to +j50 Ω), which resulted in high reflected RF power to the RF power supply and caused instabilities of the RF plasma inside the Pyrex tube. When five electrode sheets are used, the impedance of the RF plasma is properly matched, and a uniform and stable RF plasma is formed.

3.5.2. Shielding for the RF electromagnetic radiation

Although the RF plasma is formed inside the Pyrex tube, the RF electromagnetic field can strongly disturb the functioning of mass flow controllers and pressure gauges used with the system. Furthermore, exposure to the RF electromagnetic field can bring possible hazards to human health such as headache and palpitation. Therefore, the RF plasma chamber needed to be completely shielded, preventing the harmful effects from the RF electromagnetic field. In practice, a copper cylinder (0.5 mm in thickness) was made to enclose the whole RF plasma chamber. Since the skin depth for copper at 13.5 MHz is approximately 0.02 mm [109], the thickness of this copper cylinder is sufficient to shield the internal RF electromagnetic field. In addition, shielded cables are used to connect the mass flow controllers and pressure gauges to the computer. All shields are grounded in order to avoid any charge build-up.

3.6. Nanoparticle collection

In order to observe the plasma inside the reactor or collect samples of the produced nanoparticles, the elbow tube located on top of the conical section of the system (Figure 3-1) was sometimes replaced by a stainless steel cross tube equipped with a quartz view port or an electrically-insulated electrical feedthrough. Two different collection approaches were used to collect nanoparticles from the exhaust stream of the reactor. The collection locations are illustrated in Figure 3-7.

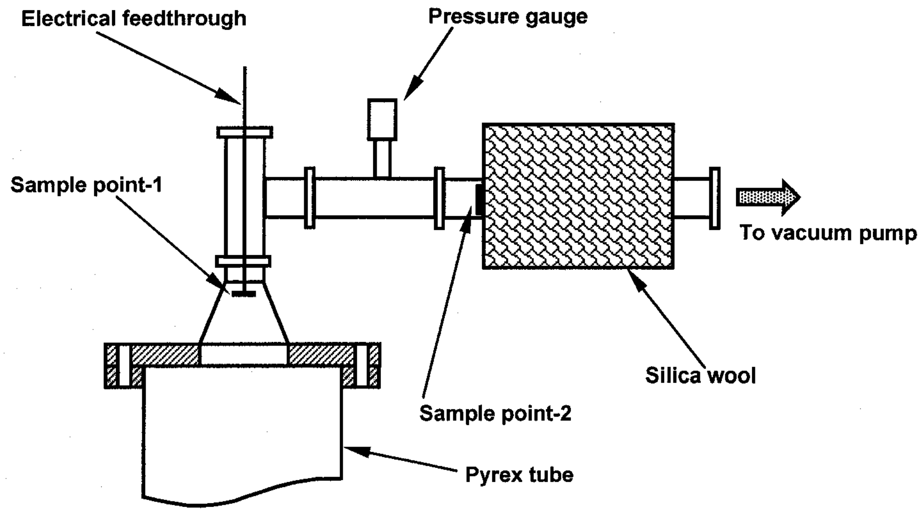

Figure 3-7. Schematic of the nanoparticles collection systems and locations.

As can be seen, the first collection point (sample point-1) was located inside the conical section of the vacuum line following the Pyrex tube. A piece of a copper sheet mounted at the end of an electrical feedthrough was used as collecting surface. The electric feedthrough was positively charged to strengthen the collection efficiency of metal nanoparticles through the electrostatic force. The bias voltage used was +100 V. The deposited metal nanoparticles were scratched off the copper sheet for further analyses. Carbon-coated TEM grids were attached to the copper sheet for the collection of nanoparticles for TEM analyses. The specimen for FT-IR analyses were collected by using KBr plates instead of TEM grids.

The second collection point (sample point-2) was located at the entrance of the filter filled with silica wool. Ultrafine polymer filters (~25 nm average pore size) were placed perpendicular to the flow direction. The nanoparticles were captured by the polymer filters for further analyses. Since the largest pores of the polymer filter are larger than the produced copper nanoparticles, it is suspected that nanoparticles penetrate into the filter and deposit on the fibrous structure without size selection. It is thus assumed that the particle size distribution obtained from the particles collected onto the filter surface is representative of the actual distribution. The measurement of the metal nanoparticle size is based on the visual inspection of FE-SEM images of the collected particles. For FE-SEM analyses, small pieces of the polymer filters hosting deposited nanoparticles were coated with a thin layer of gold (~4 nm in thickness) to make their surface electrically conductive. Generally, the metal nanoparticles collected from the two collection points showed no difference in their dimensions. Nanoparticles were also captured by the silica wool packed inside the filter chamber.

3.7. Gas and data handling

All the connections among the stainless steel components are made via compression O-ring seals. A rotary vane vacuum pump (Alcatel, model Pascal 2005SD) combined with a manual vacuum valve (MDC Vacuum, model KAV-100) are used to obtain the required vacuum conditions. The base pressure of the system is 0.008 torr (~1 Pa). The reactor pressure is measured by a pressure gauge (MKS Instruments, model HPS series 910, Dualtrans^{TM} MicroPirani/Absolute Piezo Transducer). Two mass flow controllers (Brooks, model 5850E) with 0-2000 sccm and 0-100 sccm ranges are used to meter the argon and ethane flow rates, respectively. The pressure gauge and the two mass flow controllers are powered by an OMRON S82K-00727 power supply and two OMRON S82K-00728 power supplies, respectively. The data acquisition and control is achieved using a National Instrument LabView^{TM} virtual instrument running on a personal computer. A shielded data acquisition card (National Instruments, SCB-100/BRD) is used to transmit analog signals between the pressure gauge and mass flow controllers, and the personal computer. The readings of the pressure gauge and mass flow controllers are displayed in the LabView^{TM} interface.

Chapter 4

Synthesis of metal nanoparticles

4.1. Introduction

The synthesis of uncoated metal nanoparticles is considered in this chapter. As such, no monomer gas was introduced into the plasma polymerization chamber and the CCRF plasma was not turned on. Copper (McMaster-Carr, 99.99% purity) was used as the metal source while argon (MEGS, ultra high purity 99.999%) was used as the inert gas to cool down and transport the produced metal vapors/nanoparticles.

This chapter is presented as follows. First, the experimental procedure for operating the cathodic arc evaporation system is described in detail. Next, the stability of the pulsed DC arc discharges is discussed and the cathode erosion rates are estimated. The steady-state radius of the expanding metallic plasma and the density of metal vapors within the plasma are calculated. The morphology of the produced copper nanoparticles is characterized by FE-SEM and TEM microscopy. Finally, the effects of experimental conditions such as the reactor pressure and inert gas flow rate on the nanoparticles' size and size distribution are investigated.

4.2. Experimental procedure

4.2.1. Preparation stage

1. The cathode rods and the interior of the Pyrex tube are cleaned with water and acetone. The interior of the stainless steel sleeve anode and connecting flanges are cleaned with a brush. A new cathode rod is mounted at the top of the water-cooling tube. In order to collect nanopowder samples for analyses, a piece of copper sheet or a TEM grid is attached at the end of the electrical feedthrough located at the first collection point, or a piece of polymer filter is placed at the second collection point.

2. The whole cathodic arc evaporation reactor is re-assembled. The two wire terminals of the pulsed DC power supply are connected to the cathode and anode. The high-voltage probe (Tektronix, model P6015A, 1000X) and the current transformer coil probe (Pearson electronics, model 411, 100 mV A^{-1}) are connected to two input channels of the digital oscilloscope (Tektronix, model TDS2024).
3. After the system is completely set up, the reactor is evacuated to the base pressure (typically, 0.008 torr (~1 Pa) after 30 minutes). Then, argon is introduced into the system at a pre-set gas flow rate. The reactor pressure is regulated to the required value by adjusting the opening of the vacuum valve. Cold water runs through the water-cooled cathode holder.

4.2.2. Experiments

1. Turn on the pulsed DC power supply with the circuit breaker in the "ON" position (for safety consideration). Make sure the voltage control potentiometer is in the "ZERO" position. Switch the circuit breaker to the "OFF" position and slowly increase the charging voltage across the capacitor until an arc discharge train initiates.
2. Monitor the pulsed arc voltage and circuit current waveforms displayed on the digital oscilloscope in order to detect any anomalous operation of the pulsed power source. The arcing frequency can be estimated from these waveforms. This arcing frequency can be further increased by increasing the output voltage of the capacitor-charging power supply.
3. The experiments are carried out for certain durations, for example, 30 or 60 minutes. At the end of the experiment, the pulsed DC power supply is turned off and the argon is allowed to flow for additional 10-15 minutes in order to cool down the system. The cooling water is also allowed to flow for an additional 10-15 minutes to bring the cathode rod to room temperature.
4. Close the vacuum valve with the argon still flowing. Then, turn off the argon flow when atmospheric pressure is reached inside the reactor.
5. Dismantle the reactor. Remove the sample collectors and store them.

4.2.3. Experimental conditions

The main experimental conditions are displayed in Table 4-1.

Table 4-1. Summary of the experimental conditions

Duration	30-90 min
Reactor pressure range	2.5-500 torr
Argon flow rate	200-2000 sccm
Arc pulse frequency	~22 Hz
Arc peak current	10-100 A

4.3. Stability of the pulsed arc plasma source

Since the surface of the cathode metal rod is evaporated by the action of cathode spots, it is of primary importance to sustain their formation. Under the action of a stable train of pulsed arc discharges, the cathode surface is strongly eroded and metal vapors are continuously produced. When the stability of the pulsed arc source is intermittent, the arc discharge sometimes evolves into a stable DC glow discharge following a breakdown event such that the current pulsations terminate and metal vapors are hardly produced. For this reason, the generation of a stable train of pulsed arc discharges is a prerequisite for the high and consistent production of metal vapors.

Preliminary experiments revealed that the presence of an inductor in the discharging circuit loop of the pulsed DC arc power supply plays an important role in stabilizing the train of pulsed arcs. Without an inductor, the train of pulsed arc discharges was unstable and momentarily stable DC glow discharges were often formed. With an inductor in the discharging circuit loop, the pulsed arc system was consistently stable.

The effect of the inductor in the discharging circuit loop can be analyzed on the basis of the formation of discharging current channels between the two electrodes. In theory, the presence of an inductor in the discharging loop influences the behavior of the circuit current, mostly at the beginning of the capacitor discharge since the rate of change of the circuit current (*di/dt*) is then the largest. For this reason, one can compare the dynamics of the capacitor discharge with and without the inductor assuming that, after the breakdown of the inter-electrode gap, the arc discharge channel forms a low resistance path due to the high current density cathode spots [110]. Without the inductor present in the discharging circuit loop, the circuit current can be expressed with the following equation:

$$i_1(t) = \frac{V_B}{R_2} e^{\frac{-t}{R_2 C}} \tag{4-1}$$

where V_B is the breakdown voltage of the inter-electrode gap, R_2 is the ballast resistor in the discharging circuit loop, and C is the capacitance of the high-voltage capacitor. The discharge time constant, R_2C (~3 ms), and initial circuit current, V_B/R_2, can be adjusted through the resistor R_2. With the inductor present in the discharging circuit loop, the circuit current is expressed with the following equation:

$$i_2(t) = \frac{V_B}{\overline{\omega}_0 L} e^{\frac{-R_2}{2L}t} \sinh(\overline{\omega}_0 t) \tag{4-2}$$

with $\overline{\omega}_0 = \sqrt{\left(\frac{R_2}{2L}\right)^2 - \frac{1}{LC}}$.

where L is the inductance of the inductor. Equations (4-1) and (4-2) are plotted in Figure 4-1 (A) using a logarithmic scale for the time and for a typical configuration using $R_2 = 10\ \Omega$, $C = 336\ \mu\text{F}$, $L = 90\ \mu\text{H}$, and $V_B \approx 300$ V.

As can be seen in Figure 4-1 (A), the behaviors of $i_1(t)$ and $i_2(t)$ are noticeably different during the beginning of the capacitor discharge process: $i_1(t)$ monotonically decays from the initial value of 30 A with a time constant of ~3 ms, while $i_2(t)$ first increases from zero to its maximum value of about 30 A over a time interval of ~30 μs before it decays following the same trend as $i_1(t)$. Since the initial current rise occurs over quite a smaller time scale than its decay, a straight ascending line rather than a curved ascending behavior is evidenced when $i_2(t)$ is plotted using a linear time scale (Figure 4-1 (B)). A comparison of Figure 4-1 (B) to Figure 3-5 (C) reveals that the simple model for the capacitor discharge accounts reasonably well for the actual dynamics.

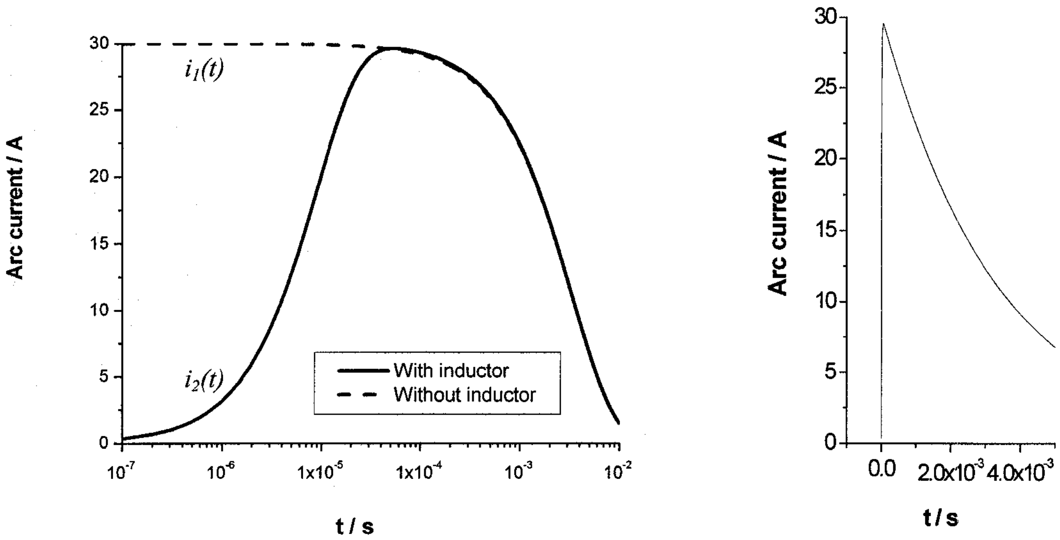

(A)

(B)

Figure 4-1. (A) Model prediction of the discharge current pulse with and without the inductor present in the discharging loop (logarithm scale for time). (B) The same discharging current pulse as a function of real time.

The initial ascending behavior of the discharging current pulse with an inductor present in the loop appears to be beneficial to the consistent formation of arcs. We attribute this phenomenon to the dynamics of cathode spot ignition, which involves the formation of low-pressure arc spots in a microsecond time scale [43, 111]. With the inductor present in the discharge loop, the lag in the current rise gives enough time for the local heating of the cathode surface and the formation of cathode spots [112], which in turn provide conditions for high electron emission through thermo-field emission. Without the inductor present in the discharge loop, a low-current DC glow discharge may form in the inter-electrode gap since there is no means to establish the high electron emission flux conditions. In fact, in the glow discharge regime, the electron emission from the cathode surface is assumed by secondary electron emission [108], which process can be sustained at low cathode surface temperatures, providing a considerably lower electron emission flux. Actually, it was found that the capacitor can not be completely discharged when the glow discharges were formed. That is, a voltage around -100 V was constantly maintained between the cathode and anode when the glow discharges happened. It is noteworthy to report that this stability problem tended to vanish with long arcing times since the ignition of cathode spots is favored on aged (i.e. roughened) cathodes.

4.4. Erosion rate

4.4.1. Macroparticles and nanoparticles produced from the cathodic arc evaporation

Due to the high concentration of power density (~10^{10} W m^{-2}) [55] and correspondingly high surface temperature under cathode spots, small molten pools are formed on the cathode surface. Macroparticles (>100 nm) are splashed away from these molten metal pools due to the high local plasma pressures, thus leaving numerous craters on the cathode surface. FE-SEM images of characteristic craters formed by the cathode spots are shown in Figure 4-2. Craters with a diameter of approximately 10 μm are scattered over the eroded cathode surface. Metal nanoparticles with diameters smaller than 50 nm and macroparticles ranging in diameter from 100 nm to 1 μm deposited on the rim and concave surfaces of the craters. The macroparticles are associated with the displacement of liquid volumes upon cathode spot extinctions. The nanoparticles are formed both from the expulsion of liquid in the nanometer range [113] and, more likely, from the condensation of produced metal vapors.

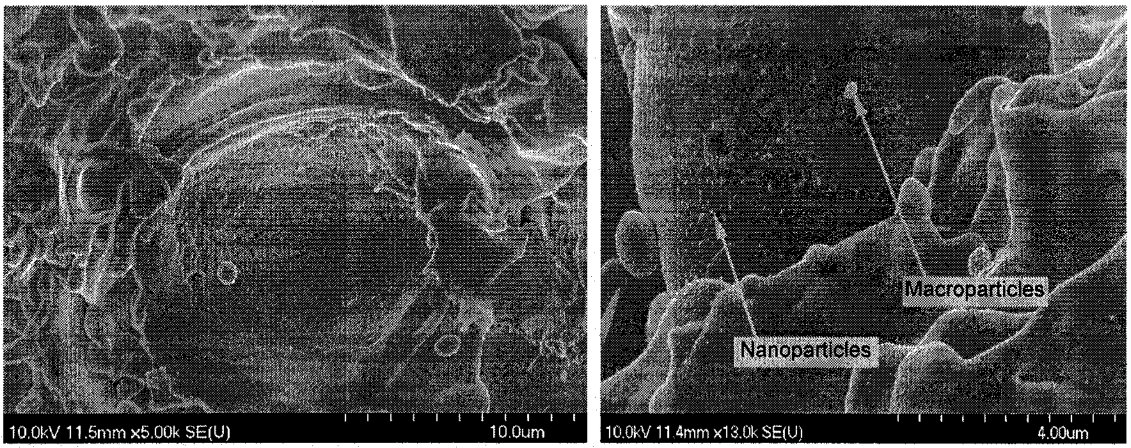

(A) (B)

Figure 4-2. (A) FE-SEM image of a crater formed by a cathode spot. (B) Enlarged view of a crater.

A numerical integration of individual current pulses (Figure 3-4 (B)) over the arcing time gives rise to an average of 0.06 C transferred per pulse. Since the reported erosion rate of a copper cathode in vacuum arcs ranges from 40 to 140 μg C^{-1}, the mass loss per pulse is estimated to be of the order of 2.4 to 8.4 μg. For a typical arcing frequency of 20 Hz, the mass loss rate falls in the range of 48 to 168 μg s^{-1}. If it is assumed that all the eroded material is used to produce fully-dense copper nanoparticles with a mean diameter of 30 nm, a nanoparticle production rate of approximately 10^{11} s^{-1} is obtained. Obviously, such high production rate is not reached since a significant fraction of the erosion rate is associated with the production of macroparticles, which are in the form of emitted droplets from the cathode spots. Additionally, some metal vapors might be swept away by the inert gas flow without condensation as metal nanoparticles.

Both the amount of evaporated cathode materials and the individual fractions of nanoparticles and macroparticles depend on many parameters such as the peak arc current and arcing frequency [58]. Based on weighing the cathode rods before and after arc evaporation for 8 hours with the pressure of 10 torr, erosion rates of 54 μg s^{-1} and 88

$\mu g\ s^{-1}$ were estimated for peak arc currents of 30 A and 60 A, respectively. For the actual arcing frequency of 22 Hz, the calculated erosion rates were approximately 38 and 32 $\mu g\ C^{-1}$, respectively. Generally, a higher arc current leads to a more intensive energy input into the cathode spot and consequently, to a higher erosion rate. However, the erosion rate for the lower pulsed arc current (30 A) was found to be slightly more significant than the higher pulsed arc current (60 A). This result may be associated with the re-deposition on the cathode surface of macroparticles emitted from the cathode spots since a larger amount of bigger metal particles were observed on the cathode surface at higher pulsed arc current (60 A). This phenomenon may also be partially caused by the condensation of some metal vapors from the higher density metallic plasma generated at higher arc currents [51].

Macroparticles are ejected away from the cathode spots mainly in the cathode plane [58]. With the copper cathode located at the axis of a coaxial electrodes assembly, most macroparticles deposited on the inside surface of the anode tube, while a small fraction re-deposited on the cathode surface. Small amounts were collected on the collection copper sheet, TEM grids and collection polymer filters. When the inter-electrode gap is smaller than the steady-state radius of the expanding metallic plasma (section 4.4.3.), only the nanoparticles formed within the expanding metallic plasma and having a direction parallel (or small angle) to the upward axial direction can be brought away from the arc evaporation zone, while the remaining flux is captured by the surrounding anode tube.

Samples of the deposit left on the inside surface of the anode tube was observed with FE-SEM, as shown in Figure 4-3. A considerable amount of copper nanoparticles with size ranging from 10 to 20 nm and a large copper macroparticle of approximately 200 nm are displayed. Some copper nanoparticles attached on the surface of the macroparticle, while most nanoparticles heavily agglomerated together on the anode surface. The macroparticles are produced by the emission of liquid metal droplets from the cathode spot. The nanoparticles are formed by the homogenous nucleation of metal vapors within the metallic plasma and possibly, by plasma vapor deposition of metal ions/atoms on the surface of the anode tube (Figure 4-3 (A)). Since the plasma/vapor plume is limited within the narrow inter-electrode zone, a significant fraction of the formed copper nanoparticles deposit on the inside surface of the anode instead of diffusing out of the metallic plasma, thus leading to the heavy agglomeration of copper nanoparticles on the anode surface. The accumulation of individual copper nanoparticles also confirms that such nanoparticles are formed within the expanding metallic plasma before they deposit onto the anode surface.

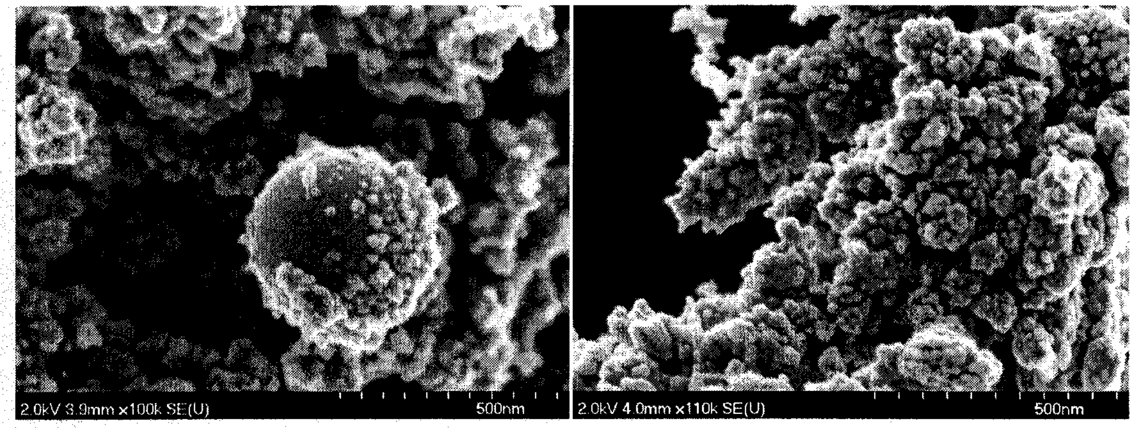

(A) (B)

Figure 4-3. FE-SEM images of copper macroparticles (A) and nanoparticles (B) deposited on the inside surface of the anode steel tube.

4.4.2. Net production rate of diffused metal vapors/nanoparticles

Since both copper macroparticles and some copper nanoparticles deposit on the inside surface of the anode tube, it is impossible to separate the condensed nanoparticles from the splashed macroparticles in the deposit and to obtain the net production rate of metal vapors from the cathode spot. However, the net production rate of diffused metal vapors/nanoparticles from the metallic plasma can be inferred by deducting the deposition rate of particles on the anode tube from the total erosion rate of the cathode materials.

The deposit left on the anode tube was collected and weighed. An approximate macroparticle production rate of 15 $\mu g\ s^{-1}$ (or 10.6 $\mu g\ C^{-1}$) is calculated for peak arc current of 30 A in 10 torr argon. Since the total erosion rate is 54 $\mu g\ s^{-1}$ (or 38 $\mu g\ C^{-1}$), the production rate of the diffused metal vapors/nanoparticles is calculated to be 39 $\mu g\ s^{-1}$ (or 27.4 $\mu g\ C^{-1}$). We can estimate that the net erosion rate of metal vapors is between 27.4 $\mu g\ C^{-1}$ (the measured production rate of metal vapors) and 38 $\mu g\ C^{-1}$ (the total erosion rate of the cathode materials) for peak arc current of 30 A in 10 torr argon. Following the same way, the macroparticle production rate of 43 $\mu g\ s^{-1}$ (or 15.6 $\mu g\ C^{-1}$) and the production rates of the diffused metal vapors/nanoparticles of 45 $\mu g\ s^{-1}$ (or 16.4 $\mu g\ C^{-1}$) are obtained for peak arc current of 60 A in 10 torr argon.

The increase of macroparticle production with the increase of peak arc current indicates that, although the operation at higher peak arc current enhances the cathode erosion rate and thus, the nanoparticle production rate, it leads to an increase of the macroparticles yield (e.g. from 15 $\mu g\ s^{-1}$ to 43 $\mu g\ s^{-1}$ with peak arc current from 30 A to 60 A). Furthermore, it is very probable that the increased production of macroparticles contributes, in most part, to the increased erosion rate observed at higher current levels, while the production of nanoparticles is only slightly increased (from 39 $\mu g\ s^{-1}$ at 30 A to 45 $\mu g\ s^{-1}$ at 60 A). This result is also consistent with model predictions that demonstrated an increase in the rate of liquid volume formation under the cathode spot with the arc current [112]. Arcing current levels of 10 to 40 A lead to a good compromise between the production rate of metal nanoparticles and the macroparticle yield. Finally, since more nanoparticles are produced at higher arcing frequencies, this frequency was kept near the maximum reachable value for all experiments (22 Hz, in practice).

4.4.3. Estimation of the metal vapor density

According to Meunier [52], the radius of the expanding metallic plasma can be estimated by the equation:

$$\frac{dR(t)}{dt} = \sqrt{3}\left(\frac{M_p(t)V_0^2 - \left(\frac{4\pi}{3}\right)pR(t)^3}{M_p(t) + 2\pi\rho_g R(t)^3} \right)^{1/2} \tag{4-3}$$

with $M_p(t) = \int_0^t E_r I(t)dt$. E_r is the vacuum erosion rate of copper, 80 μg C^{-1} [51], V_0 is the vacuum expansion velocity of the metallic plasma, 10^4 m s^{-1}. With a reactor pressure of 1333 Pa (10 torr) and a peak arc current of 30 A, integrating the expansion velocity (*dR/dt*) to the sound velocity C of argon (323 m s^{-1}) allows to obtain τ_c, the plasma expansion time (5 μs) and the steady-state radius of the expanding metallic plasma (4.8 mm). Since the estimated net erosion rate of metal vapors lies between 27.4 and 38 μg C^{-1} for a peak arc current of 30 A in 10 torr argon, the density of metal vapor within the metallic plasma is estimated to be approximately 10^{19} m^{-3}.

4.5. Characterization of metal nanoparticles

The collected metal nanoparticles were characterized by transmission electron microscopy (TEM) and field emission scanning electron microscopy (FE-SEM). Metal nanoparticles were directly deposited onto the TEM grids for TEM analysis, while the collection polymer filter with the deposited metal nanoparticles needed to be coated with a thin gold layer to make its surface electrically conductive for FE-SEM analysis. The gold layer was approximately 4 nm in thickness, and evenly spread over the surface of the polymer filter and metal particles. The TEM images were obtained with a JEOL JEM-2011 transmission electron microscope, operated at 200 kV and equipped with a CCD imaging system. The SEM images were obtained with a Hitachi S-4700 scanning electron microscope.

Figure 4-4 shows FE-SEM and TEM images of copper nanoparticles produced under the following conditions: argon flow rate of 200 sccm, reactor pressure of 2.5 Torr, arc pulse frequency of 20 Hz, and peak arc current of 30 A. The nanoparticle diameter ranges from several to approximately 50 nm. It was found that the size of the copper nanoparticles collected at the downstream end of the reactor (Figure 4-4 (A), (B) & (C)) shows little difference with the size of the nanoparticles that deposited on the inside surface of the anode tube (Figure 4-3), thus indicating that most copper nanoparticles are formed within the metallic plasma, and that their size does not further change when carried away from the arc evaporation zone by the inert carrier gas.

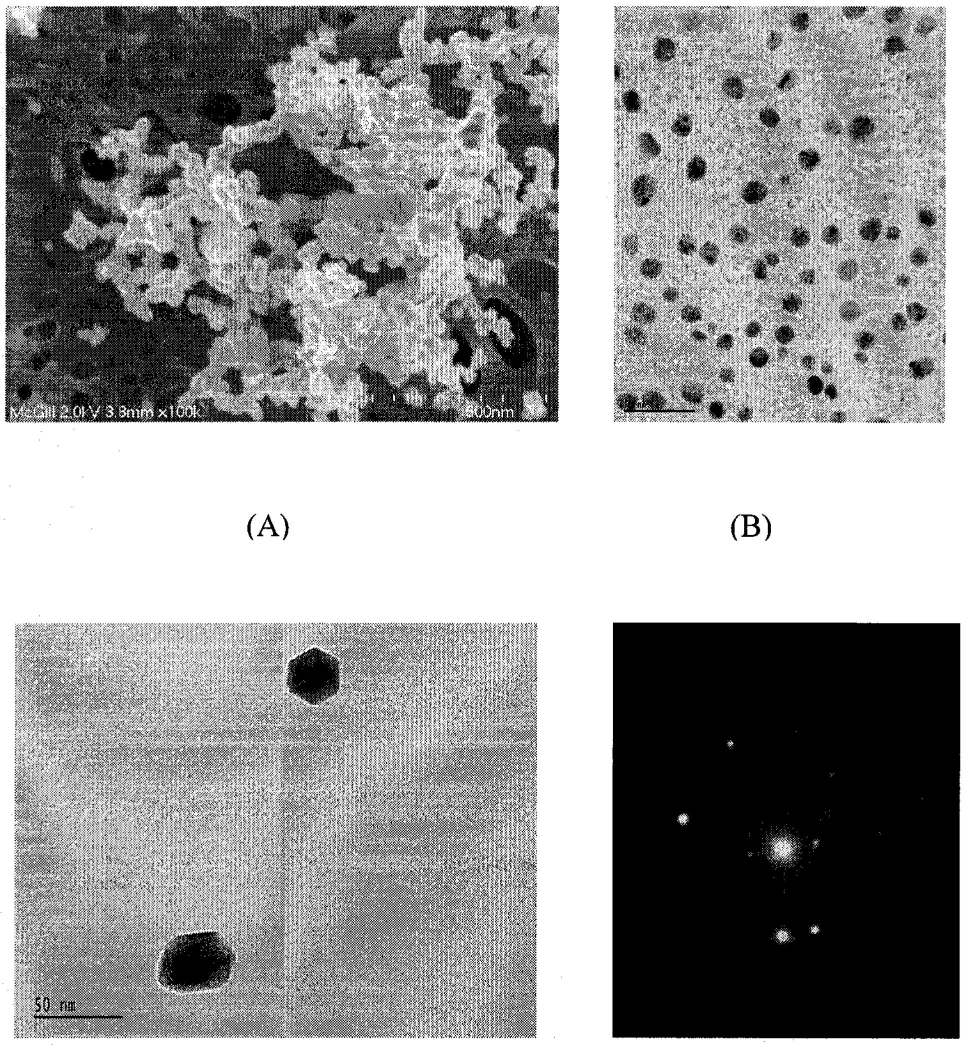

(A) (B)

(C) (D)

Figure 4-4. FE-SEM (A) and TEM (B & C) images of uncoated copper nanoparticles obtained with an argon flow rate of 200 sccm, reactor pressure of 2.5 Torr, arc pulse frequency of 20 Hz, and peak arc current of 30 A. (D) Electron diffraction pattern of a single copper nanoparticle (about 20 nm in diameter).

As a consequence of their high surface free energy, most of the copper nanoparticles agglomerated, as can be clearly seen with Figure 4-4 (A), though several individual nanoparticles are also observed. The TEM images (Figure 4-4 (B) & (C)) show that a large fraction of the copper nanoparticles have a spherical shape, while some nanoparticles have an irregular shape, suggesting a crystalline structure. In fact, the electron diffraction pattern obtained by directing the TEM electron beam perpendicular to a small agglomerate of copper nanoparticles shows a pattern of diffraction spots (Fig. 4-4 (D)), thus revealing the crystalline structure of this nanoparticle. For a crystalline nanoparticle, different crystal facets possess different surface energies. When the surfaces of the crystalline nanoparticle are combined in a certain pattern, a minimal surface energy can be obtained. Therefore, crystalline nanoparticles tend to form facets, thus leading to irregular shapes. However, the difference in surface energy of various crystal facets can be negligible if the thermal motion predominates because of high temperatures. Therefore, the produced crystalline nanoparticles do not form facets and are spherical in shape [114]. Such a crystalline structure is caused by the homogeneous nucleation process taking place inside the high-density metal vapor clouds produced by cathodic arc spots. It was reported that the homogeneous nucleation from metal vapors may lead to the formation of initial nano-sized clusters having a mono-crystalline structure [10].

It is noteworthy that no large agglomerates of metal nanoparticles were collected on the TEM grid (Figure 4-4 (B) & (C)). In fact, the copper nanoparticles individually scattered onto the TEM grid. A floating potential collecting surface like a nanoparticle accumulates a negative surface charge to balance the electric currents of the very mobile electrons and less mobile ions when exposed to a plasma [115]. This surface charge may hinder the agglomeration process due to the repulsive electrostatic interactions that develop between charged nanoparticles. The fact that no large agglomerates were observed on the TEM grids might be an indication that the nanoparticles retained their negative surface charges up to the collection point located several cm downstream the plasma region. However, a severe agglomeration of metal nanoparticles can be observed in the SEM image (Figure 4-4 (A)). This agglomeration is caused by the overlap of numerous metal nanoparticles. The ultrafine polymer filter used to collect the metal nanoparticles fully blocks the aerosol flow of nanoparticles in argon (Section 3.6). A considerable amount of nanoparticles produced during the experiment deposit onto the polymer filter, so that many nanoparticles accumulate on the surface of the polymer filter forming several layers.

4.6. Effect of reactor pressure

In the arc evaporation/condensation reactor, metal vapor condensation and cluster formation occur as a result of the confinement of the fast expanding metallic plasma by the low-pressure background gas and the formation of shock wave front. The size of the produced nanoparticles strongly depends on the chemical composition and pressure of the background gas. The effect of the inert gas pressure on the size of the formed nanoparticles was investigated. The reactor pressure was varied in the 10-500 torr range keeping the Ar flow rate constant.

Since a large amount of copper nanoparticles deposited on the collection polymer filter, it was possible to estimate their mean size and obtain their size distribution based on a visual survey of the FE-SEM images. FE-SEM images of copper nanoparticles as well as corresponding size histograms of the nanoparticles produced under different pressures with the same argon flow rate are shown in Figure 4-5. Experiments were carried out with an argon flow rate of 400 sccm and reactor pressures of 10 (A), 60 (B), 120 (C) and 500 torr (D), respectively.

(A)

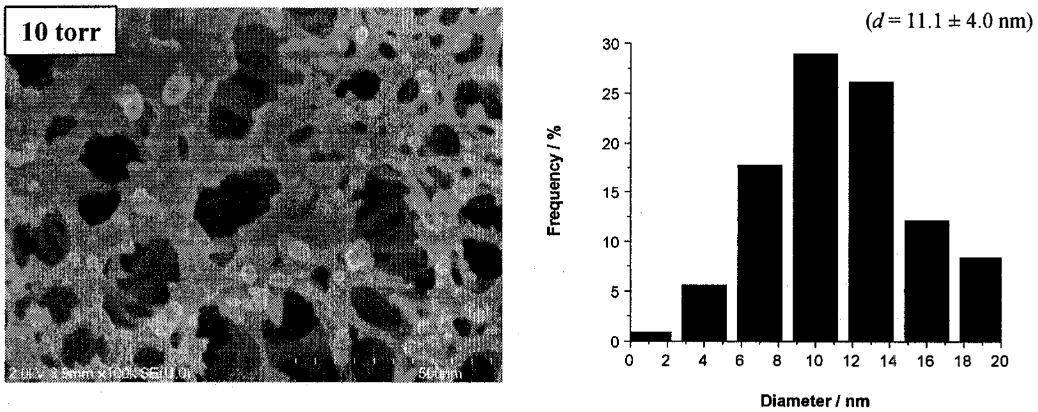

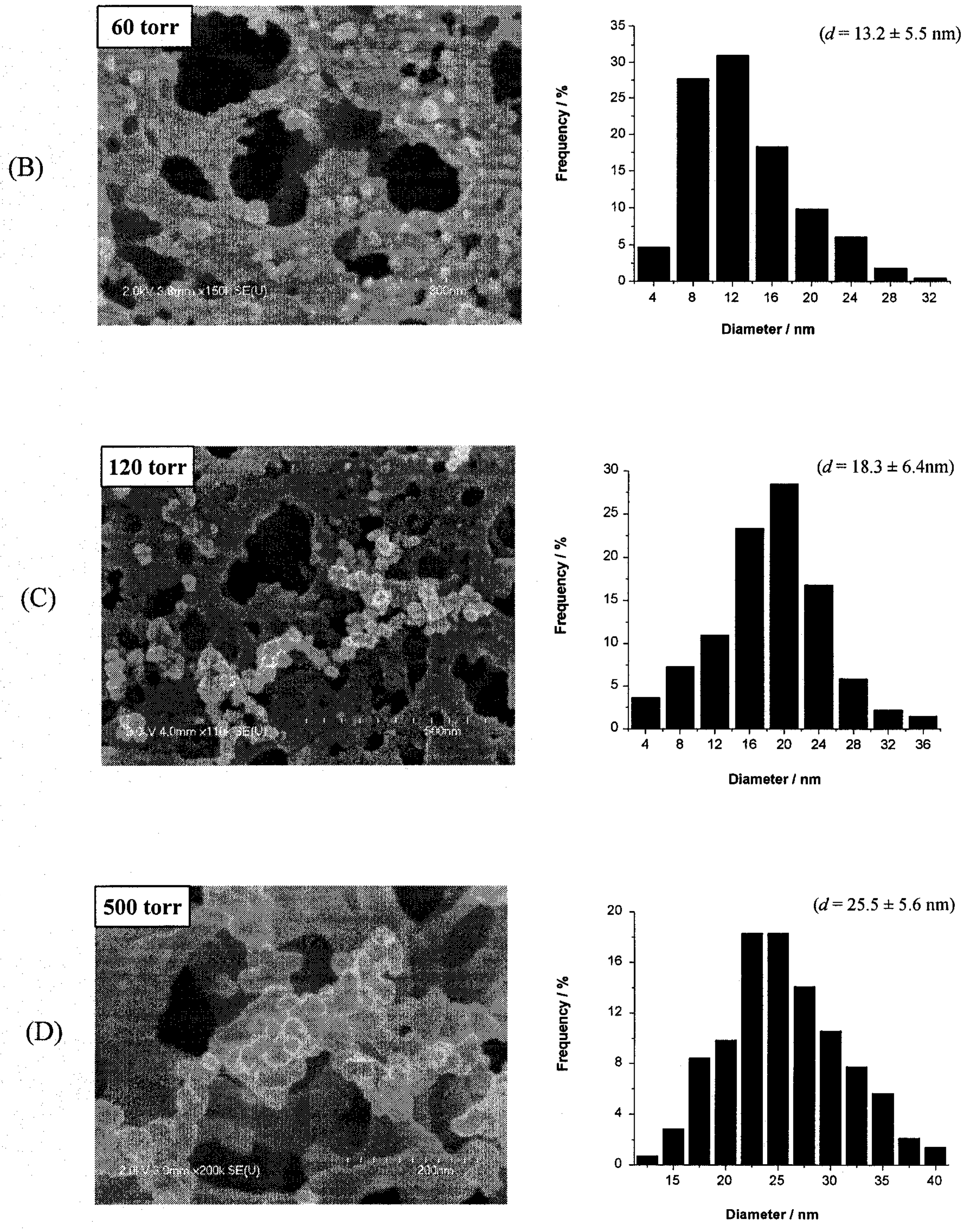

Figure 4-5. FE-SEM images and corresponding size histograms for copper nanoparticles produced under different reactor pressures with peak arc current of 30 A and an argon flow rate of 400 sccm. (A) 10 torr, (B) 60 torr, (C) 120 torr, and (D) 500 torr.

As can be seen, most of the produced copper nanoparticles have a spherical shape, while some nanoparticles have an irregular shape. At the lower reactor pressures of 10 and 60 torr, small agglomerates of several nanoparticles were produced (Figure 4-5 (A) & (B)). At higher reactor pressures (120 and 500 torr), large agglomerates containing tens of copper nanoparticles were produced (Figure 4-5 (C) & (D)).

The average particle sizes and size distributions of these copper nanoparticles were obtained based on the visual observation of at least 250 randomly selected nanoparticles. Since the polymer filters as well as all the copper nanoparticles deposited on their surface are coated with an approximately 4 nm-thick gold layer, the actual size of the individual copper nanoparticles was obtained by subtracting the thickness of the gold layer from the measured values. Since the thickness of the gold layer deposited onto the nanoparticle surface is not uniform, the obtained values of the copper nanoparticle size carry certain measurement error (approximately 15% as I discussed with the SEM experts). The average diameter of the individual copper nanoparticles produced at 10 torr was 11.1 nm, while this average size increased to 13.2 nm, 18.3 and 25.5 for reactor pressures of 60, 120 and 500 torr, respectively. The average particle size and standard deviation of the size distribution are plotted in Figure 4-6.

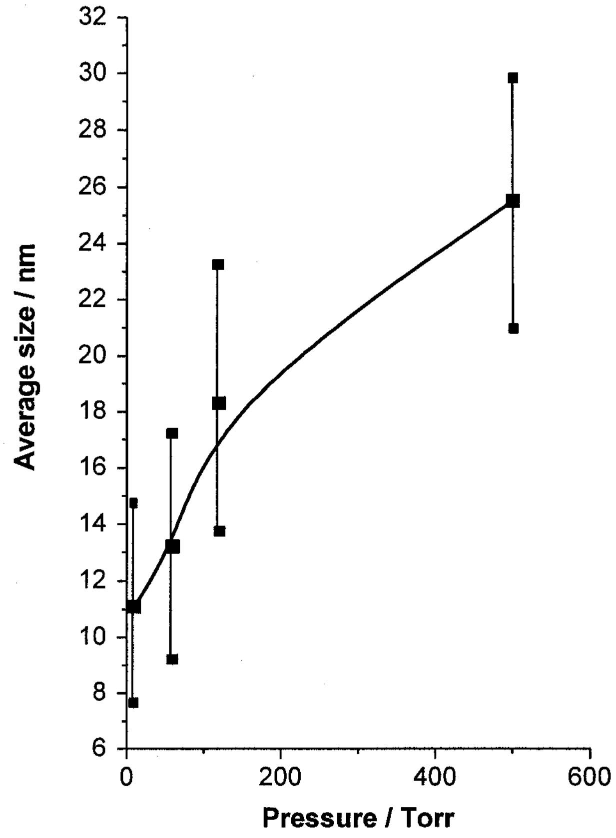

Figure 4-6. Plot of average particle size and standard deviation of the size distribution versus reactor pressure.

The increase of the average diameter of copper nanoparticles with reactor pressure is thought to be caused by the fact that the background gas limits the expansion of the metallic vapor/plasma cloud formed at the cathode spots and that a shock wave front is formed between the metallic plasma and background gas [45, 50-52]. Because of the high plasma density and high pressure within the metallic plasma [44, 116], it is assumed that the mechanism responsible for the cathodic arc evaporation is not affected by the background gas with pressure up to atmospheric and that the initial cathodic arc plasma can be assumed to operate at the vacuum evaporation rate [51]. The estimated values for the metallic plasma expansion time τ_c, steady-state radius of the expanding metallic plasma R_c and the density of generated metal vapor ρ_{Cu} for an argon flow rate of 400 sccm and a peak arc current of 30 A are reported in Table 4-2 for a range of operating pressures.

Table 4-2. Metallic plasma expansion time τ_c, steady-state radius of the expanding metallic plasma R_c and density of metal vapors ρ_{Cu} at different ambient gas (Ar) pressures.

Pressure / Torr	10	60	120	500
τ_c / μs	5.0	2.0	1.4	0.7
R_c / mm	4.81	1.96	1.38	0.68
ρ_{Cu} / m^{-3} ($\times 10^{19}$)	0.9	5.4	10.7	45.0

The highest ambient gas pressure leads to the smallest volume for the expanding metallic plasma as well as to the highest density of metal vapors within the plasma. It is suspected that with a cooling rate of 3×10^9 K s^{-1}, the condensation and nucleation of the metal vapors happen so quickly that the metal nanoparticles are formed within the boundary zone. The higher concentration of metal vapors gives rise to a more significant supersaturation of the metal vapor cloud, and higher rates of collisions amongst metal atoms and formed nanoparticles. Both processes enhance homogeneous nucleation and particle growth. The larger agglomerates seen with the high reactor pressure are also an outcome of this increased collision rate.

4.7. Effect of inert gas flow rate

The inert gas flow has three main functions: the cooling of the diffused metal vapors/nanoparticles, the transport of the formed metal nanoparticles, and the dilution of the aerosol of metal nanoparticles. Although this inert gas flow does not influence the homogeneous nucleation process of metal vapors, which happens within the expanding metallic plasma, it can cool the metal vapors diffusing out of the metallic plasma, thereby leading to the formation of metal clusters and small nanoparticles. Furthermore, the inert gas dilutes the generated metal nanoparticle mixture, thus avoiding the formation of big agglomeration of metal nanoparticles. The inert gas flow rate was varied between 200 and 2000 sccm with the reactor pressure in the 10-500 torr range. Its effect on the dimension of generated copper nanoparticles was investigated.

Figure 4-7 presents FE-SEM images of copper nanoparticles produced with argon flow rates of 600 (A), 1000 (B) and 2000 sccm (C), at a reactor pressure of 60 torr, as well as the corresponding size histograms. The average nanoparticle sizes are 12.8 nm, 11.2 nm and 9.2 nm, respectively. An average particle size of 13.2 nm was obtained at 400 sccm (Figure 4-5 (B)).

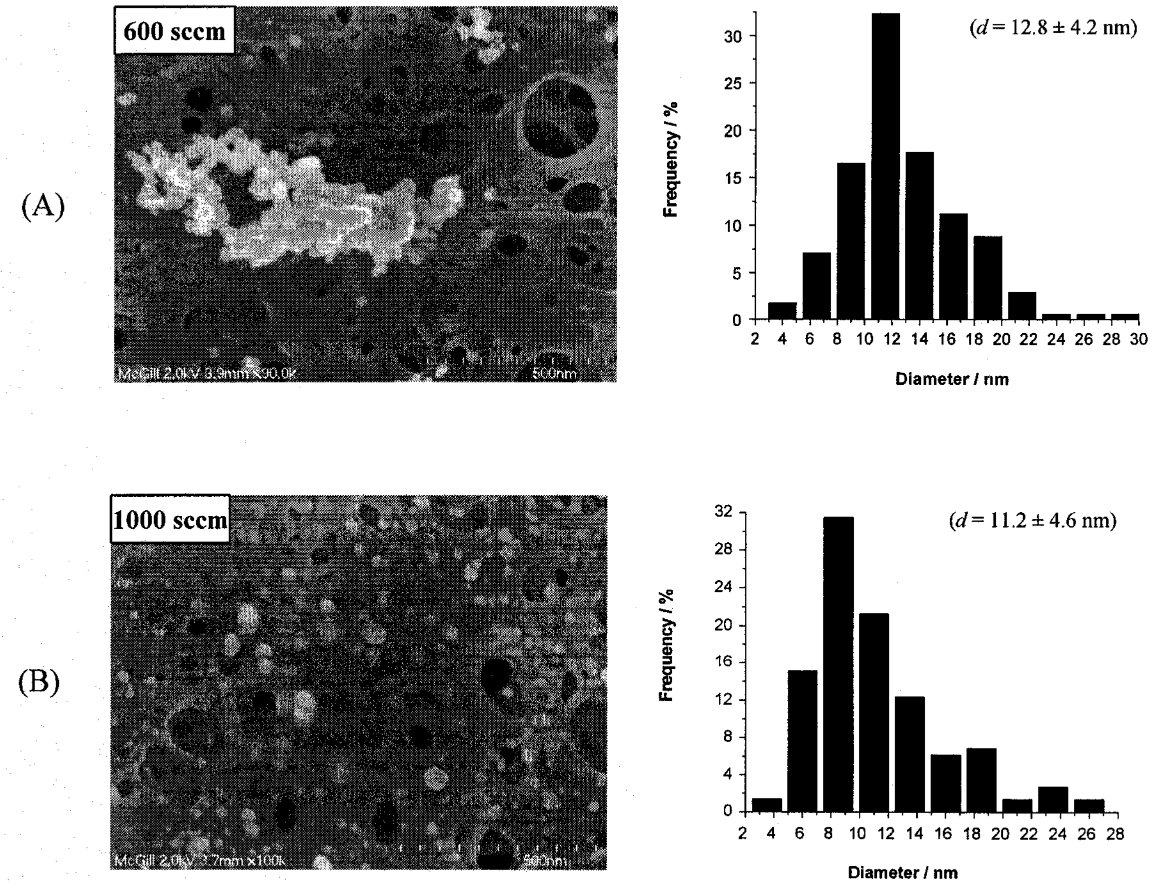

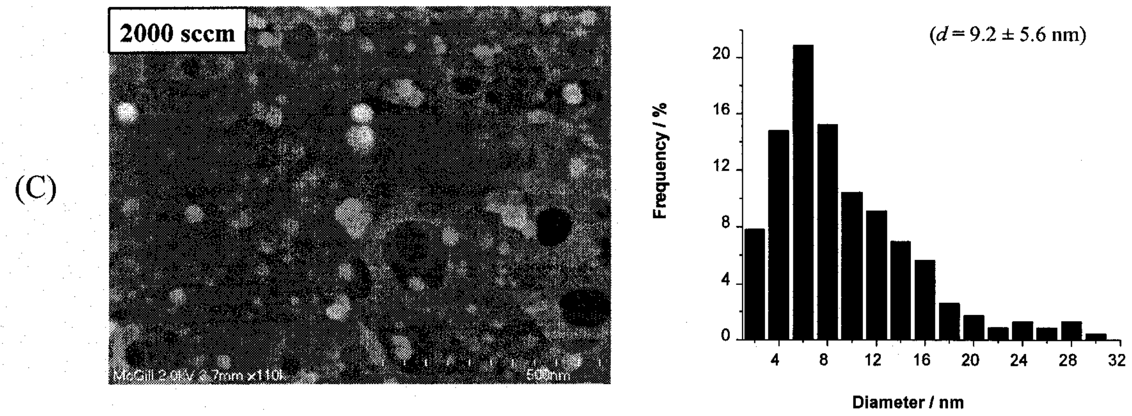

Figure 4-7. FE-SEM images and corresponding size histograms of copper nanoparticles produced with different argon flow rates under a reactor pressure of 60 torr. (A) 600 sccm, (B) 1000 sccm, (C) 2000 sccm. Results for an argon flow rate of 400 sccm were presented in Figure 4-5 (B).

The plot of the average nanoparticle size and standard deviation of the size distribution versus the argon flow rate is shown in Figure 4-8. Although the average size of the copper nanoparticles slightly decreases as the argon flow rate increases, the obtained values at different argon flow rates are essentially the same considering the measurement error. The size of most metal nanoparticles falls in the 8-16 nm range over the 400-2000 sccm Ar flow rate. This result also confirms that the copper nanoparticles are formed within the metallic plasma and that the inert gas flow rate has little effect on the size of the formed copper nanoparticles.

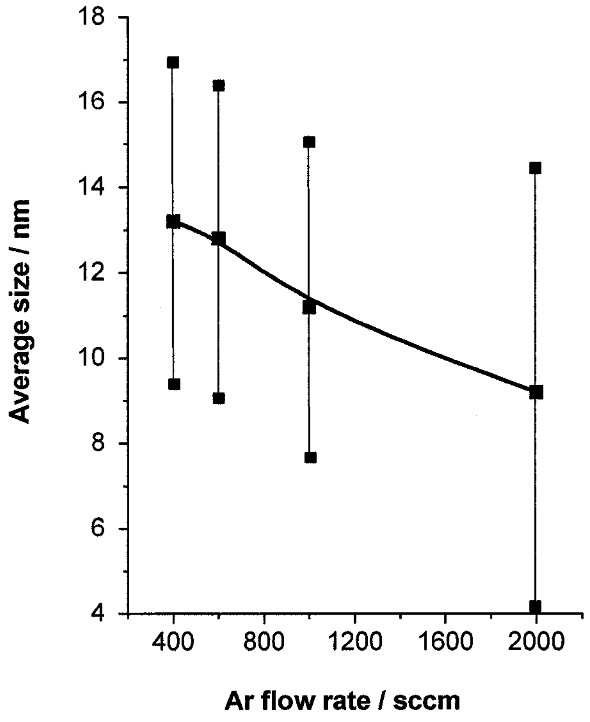

Figure 4-8. Plot of the average nanoparticle size and standard deviation of the size distribution versus the argon flow rate.

At a reactor pressure of 60 torr and an argon flow rate ranging from 400 to 2000 sccm, the mean velocity of the argon flow through the inter-electrode gap ranges from 3.7 to 18.3 m s^{-1}. Such velocities are much smaller than the velocity of the metallic arc plasma expansion (10^2 to 10^4 m s^{-1}). Consequently, the characteristic time of the metallic plasma expansion (0.1 to 10 ms) is much smaller than the residence time of argon in the inter-electrode gap (~100 ms). With the high cooling rate of 3×10^9 K s^{-1} within the plasma/gas boundary zone, the nucleation of metal vapors and nanoparticle formation within the boundary zone occur so rapidly that the inert gas flow has no significant effect.

However, it is possible that some metal vapors diffuse from the metallic plasma, cooled and transported away by the argon flow, thus forming small nanoparticles. The higher the argon flow rate, the more and smaller nanoparticles are generated outside the cathodic arc plasma. This could explain why the size distribution of the produced metal nanoparticles spreads out as the argon flow rate increases.

4.8. Summary

The experimental results revealed that the homemade pulsed DC power supply is capable of producing a steady train of pulsed arcs which, through the formation of cathode spots, lead to the formation of dense metal vapor clouds which, in turn, lead to the production of metal nanoparticles. The size of the copper nanoparticles ranges from several nanometers to 50 nm, while most of the nanoparticles are in the 10-30 nm size range. Some of the formed copper nanoparticles have a crystalline structure.

It has been demonstrated that low reactor pressures (below 20 torr) lead to the production of small nanoparticles (~10 nm) and that the argon flow rate has little influence on the average size of the produced metal nanoparticles. On the other hand, a higher argon flow rate leads to a wider size distribution. It was also shown that the macroparticles yield increases with the arc peak current, in agreement with previous model predictions.

Chapter 5

Synthesis of plasma polymer-coated metal nanoparticles

5.1 Introduction

The metal nanoparticles produced in the cathodic arc evaporation/condensation region are transported into a Pyrex chamber where they are coated in-flight with an organic film by plasma polymerization. In practice, the combination of the arc evaporation reactor with the plasma polymerization reactor requires compromises to be made with the operating conditions in order to accommodate the requirements of both processes, and to obtain the desired product. Mainly, the reactor pressure and inert gas flow rate need to be adjusted to obtain coated metal nanoparticles.

The experimental procedure for obtaining coated metal nanoparticles is presented first. Next, the operating conditions of the plasma polymerization are optimized. The morphology of the coated copper nanoparticles is characterized, and the chemical structures of the plasma polymer coating and of the interface between the organic coating and the metal nanoparticle are analyzed. Finally, the mechanism of plasma polymerization from ethane is discussed on the basis of the experimental results and models taken from the literature.

5.2. Experimental considerations

5.2.1. Experimental procedure

The reactor was evacuated for 30 minutes, and then argon and ethane were introduced. The reactor pressure was adjusted to the required value. In order to ensure that all produced metal nanoparticles are coated, the CCRF plasma was ignited before the pulsed arcs and also, switched off after. After the experiments, the ethane flow was shut off while argon was allowed to flow for an additional 10-15 minutes in order to cool down the reactor.

5.2.2. Experimental conditions

Preliminary experiments showed that a stable, uniform and large volume CCRF plasma in a mixture of argon and ethane could not be sustained at high pressures above 30 torr with the present reactor configuration. In fact, we found that reactor pressures under 20 torr ensured both stability and uniformity of the plasma volume for RF power levels under 100 W and argon flow rates in the 200-800 sccm range. Under such conditions, extensive plasma polymerization onto the metal nanoparticles' surface occurred even at high ethane dilution (e.g. 0.25% v/v). In practice, an ethane flow rate of 2 sccm was used in all experiments, since this flow rate proved to be enough to ensure a full coating of the produced copper nanoparticles. The arcing current and arcing frequency were kept at the values used in Chapter 4: arc current ranging from 10 to 40 A and an arcing frequency of 22 Hz. All experiments were carried out for 30 to 60 min. The main experimental conditions are displayed in Table 5-1.

Table 5-1. Summary of the experimental conditions

Duration	30-60 min
Reactor pressure	2.5-20 torr
Argon flow rate	200-800 sccm
Ethane flow rate	2 sccm
Arc pulse frequency	~22 Hz
Arc peak current	10-40 A
RF power	40-100 W

5.3. Characterization of coated metal nanoparticles

5.3.1. Product of plasma polymerization from ethane

TEM images (Figure 5-1) of the coated copper nanoparticles show that two kinds of plasma polymer films were generated in the plasma polymerization reactor: one is a smooth, uniform and dense film onto the copper nanoparticle's surface (Figure 5-1 (A) & (B)); another is an oily film (Figure 5-1 (C)).

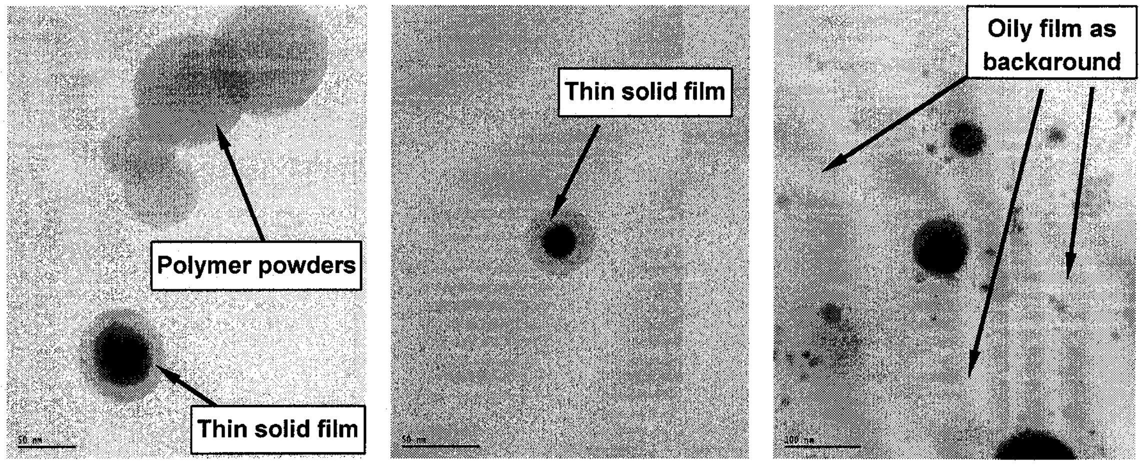

(A) (B) (C)

Figure 5-1. TEM images of plasma polymer-coated Cu nanoparticles. (A) & (B) solid-film coated Cu nanoparticles produced with a pulsing frequency of 22 Hz, Ar flow rate of 400 sccm, C_2H_6 flow rate of 2 sccm, pressure of 10 torr and RF power of 60 W; (C) oily films with Cu nanoparticles produced with a pulsing frequency of 22 Hz, Ar flow rate of 400 sccm, C_2H_6 flow rate of 2 sccm, pressure of 15 torr and RF power of 100 W.

In the first case, the solid film appears as a translucent thin shell surrounding the copper nanoparticles. Such solid coatings were formed by the plasma polymerization from the ethane monomer onto the copper nanoparticles' surface, which is confirmed with other characterization means such as FT-IR and XPS. The characteristic thickness of the organic layer ranges from 3 to 10 nm. The spread in thickness is due to the range of residence times of the copper nanoparticles in the plasma polymerization chamber (e.g.

residence times ranging from 6 to 1.5 s with a reactor pressure of 5 torr and an argon flow rate in the 200-800 sccm range).

In the latter case, no dense solid coating is observed, and the oily deposits onto the copper nanoparticles appear like sticky liquid droplets. When collected with TEM grids, the oily deposits spread on the grids, forming blurred backgrounds on the TEM images.

Unfortunately, a co-product was formed in the first case. Polymer powders (Figure 5-1 (A)) with a mean diameter of about 100 nm were formed inside the plasma polymerization reactor. They have spherical shape and agglomerate together. Géraud et al. [93] also reported that white spherical particulates with diameters in the 200-800 nm range are generated in the CCRF methane plasma. Kobayashi et al. [90] proved that the chemical structure of the organic powders and the coatings on the metal nanoparticles' surface are not significantly different, while the oily films are composed of highly branched oligomers. Stoykov et al. [117] have studied the synthesis of nanosized organic particles in a C_2H_2 RF discharge and indicated that the reactor pressure and plasma power both have dramatic effects on the clustering process. In the present reactor, small amounts of polymer powders mixed with coated copper nanoparticles were consistently found. Unfortunately, we could not identify the relationship between the quantity of polymer powders produced and the operating conditions.

It is also seen from the FE-SEM image (Figure 5-2) of coated copper nanoparticles that they tend to deposit onto the polymer filter surface as individual entities. This observation suggests that the thin organic layer deposited onto the metal nanoparticle's surface significantly reduces its surface free energy and thus, hinders the agglomeration process leading to the formation of large micrometer-sized particles.

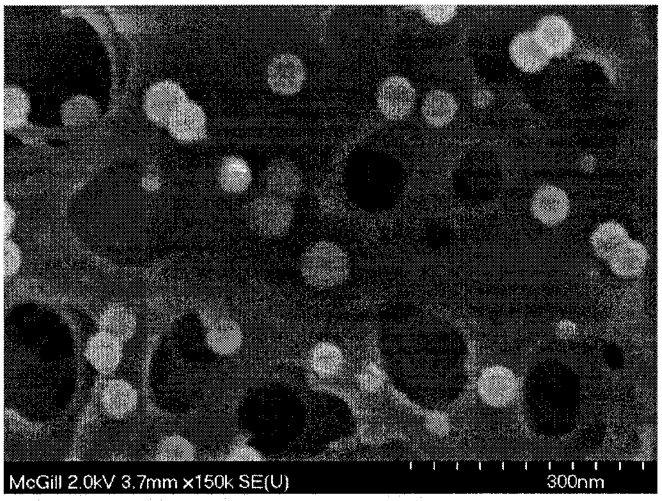

Figure 5-2. FE-SEM images of coated copper nanoparticles produced with a pulsing frequency of 22 Hz, Ar flow rate of 400 sccm, C_2H_6 flow rate of 2 sccm, pressure of 10 torr and RF power of 60 W.

5.3.2. Hydrophobicity of the plasma polymer coating

The coated copper nanoparticles were dispersed in various polar solvents (water, ethylene glycol and acetone) in order to assess their hydrophilicity. A 10-minute-ultrasonic agitation was used to prepare the suspensions. The mixture of water and coated copper nanoparticles could not form a stable suspension. In fact, the nanoparticles floated at the water-air interface even after 10 minutes of ultrasonic agitation. On the other hand, when dispersed in moderately polar (ethylene glycol) and weakly polar (acetone) solvents, the nanoparticles were suspended in the suspension for at least 6 hours. These results confirmed the hydrophobicity of the plasma polymer coating deposited onto the copper nanoparticles. The FT-IR analysis (Section 5.3.4) showed that the coating mainly consists of C-C chains with attached hydrogens, which are non-polar groups [78].

5.3.3. "Characteristic map" for the in-flight plasma polymerization process

The outcome of the plasma polymerization process is quite sensitive to the RF power level, reactor pressure and argon flow rate. It could be a solid nanoscaled film, an oily film, or a mix of the two kinds of films. A series of experiments with different combinations of the operating conditions have been carried out. The RF power was varied in the 40-100 W range, the argon flow rate in the 200-800 sccm range, and the reactor pressure in the range extending from the pump limit to 20 torr. The collected coated copper nanoparticles were observed using the JEOL JEM-2011 TEM microscope to determine the morphology of the produced plasma polymer film. Based on the analysis of the TEM images, a "characteristic map" of the plasma polymerization from ethane generating an organic layer onto the copper nanoparticle was developed (Figure 5-3).

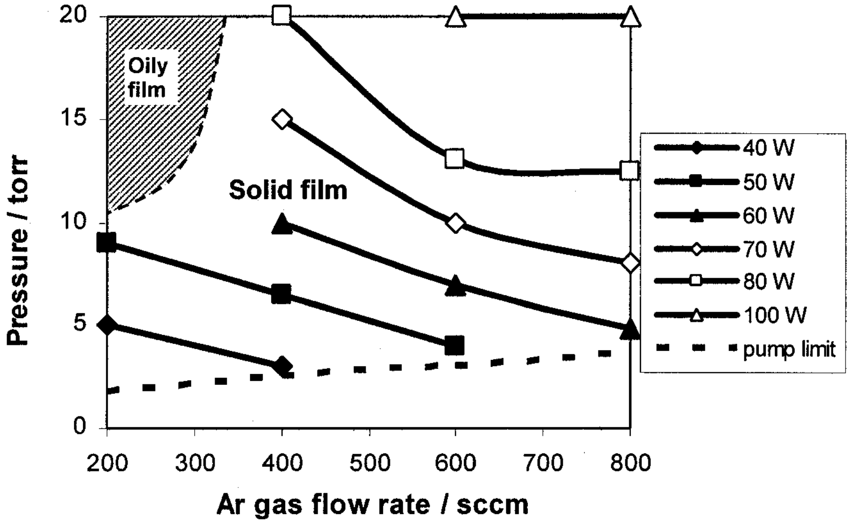

Figure 5-3. Characteristic map for plasma polymerization of ethane onto Cu nanoparticles.

In a nutshell, the map presents regions in the operating parameter space where oily and uniform solid films are formed. Oily films were consistently produced at reactor pressures above 10 torr and argon flow rates under 300 sccm, independently of the RF power level. While in the remaining of the region located above the vacuum pump limit, uniform solid films were formed. In fact, the transition from solid films to oily films is not so abrupt and consequently, the boundary line that separates the two regions must be regarded as approximate. Since the process of plasma polymerization is known to be highly system-dependant [78], critical conditions for the formation of oily films can be defined for the present system: reactor pressures above 10 torr and argon flow rates under 300 sccm. Jensen et al. [91] reported that tacky films and, occasionally, oil droplets were formed by plasma polymerization from the ethane monomer at high reactor pressures and independently of other experimental conditions. Kobayashi [90] observed that the plasma polymer from the ethylene monomer appears in the similar oily film form at high reactor pressures and high ethylene flow rates. Based on the literature and present experimental results, it appears fair to assume that the reactor pressure is the main parameter inducing the generation of oily films from the plasma polymerization of ethane and other simple hydrocarbon monomers.

The effect of RF power levels, reactor pressures and argon flow rates was investigated with more attention in the region where solid films were obtained. The results of such investigation are reported as operating curves at various RF power levels in the "characteristic map" (Figure 5-3). More specifically, operating curves corresponding to each RF power level and correlating the reactor pressure with the argon flow rate are plotted in the map. These operating curves show that at a given value of the RF power, the reactor pressure must be reduced when increasing the argon flow rate in order to produce the solid film on the copper nanoparticle surface. At a given value of the argon flow rate, the RF power must be increased when increasing the reactor pressure. The RF power also needs to be increased with increasing argon flow rate at a given value of reactor pressure.

These operating curves are representative of the combined operating conditions of RF power, reactor pressure and argon flow rate under which uniform solid films form. The calculated energy densities, the energy input per unit mole of gas molecules, are in the 1.0×10^5 to 3.3×10^5 J mol^{-1} range for the operating conditions corresponding to the solid film region. The results presented in the "characteristic map" are further discussed in section 5.4, after the results of the FT-IR and XPS analyses are presented.

5.3.4. FT-IR analysis for coated copper nanoparticles

In order to determine the structure and chemical composition of the organic films deposited onto the surface of the copper nanoparticles, FT-IR spectra of coated copper nanoparticles were taken. The specimens were prepared by depositing uncoated copper nanoparticles and coated copper nanoparticles onto plates made of pressed anhydrous KBr powders placed at the sample collection point-1 (see section 3.6.) for 30 minutes. A Bruker TENSOR 27 FT-IR spectrometer was used to acquire the IR spectrum of the samples. By setting the spectrum of uncoated copper nanoparticles as the background, the IR spectrum obtained with coated copper nanoparticles shows only the features of the deposited organic coating (Figure 5-4).

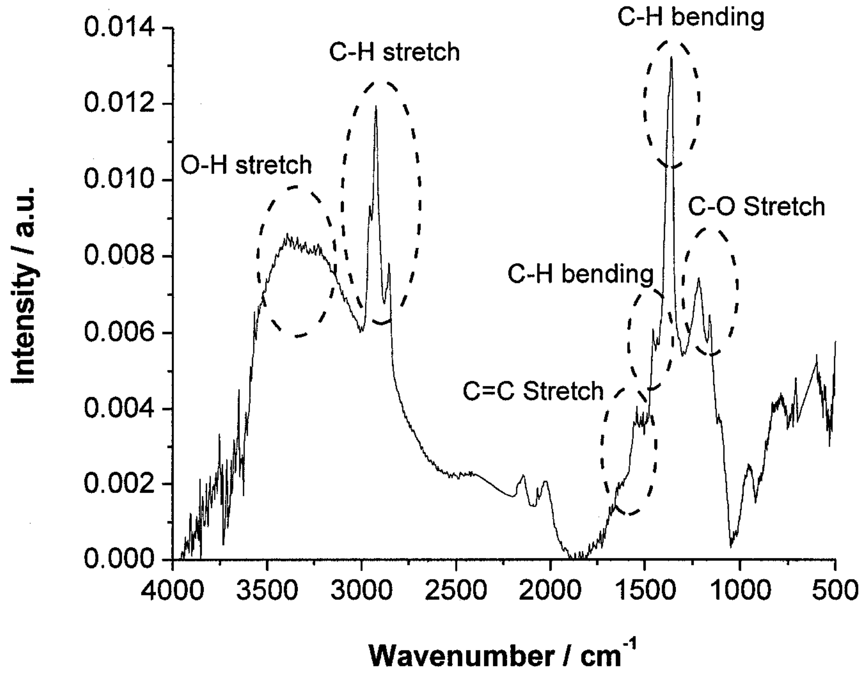

Figure 5-4. FT-IR spectrum of coated copper nanoparticles. The spectrum of uncoated copper nanoparticles has been subtracted.

Because of the existence of plasma polymer powders mixed with coated copper nanoparticles, the obtained IR spectrum contains information from both structures. We assume that the structure of the plasma polymer powder is similar to the one of the plasma polymer film since both were generated under the same plasma polymerization conditions. It must be noted that the coating results from a heterogeneous reaction with the metal particle while the powder forms in a homogenous reaction. On the other hand, it was reported that the chemical structures of the organic powders and coatings on the metal nanoparticles' surface are not significantly different [90]. So, it appears reasonable to assume that the obtained IR spectrum represents the structure of the coating.

The absorption peaks at 3200 cm^{-1} to 3500 cm^{-1} are attributed to the O-H stretch bonds. The peaks at 2953 cm^{-1}, 2924 cm^{-1} and 2855 cm^{-1} are associated to the saturated C-H stretch bonds, the peak at 1454 cm^{-1} to the C-H bending bond, and the peak at 1361 cm^{-1} to the C-H bending bond of the CH_3 group. In addition, a small part of the C-O stretch bonds around 1250 cm^{-1} and C=C stretch bonds around 1650 cm^{-1} are present in the FT-IR spectrum. Due to the presence of C=C bonds in the samples, the IR peaks of unsaturated C-H stretch bonds may also exist in the spectrum, but it is too weak to be observed.

The presence of the O-H stretch bonds in the FT-IR spectrum of the organic hydrocarbon coating is most likely due to the contamination of the KBr powders by some remaining humidity. Owing to the presence of little air in the reactor, a small quantity of oxides is formed in the reactor, which is represented by the C-O stretch bonds in the spectrum of the coating. The most noticeable peaks in the IR spectrum are the saturated C-H stretch and bending bonds, which indicates that the coating has a macromolecular structure with the presence of a small part of C=C bonds [84].

Generally, the result of FT-IR analysis confirms that an organic hydrocarbon coating with a macromolecular structure is formed onto the surface of the copper nanoparticles.

The presence of a great quantity of CH_3 groups in the organic coating reveals that the plasma polymer coating is highly branched.

5.3.5. XPS analysis of the coated copper nanoparticles

X-ray photoelectron spectroscopy (XPS) is a useful tool for the surface analysis of coated metal nanoparticles. It can be used to investigate the elemental composition of the surface layer and their chemical state of the elements. The low kinetic energy (by definition < 1.5 keV) of the emitted photoelectrons makes the XPS technique inherently surface sensitive with the majority of the photoelectrons in a given sample originating from the top 5 nm layer. The detected electron number of one given element is proportional to its concentration in the sample. Most importantly, the exact binding energy of the detected electron is a function of the local environment of the atom, yielding a chemical state-sensitive tool [118]. In practice, the organic layer deposited onto the metal nanoparticle surface of our samples is only a few nanometers thick, so the XPS analysis can be performed to gain insight into the chemical structure of the polymer film as well as on the interfacial bonding between the copper nanoparticle and the polymer film.

The sample for XPS analysis has been prepared by collecting coated copper nanoparticles at the sample collection point-1 using a circular piece of copper sheet (12 mm in diameter) for 12 hours. Then, the deposited coated copper nanoparticles were removed from the copper sheet and stored in a sealed desiccator. The XPS analysis was performed using a Kratos system (Kratos Ultra) with a dual Mg-Al non-monochromatic anode. A depth of approximately 5 nm could be probed with the detector mounted perpendicular to the sample surface. The survey scans covered the 0-1200 eV binding energy range with a resolution of 1 eV and a dwell time of 300 ms. High resolution scans with a resolution of 0.05 eV were used to cover specific regions close to the binding energies of wanted elements. The XPS spectra were analyzed with the help of the Advantage software from Thermo VG Scientific. The spectrum obtained from the survey scan of the coated copper nanoparticles is shown in Figure 5-5, and Table 5-2 displays the concentration of detected elements.

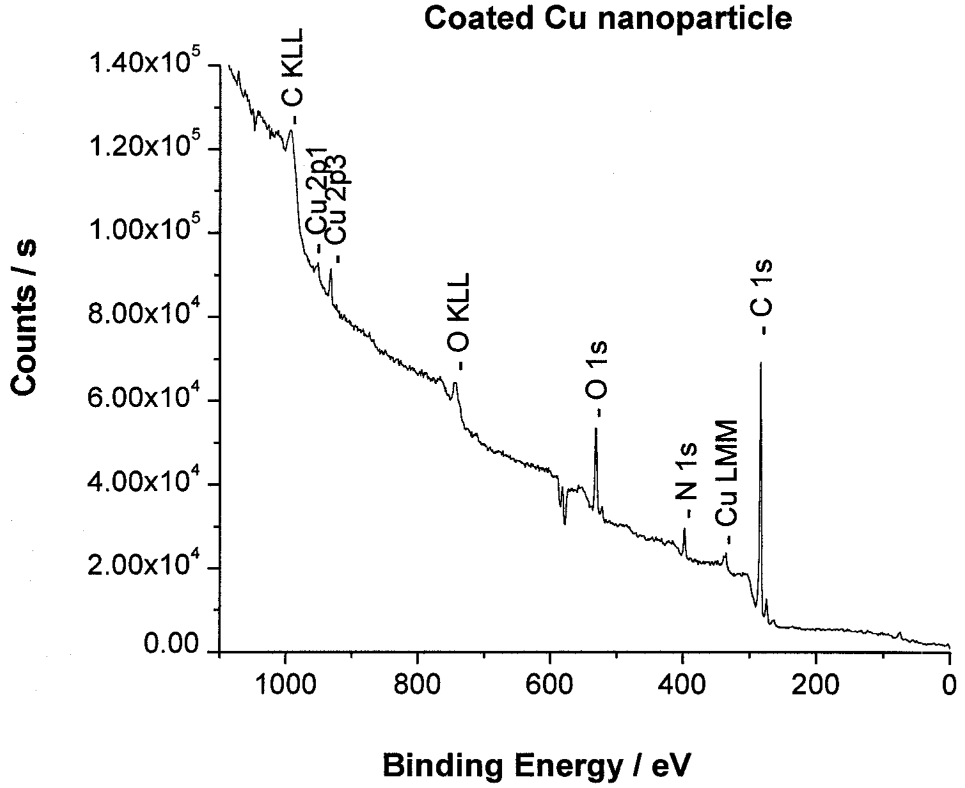

Figure 5-5. The XPS spectrum of coated Cu nanoparticles

From the XPS spectrum, it is found that the main elements present in the top few nanometers of the coated copper nanoparticles sample are Cu, C, O and N, with carbon as the dominant element. This observation confirms the presence of carbon in the coating. The detected Cu elements are from the surface of copper nanoparticles beneath ultrathin (<5 nm) organic coatings. The N and O elements originate from air contamination which is caused either by the residual air present in the reactor or by oxidation when the nanoparticles are removed from the reactor. Certainly, hydrogen should be present in the sample although it can not be detected by XPS.

Table 5-2. Elemental composition of the coating onto the Cu nanoparticles obtained by XPS.

Name	**Binding Energy / eV**	**Height / cps**	**FWHM / eV**	**Peak Area / cps • eV**	**Atom percentage / %**
Cu 2p3	932.0	7246.8	3.43	24138.77	1.8
Cu 2p1	951.0	3423.4	2.35	13538.89	0.0
C KLL	990.0	11336.2	11.34	169857.25	0.0
O KLL	743.0	5921.3	7.17	56188.93	0.0
O 1s	531.0	19834.9	3.69	78566.04	16.6
N 1s	397.0	6804.3	1.91	20935.52	5.9
Cu LMM	335.0	3685.3	2.91	17541.75	0.0
C 1s	283.0	59589.6	2.80	182261.20	75.7
Cu 3p	75.0	1382.4	4.13	6226.66	0.0

The high resolution scans for the Cu, C, O and N elements are shown in Figure 5-6. Since chemical shifts in the spectra of the Cu, C, O and N elements were noticeable with high-resolution scans, the various components of these convoluted spectra could be assigned with the peak fitting routines of the XPS instruments. The binding energies, identification, and the atomic percentages of all identified chemical bonds are reported in Table 5-3.

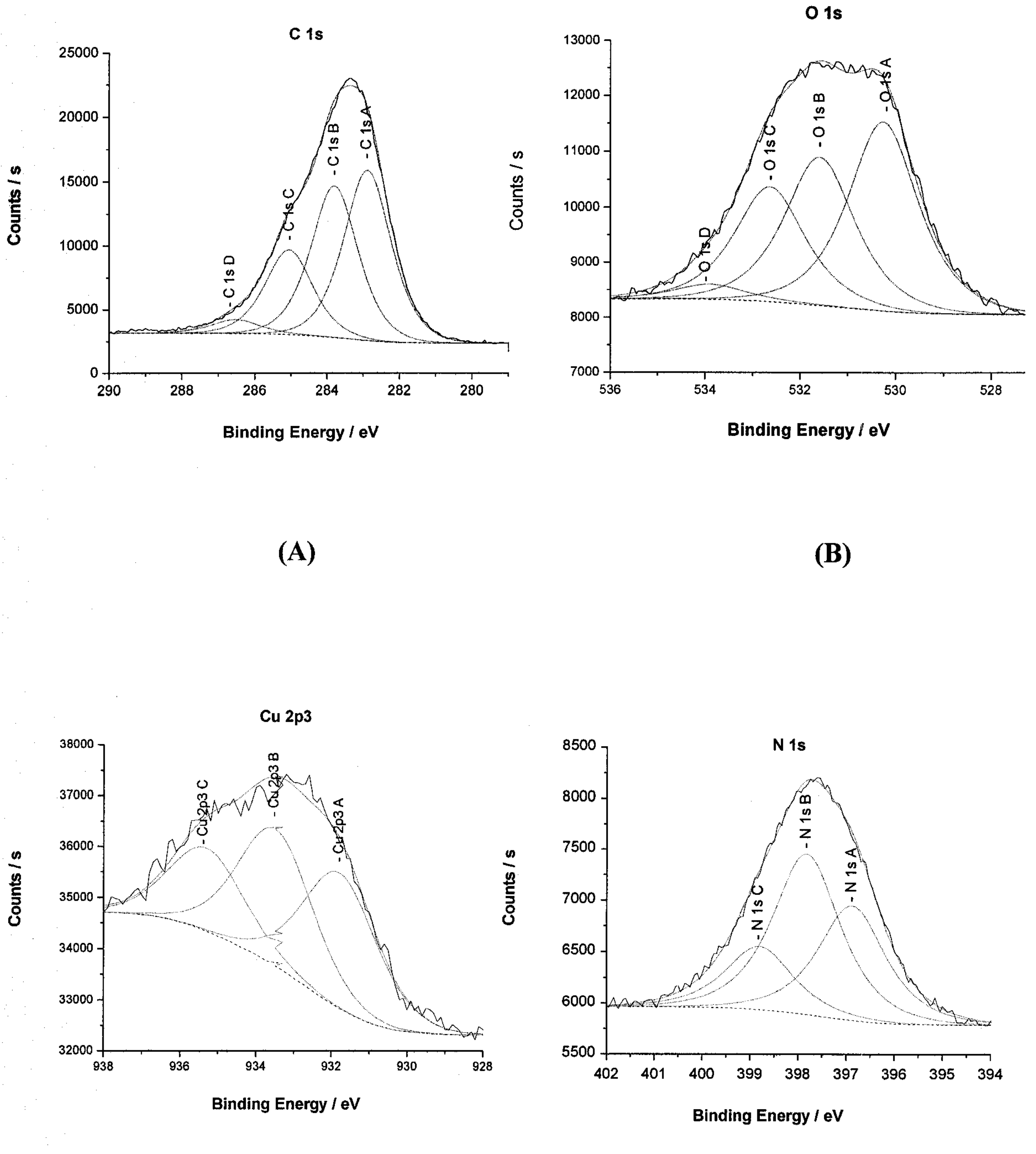

(A)

(B)

(C)

(D)

Figure 5-6. High resolution XPS spectra of C 1s (A), O 1s (B), Cu 2p3 (C) and N 1s (D).

Table 5-3. Binding energies, identification, and atomic percentages of the elements C 1s, O 1s, N 1s and Cu 2p3 obtained by XPS analysis.

Name	Binding Energy (eV)	Identification	Atomic %
C 1s A	282.9	Cu-C	30.7
C 1s B	283.8	Cu-C $(-C=C-)_n$	27.4
C 1s C	285.1	C-C	15.4
C 1s D	286.5	C-O Cu-C-NO	2.5
O 1s A	530.3	O-Cu	5.3
O 1s B	531.6	O-Cu O=C-NH	4.2
O 1s C	532.6	O=C $C-NO_x$	3.3
O 1s D	533.9	O-C	0.4
N 1s A	396.9	N-O	2.1
N1s B	397.8	C=N	2.9
N 1s C	398.8	Cu-C-NH	1.1
Cu 2p3 A	931.8	Cu-C	1.8
Cu 2p3 B	933.5	Cu-O	1.8
Cu 2p3 C	935.3	$Cu-CO_3$ Cu-C-NO Cu-C-O	1.1

It is shown in Table 5-3 that some Cu atoms were oxidized and the rest were bonded to C atoms. A major fraction of the C atoms were bonded to Cu atoms. Another large fraction of the C atoms were bonded to themselves. There is a weak indication that some C atoms were bonded to O and N atoms. For the binding energy of 283.8 eV of the C 1s bond, it is impossible to distinguish between the Cu-C and $(-C=C-)_n$ bonds. However, based on the observations made with the FT-IR spectrum (section 5.3.4.), it can be inferred that most of these C 1s bonds are attributable to Cu-C liaisons, and to a much lesser extent to C=C bonds. The presence of a considerable amount of Cu-C bonds indicates that hydrocarbon radicals created in the plasma react with active sites present at the surface of bare copper nanoparticles. Therefore, it is inferred that chemical bonds are formed between the organic film and the copper nanoparticle's surface.

Since C_2H_6 does not polymerize under normal conditions because of the absence of functional groups, the C_2H_6 molecule has to be dissociated in the CCRF plasma, thus forming free radicals and active molecules such as $\cdot CH_3$, $\cdot CH_2$, $\cdot C_2H_5$ and C_2H_4. These radicals can adsorb onto the copper nanoparticles and react with either gas-phase or neighboring adsorbed free radicals, resulting in the formation of an organic film onto the nanoparticles (and of polymer powders suspended in the gas stream). The weak percentages of atomic bonds involving oxygen and nitrogen indicate that oxygen and nitrogen radicals, formed in the CCRF plasma due to air contamination, also react with the hydrocarbon radicals and the active sites present at the surface of the copper nanoparticles.

It is postulated that the $(CH_x\text{-}CH_y)_z$ configuration is the main structure of the plasma polymer film, and that the C-O-C, C-N-C and C=C configurations are also present in the plasma polymer film, but in a smaller percentages. The organic coating deposited onto the copper nanoparticles has a macromolecular structure, and includes a very small amount of carbon double bonds.

5.4. Study of the mechanism of plasma polymerization

Based on the FT-IR and XPS analyses of the coated copper nanoparticles, it is concluded that the formation and reaction of free radicals in the CCRF ethane plasma play main roles in the plasma polymerization process. Radicals such as $\cdot CH_3$, $\cdot C_2H_3$, $\cdot C_2H_5$ and other hydrocarbon radicals are formed in the gas phase by the collision of high-energy free electrons with hydrocarbon molecules, or at the surface of a substrate exposed to the RF plasma by the adsorption of free radicals and the hydrogen abstraction from the already produced polymer film. The energy required to form free radicals in the plasma volume (~3-4 eV) is much lower than the energy required to form ions (~9-13 eV). Because the average electron energy in low-pressure RF discharge is typically of ~2-5 eV, it is anticipated that radicals are present in a much higher concentration than the ions. Kobayashi et al. [119] estimated that the concentration of free radicals in this kind of plasma is usually five to six orders of magnitude higher than that of the ions. Therefore, the mechanism of plasma polymerization from ethane lies mostly on the generation and reaction of free radicals.

5.4.1. Simple model of plasma polymerization from the ethane monomer

On the basis of the above discussions and the literature, a simplified free-radical mechanism of plasma polymerization is proposed. First, the collision of ethane molecules with either free energetic electrons or hydrogen atoms results in the formation of a considerable amount of free radicals such as $\cdot CH_3$, $\cdot C_2H_3$ and $\cdot C_2H_5$ and active molecules such as C_2H_4 and C_2H_2. The dissociation of C_2H_6 to produce C_2H_4 is more important since this reaction happens more rapidly than other reactions with the present system [92]. C_2H_4 can be further dissociated to produce C_2H_2. The chemical reactions are shown below:

$$e + C_2H_6 \rightarrow C_2H_4 + H_2 + e \tag{5-1}$$

$$e + C_2H_4 \rightarrow C_2H_2 + H_2 + e \tag{5-2}$$

$$e + C_2H_6 \rightarrow 2CH_3 \bullet + e \tag{5-3}$$

$$e + C_2H_6 \rightarrow C_2H_5 \bullet + H \bullet + e \tag{5-4}$$

$$e + C_2H_6 \rightarrow CH_2 \bullet + CH_4 \bullet + e \tag{5-5}$$

$$e + H_2 \rightarrow 2H \bullet + e \tag{5-6}$$

$$H \bullet + C_2H_4 \rightarrow C_2H_5 \bullet \tag{5-7}$$

$$H \bullet + C_2H_2 \rightarrow C_2H_3 \bullet \tag{5-8}$$

The formation of free radicals and active molecules can also happen at the plasma polymer surface exposed to the plasma through hydrogen abstraction of the organic bonds and the absorption of free radicals such as $\cdot CH_3$, $\cdot C_2H_3$ and $\cdot C_2H_5$. These surface reactions are shown below:

$$H\bullet + M(s) \rightarrow R(s) + H_2 \tag{5-9}$$

$$CH_3\bullet(g) + S \rightarrow CH_3\bullet(s) \tag{5-10}$$

$$C_2H_3\bullet(g) + S \rightarrow C_2H_3\bullet(s) \tag{5-11}$$

$$C_2H_5\bullet(g) + S \rightarrow C_2H_5\bullet(s) \tag{5-12}$$

where (*g*) and (*s*) denote the species in gas phase and on particle surface, respectively. *M*, *R* and *S* represent a gas molecule, a free radical and a particle surface, respectively.

For the reactor pressure (1~20 torr) used in the present study, the diffusion and adsorption of free radicals and active molecules onto the particle surface is expected to predominate over the gas-phase recombination between them [88]. So, the heterogeneous formation of plasma polymers onto the particle surface happens dominantly. The addition of C_2H_4 and C_2H_2 molecules to the free radicals present at the copper nanoparticle surface leads to the growth of plasma polymer films. These free radicals include $\cdot CH_3$, $\cdot C_2H_3$, $\cdot C_2H_5$ and other high-molecular-weight radicals. The chemical reactions happening onto the particle surface are shown below [92]:

$$C_2H_4(g) + CH_3\bullet(s) \rightarrow R_1(s) \tag{5-13}$$

$$C_2H_4(g) + C_2H_3\bullet(s) \rightarrow R_2(s) \tag{5-14}$$

$$C_2H_4(g) + C_2H_5\bullet(s) \rightarrow R_3(s) \tag{5-15}$$

$$C_2H_2(g) + CH_3\bullet(s) \rightarrow R_4(s) \tag{5-16}$$

$$C_2H_2(g) + C_2H_3\bullet(s) \rightarrow R_5(s) \tag{5-17}$$

$$C_2H_2(g) + C_2H_5 \bullet (s) \rightarrow R_6(s) \qquad (5\text{-}18)$$

The addition of C_2H_2 to a surface free radical can lead to the formation of C=C bonds in the plasma polymer film, while the addition of C_2H_4 will form only C-C bonds. Most active C_2H_4 molecules react directly with the free radicals, resulting in the formation of more C-C bonds than C=C bonds. The active C_2H_4 and C_2H_2 molecules also react with free radicals in the gas phase, thus generating longer radicals, which can be adsorbed onto the copper nanoparticle surface thus forming plasma polymer films. In parallel, they also can be used towards the gas phase synthesis of polymer powders.

Therefore, the mechanism of plasma polymerization from ethane with the present reactor system can be described as the dissociation of ethane to produce ethylene, acetylene and free radicals and the addition of ethylene and acetylene to the adsorbed or generated free radicals at the copper nanoparticle's surface.

5.4.2. Explanation for the "characteristic map"

The simplified free-radical mechanism of plasma polymerization from ethane can provide an explanation for the "characteristic map" presented in section (5.3.3.). Basically, the concentration of free radicals and other active species in CCRF ethane plasmas depends on the operating conditions, such as the RF power, reactor pressure, and the inert gas flow rate. The increase in RF power leads to an increase in the concentration of active molecules and free radicals; whereas inverse relationships are expected between reactor pressure and the concentration of active molecules and free radicals as well as between the argon flow rate and the concentration of active molecules and free radicals. As the RF power level is increased, the density of high-energy electrons increases, thus intensifying the dissociation of hydrocarbon molecules and increasing the production of active molecules and free radicals. When the pressure is increased, both the energy and density of electrons decrease [98], resulting in lower active molecules and radical production yields. When the argon flow rate is increased at constant C_2H_6 flow rate, the residence time and concentration of the active molecules and free radicals are reduced. So, as it is shown in Figure 5-3 (A), the concentrations of the reactive species are kept at similar levels in each operating curve, thus producing continuous solid films on the copper nanoparticle surface.

5.5. Summary

In this chapter, the preparation of copper nanoparticles of size ranging from several nm to ~50 nm and coated with a 3~10 nm-thick organic film in a dual-plasma process making use of a pulsed metal vapor arc source and an in-flight capacitively-coupled RF plasma polymerization source has been demonstrated. The plasma polymer film has a macromolecular structure and contains a small fraction of C=C bonds. The film is hydrophobic and is chemically adsorbed onto the surface of copper nanoparticle.

A "characteristic map" for the deposition of an organic layer by plasma polymerization from ethane onto copper nanoparticles has been developed. The concentration and reaction of free radicals and active molecules, which both depend on the operating conditions, plays an important role in the formation of the plasma polymer coating.

Chapter 6

Further experiments

6.1 Experimental considerations

Since the cathodic arc evaporation/condensation reactor is quite universal with respect to the choice of the metal material and the plasma polymerization process can be performed from a wide range of organic monomers, the dual-plasma process and reactor assembly developed in this Ph.D. project are supposed to be versatile enough to accommodate other metal sources and gaseous organic monomers. In order to confirm the versatility of this dual-plasma reactor and extend its applications with other metal and organic monomer sources, further experiments were carried out on the basis of the experience gained from the arc evaporation of copper and the plasma polymerization from ethane.

6.1.1. Synthesis of uncoated and coated iron and aluminum nanoparticles

Further experiments with other metal sources such as iron and aluminum were performed. Iron (McMaster-Carr, 99% purity in the present study) and aluminum rods (McMaster-Carr, 99% purity in the present study) of dimensions similar to the copper ones were used. The experimental conditions were also similar: argon flow rate of 400 sccm, ethane flow rate of 2 sccm, reactor pressure of approximately 10 torr, RF plasma power of 60 W, and 30 minutes duration. Uncoated metal nanoparticles were synthesized first and then, coated ones with plasma polymerization from ethane.

6.1.2. Plasma polymerization from ethylene glycol (EG) vapors

Metal nanoparticles have a useful application as dispersed phase in nanofluids. Common host fluids for such applications include deionized water and ethylene glycol (EG). The preparation of nanofluids requires low agglomeration of nanoparticles and the formation of even and stable suspension of nanoparticles. These requirements can be achieved with the surface modification of nanoparticles before they are dispersed in the liquid phase. In practice, the preparation of the surface-functionalized metal nanoparticle suspensions in EG is being carried out in our laboratory. The laboratory-scale process used by the plasma group researchers combines a cathodic arc evaporation/condensation source for the synthesis of metal nanoparticles with an hybrid (plasma-liquid) down-flow CCRF reactor for the in-flight coating and in-situ dispersion of the metal nanoparticles into the host fluid (i.e. EG). The present experiments aimed at studying the feasibility of using EG vapors as a monomer source for the plasma polymerization of a coating onto the metal nanoparticles. EG is a low-vapor pressure, mildly polar solvent. It is believed that the plasma polymerization from EG will lead to the deposition of a coating onto the metal nanoparticle that will enhance the dispersibility of the nanoparticles into EG. EG, which is in the liquid form under normal conditions, was introduced into the system by the use of an argon flow (200 sccm) bubbling through a reservoir of EG, as shown in Figure 6-1.

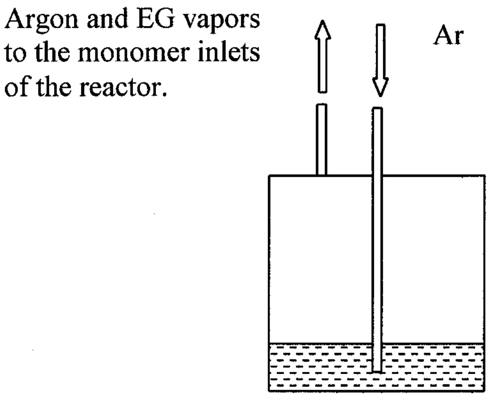

Figure 6-1. Schematic of the EG injector.

The reactor pressure was maintained around 8 torr. Preliminary experiments at low RF power levels (<60 W) led to a dimmed and unstable RF plasma. The RF power level was set to 80 W from then on. Copper rods were used as the metal source. The experiments lasted 30 minutes.

6.2. Morphology of uncoated and coated iron and aluminum nanoparticles

Consistent with common knowledge [45], the breakdown voltage of the inter-electrode gap did not change significantly when aluminum and iron rods were used instead of copper ones. Representative TEM images of uncoated and coated (with plasma polymer from ethane) iron and aluminum nanoparticles are shown in Figure 6-2.

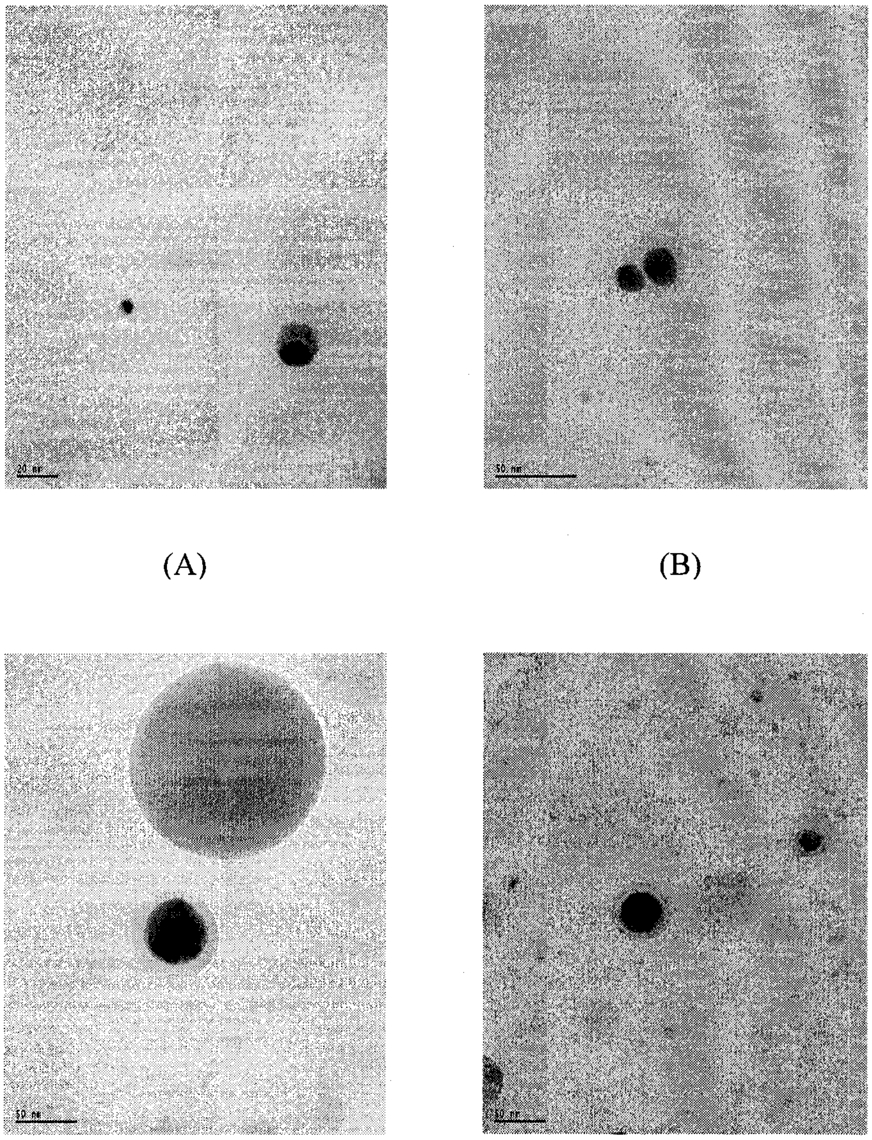

(A) (B)

(C) (D)

Figure 6-2. TEM images of uncoated and coated iron and aluminum nanoparticles. (A) uncoated Fe nanoparticles, (B) uncoated Al nanoparticles, (C) coated Fe nanoparticles, (D) coated Al nanoparticles.

As it can be seen, the appearance of iron and aluminum nanoparticles shows little differences with the coated Cu nanoparticles. The diameter of these nanoparticles is under 50 nm, and some nanoparticles have a spherical shape, while some have an irregular shape. The TEM images also reveal a thin translucent film (~6 nm in thickness) deposited onto the metal nanoparticles. Organic powders are also formed as co-products. These results indicate that the cathodic arc evaporation/condensation reactor can be used to produce metal nanoparticles from various metal sources, including copper, iron and aluminum, with sizes lower than 50 nm.

6.3. Morphology of copper nanoparticles coated from EG vapors

A TEM image of copper nanoparticles coated from EG vapors is shown in Figure 6-3.

Figure 6-3. TEM image of a copper nanoparticle (small nanoparticle on the left) coated from EG vapors. The nanoparticle is agglomerated with a macroparticle.

It can be seen that the coating is thicker than the plasma polymer film obtained from the ethane monomers, and that the EG coating does not have a uniform structure. It appears like as an agglomerate of tiny particles. Finally, both the ethane and EG monomer sources seem to produce a coating that completely covers the metal nanoparticles.

6.4. Summary

The additional experiments reveal that uncoated and coated (with ethane plasma polymer) iron and aluminum nanoparticles can be synthesized with the dual-plasma reactor, and that plasma polymerization from EG vapors can be achieved. The morphology of the produced uncoated and coated iron and aluminum nanoparticles is similar to the one of copper nanoparticles. The plasma polymer film from EG vapors completely encapsulates the copper nanoparticles, though its morphology is different from the plasma polymer obtained with ethane. These results confirm that the dual-plasma reactor can be generally used to produce coated metal nanoparticles with organic films from a wide range of metal and organic monomer sources.

Chapter 7

Conclusions and recommendations for future work

7.1. Conclusions

7.1.1. A novel dual-plasma process

The main contribution of this PhD project is the development of a novel dual-plasma process for the synthesis of metal nanoparticles coated with a thin organic layer. The process combines a pulsed arc evaporation/condensation process for the production of metal nanoparticles with in-flight plasma polymerization of an organic layer onto the produced metal nanoparticles. The combination of the two processes inside a single vacuum chamber avoids the contamination of the metal nanoparticles by the environment and enables the control of the product chemistry.

A wide range of metal sources can be used as the raw cathode and metal nanoparticle precursor. Similarly, various organic gas monomers can be used to generate different kinds of plasma polymer films. Furthermore, the results showed that the morphology of the metal nanoparticles is controlled solely by the experimental parameters associated with the pulsed arc evaporation reactor, while the properties of the plasma polymer films depend on several of the operating parameters. The main parameters that couple the two processes are the reactor pressure and inert gas flow rate, which needed to be optimized in order to accommodate both processes' requirements.

7.1.2. Copper nanoparticles coated with plasma polymer films

Most of the experiments reported in this thesis concentrated on the synthesis of copper nanoparticles coated with ultrathin organic films obtained from the plasma polymerization of the ethane monomer. Other metal sources such as iron and aluminum as well as another organic monomer source (ethylene glycol vapors) have also been studied, but to a lesser extent. The important conclusions obtained from this research project are summarized below.

- The size of the produced copper nanoparticles ranges from several nanometers to 50 nm, and the thickness of organic films obtained from plasma polymerization of the ethane monomer ranges from 3 to 10 nm. The metal nanoparticles have a crystalline structure, while the organic films have a macromolecular structure as showed with a FT-IR analysis of the coating. The plasma polymer produced from ethane is hydrophobic, in agreement with the fact that the monomer source does not contain polar groups. It was evidenced with the XPS analysis probing approximately 5 nm inside the coated nanoparticles that the organic coating is chemically bonded to the metal nanoparticle surface. When ethylene glycol vapors were used as the organic monomer source, the generated plasma polymer films were thicker and showed a rougher surface than the plasma polymer films obtained with the ethane monomer.
- The mean size of the produced metal nanoparticle is influenced mainly by the reactor pressure. It was demonstrated that low reactor pressures (below 20 torr) lead to the production of small copper nanoparticles. The argon flow rate has little influence on the mean size, but higher gas flow rates (about 2000 sccm) seem to lead to the production of smaller metal nanoparticles and to the broadening of the particle size distribution. Additionally, the metal macroparticle production rate increased with increasing pulsed arc current.
- The actual outcome of plasma polymerization from the ethane monomer strongly depends on reactor pressure, RF power level, and inert gas flow rate. A "characteristic map" has been developed to elucidate the relationship between the operating conditions and the product of plasma polymerization. In this particular study, the reactor pressure range covered the pump limit (~8 mtorr) to 20 torr, RF power levels of 40 to 100 W, and inert gas flow rates of 200 to 800 sccm.
- A simplified free-radical mechanism for the plasma polymerization from ethane has been proposed based on the characterization of the plasma polymers and the

literature. This mechanism qualitatively explains the operating curves traced in the "characteristic map".

7.2. Recommendations for future work

The cathodic arc evaporation/condensation process could also be used to synthesize metal alloy nanoparticles. Since metal nanoparticles made of copper, iron or aluminum have been synthesized with the use of pure cathode metals, it is most probable that alloy nanoparticles can be produced in the cathodic arc evaporation reactor with some kind of alloy used as the cathode metal source. Then, extensive studies on different cathode metal sources from pure metals to alloys could be performed in the cathodic arc evaporation reactor.

The erosion rate of cathode materials is known to be a strong function of reactor pressure in the range from 0.1 torr to atmospheric pressure, which ranges covers the pressure conditions used in the present study. The relationship that exists between these parameters should be characterized in a future work.

In the present reactor design, the inter-electrode gap (~1 mm) is smaller than the steady-state radius of the metallic plasma expansion. This causes a considerable metal ions/atoms deposition on the inside surface of the anode tube. Therefore, increasing the inter-electrode gap could lead to an increase of the production rate of metal nanoparticles for the same operating conditions.

It should be noted that macroparticles were also found mixed with the nanoparticles, although the use of a pulsed arc power supply strongly attenuates the production of macroparticles in the cathodic arc evaporation process. The elimination of macroparticles from the condensed metal nanoparticles needs to be further studied.

It was evidenced that the structure and morphology of the produced metal nanoparticles are only dependent on the arc evaporation parameters, but the formation process is still poorly understood. Modeling the generation of metal nanoparticles using the present experimental conditions could shed some light on the mechanism of formation of metal nanoparticles.

A detailed study of the plasma polymerization from the ethane monomer should be performed, including a characterization of the reactive species present in the CCRF plasma, their residence times, and chemical reactions amongst active species. Characterization techniques such as optical emission or laser absorption spectroscopy, and gas chromatography could be employed to determine the species in the plasma. Since the residence time of radicals and other active species in the plasma is very short, the development of a chemical kinetics model would be useful in exploring the plasma polymerization process.

Abbreviations and symbols used

C	capacitance of the (high-voltage) capacitor (F)
	sound velocity of the background gas (m s^{-1})
CCD	charge-coupled device (camera)
CCRF	capacitively-coupled radio frequency (plasma)
d^*	critical size for a stable nucleus (m)
DC	direct current (discharge)
DLC	diamond-like carbon (coating)
E_r	vacuum erosion rate (μg C^{-1})
EG	ethylene glycol
FE-SEM	field emission scanning electron microscopy
FT IR	Fourier-transform infrared spectroscopy
HMDSO	hexamethyldisiloxane
i	current in the discharging circuit loop (A)
k	Boltzmann's constant (1.380658×10^{-23} J)
L	inductance of the inductor (H)
LED	light-emitting diode (display)
M	gas molecule
M_g	atomic mass of the background gas (kg)
MW	microwave (discharge)
R	free radical
R_1	resistor in the charging circuit loop (Ω)
R_2	ballast resistor in the discharging circuit loop (Ω)
R_c	Steady-state radius of the metallic plasma (m)
R(t)	radius of the expanding metallic plasma
RF	radio frequency (discharge)
S	vapor saturation ratio
S	particle surface
sccm	standard cubic centimeters per minute (cm^3 min^{-1})

T_e	electron temperature (K)
T_g	gas temperature (K)
T_i	ion temperature (K)
TEOS	tetraethyloxysilane
TEM	transmission electron microscopy
torr	pressure unit (1 torr = 133.32 Pa)
V_0	vacuum expansion velocity of the metallic plasma ($m\ s^{-1}$)
V_B	breakdown voltage of the inter-electrode (V)
XPS	X-ray photoelectron spectroscopy
ρ_g	mass density of the background gas ($kg\ m^{-3}$)
σ	surface tension of the nucleus ($N\ m^{-1}$)
τ_c	plasma expansion time (s)
υ	monomer volume of metal vapors (m^3)

References

1. L. Lee, G. Seddon and F. Stephens. Stained glass. 1976, New York: Crown.
2. O. Deparis, P. G. Kazansky, A. Podlipensky, A. Abdolvand, G. Seifert and H. Graener. Novel technique for engineering the structural and optical properties of metal-doped nanocomposite. *Ninth Annual Symposium of IEEE/LEOS Benelux Chapter*. 2004. University of Ghent, Belgium.
3. D. L. Feldheim and C. A. Foss, Jr. Metal nanoparticles: synthesis, characterization and application. 2002, New York: Marcel Dekker.
4. A. D. Pomogailo and V. N. Kestelman. Metallopolymer nanocomposites. 2005, Berlin: Springer.
5. A. Ermoline, M. Schoenitz, E. Dreizin and N. Yao, Production of carbon-coated aluminum nanopowders in pulsed microarc discharge. *Nanotechnology*, 2002. **13**, p. 638.
6. R. Elghanian, J. J.Storhoff, R. C. Mucic, R. L. Letsinger and C. A. Mirkin. Selective colorimetric detection of polynucleotides based on the distance-dependent optical properties of gold nanoparticles. *Science*. 1997, **277**, p. 1078.
7. P. V. Kamat. Photophysical, photochemical and photocatalytic aspects of metal nanoparticles. *J. Phys. Chem.* B, 2002, **106**, p. 7729-7744.
8. M. -P. Pileni. Magnetic fluids: fabrication, magnetic properties, and organization of nanocrystals. *Adv. Funct. Mater.* 2001, **11**, p. 323.
9. P. Keblinski, S. R. Phillpot, S. U. S. Choi and J. A. Eastman. Mechanisms of heat flow in suspensions of nano-sized particles (nanofluids). *Int. J. Heat Mass Transfer.* 2002, **45**, p. 855.
10. L. Nicolais and G. Carotenuto. Metal-polymer nanocomposites. 2005, Hoboken, New Jersey: John Wiley & Sons, Inc.
11. M. C. Roco, C. L. Bai, H. J. Fissan, J. Schoonman, C. Hayashi and M. Oda. Reviews of national research programs in nanoparticle and nanotechnology research. *J. Aerosol Sci.* 1998, **29**, p. 749-760.

12. T. Appenzeller. The man who dared to think small. (Richard Feynman) (Includes excerpts from his talk on Dec. 29, 1959 "Engineering a small world: from atomic manipulation to microfabrication"). *Science*. 1991, **257**, p. 1300-1302.

13. F. E. Kruis, H. Fissan and A. Peled. Synthesis of nanoparticles in the gas phase for electronic, optical and magnetic application - a Review. *J. Aerosol Sci.* 1998, **29**, p. 511.

14. M. T. Swihart. Vapor-phase synthesis of nanoparticles. *Curr. Opin. Colloid Interface Sci.* 2003, **8**, p. 127.

15. C. B. Murray, C. R. Kagan and M. G. Bawendi. Synthesis and characterization of monodisperse nanocrystals and close-packed nanocrystal assemblies. *Annu. Rev. Mater. Sci.* 2000, **30**, p. 545-610.

16. T. Trindade, P. O'Brien and N. L. Pickett. Nanocrystalline semiconductors: synthesis, properties, and perspectives. *Chem. Mater.* 2001, **13**, p. 3843-3858.

17. A. Henglein. Colloidal Palladium Nanoparticles: Reduction of Pd(II) by H_2; $Pb_{core}Au_{shell}Ag_{shell}$ Particles. *J. Phys. Chem.* B, 2000, **104**, p. 6683-6685.

18. Y. Sun and Y. Xia. Shape-controlled synthesis of gold and silver nanoparticles. *Science*. 2002, **298**, p. 2176.

19. P. -L. Kuo and W. -F. Chen. Formation of silver nanoparticles under structured amino groups in pseudo-dendritic poly(allylamine) derivatives. *J. Phys. Chem.* B, 2003, **107**, p. 11267-11272.

20. D. Farrell, S. A. Majetich and J. P. Wilcoxon. Preparation and characterization of monodisperse Fe nanoparticles. *J. Phys. Chem.* B, 2003, **107**, p. 11022-11030.

21. V. F. Puntes, K. M. Krishnan and A. P. Alivisators. Colloidal nanocrystal shape and size control: the case of cobalt. *Science*. 2001, **291**, p. 2115-2117.

22. T. Sato, T. Ichikawa, T. Ito, Y. Yonezawa, K. Kadono, T. Sakaguchi and M. Miya. Nonlinear optical properties of silver sols prepared by photoreduction method. *Chem. Phys. Lett.* 1995, **242**, p. 310-314.

23. B. Cheng, R. Zhu, Z. -Y. Chen and W. -Q. Jiang. Ultrafine cobalt particles immobilized on styrene/acrylic acid copolymer particles by ultraviolet irradiation. *J. Mater. Sci. Lett.* 1999, **18**, p. 1859-1860.

24. M. Mostafavi, N. Keghouche and M. -O. Delcourt. Complexation of silver clusters of a few atoms by a polyanion in aqueous solution: pH effect correlated to structural changes. *Chem. Phys. Lett.* 1990, **169**, p. 81-84.

25. A. Henglein, B. G. Ershov and M. Malow. Absorption spectrum and some chemical reactions of colloidal platinum in aqueous solution. *J. Phys. Chem.* 1995, **99**, p. 14129-14136.

26. K. Wegner, B. Walker, S. Tsantilis and S. E. Pratsinis. Design of metal nanoparticles synthesis by vapor flow condensation. *Chem. Eng. Sci.* 2002, **57**, p. 1753-1762.

27. W. Mahoney and R. P. Andres. Aerosol synthesis of nanoscale clusters using atmospheric arc evaporation. *Mater. Sci. Eng.* A, 1995, **204**, p. 160-164.

28. T. M. Ayers, J. L. Fye, Q. Li and M. A. Duncan. Synthesis and isolation of titanium metal cluster complexes and ligand-coated nanoparticles with a laser vaporization flowtube reactor. *J. Cluster Sci.* 2003, **14**, p. 97-113.

29. A. Harano, K. Shimada, T. Okubo and M. Sadakata, Crystal phase of TiO_2 ultrafine particles prepared by laser ablation of solid rods. *J. Nanoparticle Res.* 2002, **4**, p. 215-219.

30. W. Marine, L. Patrone, B. Luk'yanchuk and M. Sentis. Strategy of nanocluster and nanostructure synthesis by conventional pulsed laser ablation. *Appl. Surf. Sci.* 2000, **154-155**, p. 345-352.

31. H. Hahn and R. S. Averback. The production of nanocrystalline powders by magnetron sputtering. *J. Appl. Phys.* 1990, **67**, p. 1113-1115.

32. F. K. Urban III, A.Hosseini-Tehrani, P. Griffiths, A. Khabari, Y. -W. Kim and I. Petrov. Nanophase films deposited from a high-rate, nanoparticle beam. *J. Vacuum Sci. Technol.* B, 2002, **20**, p. 995-998.

33. S. Schwyn, E. Garwin and A. Schmidt-Ott. Aerosol generation by spark discharge. *J. Aerosol Sci.* 1988, **19**, p. 639.

34. A. P. Weber, M. Seipenbusch and G. Kasper. Application of aerosol techniques to study the catalytic formation of methane on gasborne nickel nanoparticles. *J. Phys. Chem.* A, 2001, **105**, p. 8958-8963.

35. L. Rao, N. K. Reddy, S. Coulombe, J. -L. Meunier and R. J. Munz. Carbon nanotubes as nanoparticles collector. *J. Nanoparticle Res.* 2007, **9**, p. 689-695.

36. M. H. Magnusson, K. Deppert and J. -O. Malm. Single-crystalline tungsten nanoparticles produced by thermal decomposition of tungsten hexacarbonyl. *J. Mater. Res.* 2000, **15**, p. 1564-1569.

37. A. G. Nasibulin, P. P. Ahonen, O. Richard, E. I. Kauppinen and I. S. Altman. Copper and copper oxide nanoparticles formation by chemical vapor nucleation from copper (II) acetylacetonate. *J. Nanoparticle Res.* 2001, **3**, p. 385-400.

38. J. H. Kim, T. A. Germer, G. W. Mulholland and S. H. Ehrman. Size-monodisperse metal nanoparticles via hydrogen-free spray pyrolysis. *Adv. Mater.* 2002, **14**, p. 518-521.

39. K. Haneda, Z. X. Zhou and A. H. Morrish. Low-temperature stable nanometer-size fcc-Fe particles with no magnetic ordering. *Phys. Rev.* B, 1992, **46**, p. 13832-13838.

40. A. Bapat, C. R. Perrey, S. A. Campbell, C. B. Carter and U. Kortshagen. Synthesis of highly oriented, single-crystal silicon nanoparticles in a low-pressure, inductively coupled plasma. *J. Appl. Phys.* 2003, **94**, p. 1969-1974.

41. K. L. Klug, V. P. Dravid and D. L. Johnson. Silica-encapsulated magnetic nanoparticles formed by a combined arc evaporation/chemical vapor deposition technique. *J. Mater. Res.* 2003, **18**, p. 988.

42. D. Vollath and D. V. Szabó, Coated nanoparticles: a new way to improved nanocomposites. *J. Nanoparticle Res.* 1999, **1**, p. 235.

43. B. Jüttner. Cathode spots of electric arcs. *J. Phys. D: Appl. Phys.* 2001, **34**, p. R103-R123.

44. S. Coulombe and J. -L. Meunier. Arc-cold cathode interactions: parametric dependence on local pressure. *Plasma Sources Sci. Technol.* 1997, **6**, p. 508-517.

45. R. L. Boxman, D. M. Sanders and P. J. Martin. Handbook of vacuum arc science and technology: fundamentals and applications. 1995, New Jersey: Park Ridge: Noyes Publications.

46. T. H. Lee and A. Greenwood. Theory for the cathode mechanism in metal vapor arcs. *J. Appl. Phys.* 1961, **32**, p. 916-923.

47. J. -L. Meunier and S. Coulombe. Cold cathode arc attachment: the importance of the high local pressure. *Pure Appl. Chem.* 1998, **70**, p. 1175-1180.

48. C. W. Kimblin. Cathode spot erosion and ionization phenomena in the transition from vacuum to atmospheric pressure arcs. *J. Appl. Phys.* 1974, **45**, p. 5235-5244.

49. P. R. Emtage. Interaction of the cathode spot with low pressure of ambient gas. *J. Appl. Phys.* 1975, **46**, p. 3809-3816.

50. M. G. Drouet and J. -L. Meunier. Influence of the background gas pressure on the expansion of the arc-cathode plasma. *IEEE Trans. Plasma Sci.* 1985, **PS-13**, p. 285-287.

51. J. -L. Meunier and M. G. Drouet. Experimental study of the effect of gas pressure on arc cathode erosion and redeposition in He, Ar, and SF_6 from vacuum to atmospheric pressure. *IEEE Trans. Plasma Sci.* 1987, **PS-15**, p. 515-519.

52. J. -L. Meunier. Pressure limits for the vacuum arc deposition technique. *IEEE Trans. Plasma Sci.* 1990, **18**, p. 904-910.

53. J. -L. Meunier. Cathodic arc carbon plasma/gas interaction in fullerenes synthesis study. *J. Appl. Phys.* 1999, **85**, p. 1992-1994.

54. V. I. Rakhovskii. Experimental study of the dynamics of cathode spots developments. *IEEE Trans. Plasma Sci.* 1976, **PS-4**, p. 81-102.

55. J. Vyskočil and J. Musil. Arc evaporation of hard coatings: process and film properties and film properties. *Surf. Coat. Technol.* 1990, **43-44**, p. 299-311.

56. J. E. Daalder. Erosion and origin of charged and neutral species in vacuum arcs. *J. Phys. D: Appl. Phys.* 1975, **8**, p. 1647-1659.

57. D. T. Tuma, C. L. Chen and D. K. Davies. Erosion products from the cathode spot region of a copper vacuum arc. *J. Appl. Phys.* 1978, **49**, p. 3821-3831.

58. J. E. Daalder. Cathode spots and vacuum arcs. *Physica,* 1981, **104C**, p. 91-106.

59. C. W. Kimblin. Erosion and ionization in the cathode spot regions of vacuum arcs. *J. Appl. Phys.* 1973, **44**, p. 3074-3081.

60. J. E. Jenkin, J. C. Sherman, R. Webster and R. Holmes. Measurement of the neutral vapour density decay following the extinction of a high-current vacuum arc between copper electrodes. *J. Phys. D: Appl. Phys.* 1975, **8**, p. L139-L143.

61. A. Anders. Approaches to rid cathodic arc plasmas of macro- and nanoparticles: a review. *Surf. Coat. Technol.* 1999, **120-121**, p. 319-330.

62. B..Jüttner. Erosion craters and arc cathode spots in vacuum. *Beiträge aus der Plasmaphysik.* 1979, **19**, p. 25-48.

63. G. W. McClure. Plasma expansion as a cause of metal displacement in vacuum-arc cathode spots. *J. Appl. Phys.* 1974, **45**, p. 2078-2084.

64. K. Keutel, H. Fuchs and C. Edelmann. The influence of the operation parameters on the properties of thin films produced by a modified pulsed arc process. *Appl. Phys. A.* 2004, **78**, p. 687-690.

65. M. Büschel and W. Grimm. Influence of the pulsing of the current of a vacuum arc on rate and droplets. *Surf. Coat. Technol.* 2001, **142-144**, p. 665-668.

66. B. Engers, H. Fuchs, J. Schultz, E. Hettkamp and H. Mecke. Comparison of substrate temperature and deposition rate between modified pulsed arc process and d.c. arc process. *Surf. Coat. Technol.* 2000, **133-134**, p. 121-125.

67. S. L. Girshick, C. -P. Chiu and P. H. McMurry. Modelling particle formation and growth in a plasma systhesis reactor. *Plasma Chem. Plasma Process.* 1988, **8**, p. 145-157.

68. S. L. Girshick and C. -P. Chiu. Homogeneous nucleation of particles from the vapor phase in thermal plasma synthesis. *Plasma Chem. Plasma Process.* 1989, **9**, p. 355-369.

69. F. F. Abraham. Homogeneous nucleation theory: the pretransition theory of vapor condensation. 1974, New York: Academic Press.

70. V. Haas, R. Birringer, H. Gleiter and S. E. Pratsinis. Synthesis of nanostructured powers in an aerosol flow condenser. *J. Aerosol Sci.* 1997, **28**, p. 1443.

71. S. K. Friedlander. The behavior of constant rate aerosol of reactors. *Aerosol Sci. Technol.* 1982, **1**, p. 3-13.

72. G. Callies, H. Schittenhelm, P. Berger and H. Hügel. Modeling of the expansion of laser-evaporated matter in argon, helium and nitrogen and the condensation of clusters. *Appl. Surf. Sci.* 1998, **127-129**, p. 134-141.

73. D. Bauerle. Laser processing and chemistry. 2000, Berlin: Springer.

74. Z. Pászti, Z. E. Horváth, G. Petõ, A. Karacs and L. Guczi. Pressure dependent formation of small Cu and Ag particles during laser ablation. *Appl. Surf. Sci.* 1997, **109-110**, p. 67-73.

75. B. S. Luk'yanchuk, W. Marine and S. I. Anisimov. Condensation of vapor and nanoclusters formation within the vapor plume, produced by ns-laser ablation of Si. *Laser Phys.* 1998, **8**, p. 291-302.

76. T. Ohkubo, M. Kuwata, B. Luk'yanchuk and T. Yabe. Numerical analysis of nanocluster formation within ns-laser ablation plume. *Appl. Phys. A.* 2003, **77**, p. 271-275.

77. D. B. Geohegan, A. A. Puretzky, G. Duscher and S. J. Pennycook, Time-resolved imaging of gas phase nanoparticle synthesis by laser ablation. *Appl. Phys. Lett.* 1998, **72**, p. 2987-2989.

78. H. Yasuda. Plasma polymerization. 1985, Orlando, Florida: Academic Press Inc.

79. P. W. Kramer, Y.-S.Yeh and H. Yasuda, Low temperature plasma for the preparation of separation membranes. *J. Membrane Sci.* 1989, **46**, p. 1-28.

80. D. Shi, S. X. Wang, W. J. van Ooij, L. M. Wang, J. Zhao and Z. Yu, Uniform deposition of untrathin polymer films on the surfaces of Al_2O_3 nanoparticles by a plasma treatment. *Appl. Phys. Lett.* 2001, **78**, p. 1243-1245.

81. A. Kouprine, F. Gitzhofer, M. Boulos and A. Fridman. Polymer-like C:H thin film coating of nanopowders in capacitively coupled RF discharge. *Plasma Chem. Plasma Process.* 2004, **24**, p. 189.

82. A. Kouprine, F. Gitzhofer, M. Boulos and T. Veres. Synthesis of ferromagnetic nanopowders from iron pentacarbonyl in capacitively coupled RF plasma. *17th International Symposium on Plasma Chemistry*. 2005. Toronto, Canada.

83. H. Vora and T. J. Moravec. Structural investigation of thin film of diamondlike carbon. *J. Appl. Phys.* 1981, **52**, p. 6151-6157.

84. A. Vanhulsel, J. -P. Ceils, E. Dekempeneer, J. Meneve, J. Smeets and K. Vercammen. Inductively coupled r.f. plasma assisted chemical vapor deposition of diamond-like carbon coatings. *Diam. Relat. Mater.* 1999, **8**, p. 1193-1197.

85. J. C. S. Fernandes, M. G. S. Ferreira, D. B. Haddow, A. Goruppa, R. Short and D. G. Dixon. Plasma-polymerized coatings used as pre-treatment for aluminum alloys. *Surf. Coat. Technol.* 2002, **154**, p. 8-13.

86. G. Akovali. Plasma polymerization of ethane and some properties of PP ethane as a protective coat. *J. Appl. Polym Sci.* 1986, **32**, p. 4027-4042.

87. H. Hiratsuka, G. Akovali, M. Shen and A. T. Bell. Plasma polymerization of some simple saturated hydrocarbons. *J. Appl. Ploym. Sci.* 1978, **22**, p. 917.

88. J. M. Tibbitt, R. Jensen, A. T. Bell and M. Shen. A model for the kinetics of plasma polymerization. *Macromolecules*, 1977, **10**, p. 647.

89. H. Kobayashi, A. T. Bell and M. Shen, Plasma polymerization of saturated and unsaturated hydrocarbons. *Macromolecules*, 1974, **7**, p. 277.

90. H. Kobayashi, M. Shen and A. T. Bell. Effects of reaction conditions on the plasma polymerization of ethylene. *J. Macromol. Sci. -Chem.* A, 1974, **8**, p. 373-391.

91. R. J. Jensen, A. T. Bell and D. S. Soong. Plasma polymerization of ethane. I. experimental studies of effluent gas composition and polymer deposition rates. *Plasma Chem. Plasma Process.* 1983, **3**, p. 139.

92. R. J. Jensen, A. T. Bell and D. S. Soong. Plasma polymerization of ethane. II. theoretical analysis of effluent gas composition and polymer deposition rates. *Plasma Chem. Plasma Process.* 1983, **3**, p. 163.

93. I. Géraud-Grenier, V. Massereau-Guibaud and A. Plain. Characterization of particulates and coatings created in a 13.56 MHz RF methane plasma. *Surf. Coat. Technol.* 2004, **187**, p. 336.

94. A. Grill. Cold plasma in materials fabrication: from fundamentals to application. 1994, New York: The Institute of Electrical and Electronic Engineers, Inc.

95. L. S. Polak and Y. A. Lebedev. Plasma Chemistry. 1998, Cambridge, UK: Cambridge International Science Publishing.

96. H. Yasuda. Luminous chemical vapor deposition and interface engineering. 2005, New York: Marcel Dekker.

97. V. M. Lelevkin, D. K. Otorbaev, D. C. Schram. Physics of non-equilibrium plasma. 1992, Amsterdam: North-Holland.

98. J. R. Hollahan and A. T. Bell. Techniques and applications of plasma chemistry. 1974, New York: John Wiley & Sons, Inc.

99. R. R. Manory, U. Carmi, R. Avni and A. Grill, A comparative study of silicon deposition from $SiCl_4$ in cold plasma using argon, H_2 or $Ar+H_2$. *Thin Solid Films.* 1988, **156**, p. 79-92.

100. N. Mutsukura, S. -I. Inoue, Y. Machi. Deposition mechanism of hydrogenerated hard-carbon films in a CH_4 rf discharge plasma. *J. Appl. Phys.* 1992, **72**, p. 43-53.

101. M. Niinomi, H. Kobayashi, A. T. Bell and M. Shen, Morphology of plasma-polymerized ethylene. *J. Appl. Phys.* 1973, **44**, p. 4317-4321.

102. P. Canepa, G. Castello, S. Munari and M. Nicchia. RF plasma polymerization of ethane in a flow low pressure system. *Rad. Phys. Chem.* 1982, **19**, p. 49-55.

103. A. Kouprine. Thin film coating of nano-particles in a capacitively coupled RF discharge. Ph.D. thesis. 2003, University of Sherbrooke: Sherbrooke.

104. F. Aristizabal. Modelling of the generation of ultra fine aluminum particles from the quench of superheated vapour in turbulent flow. M.Eng. thesis. 2002, McGill University: Montreal.

105. A. Tariq. Design and implementation of a plasma enhanced chemical vapour deposition (PEVCD) system for the study of C_{60}-polymer composite films and surface functionalization effects on C_{60}. M.Eng. thesis. 2004, McGill University: Montreal.

106. D. M. Mattox. Handbook of physical vapor deposition (PVD) processing: film formation, adhesion, surface preparation and contamination control. 1998, Westwood: Noyes publications

107. G. Auday, P. Guillot, J. Galy and H. Brunet. Experimental study of the effective secondary emission coefficient for rare gases and copper electrodes. *J. Appl. Phys.* 1998, **83**, p. 5917-5921.

108. J. D. Cobine. Gaseous Conductors: Theory and Engineering Applications. 1st ed. 1941, New York: McGraw-Hill.

109. S. Ramo, J. R. Whinnedry and T. Van Duzer. Fields and waves in communication electronics. 2nd ed. 1984, New York: Wiley.

110. J. R. Roth. Industrial plasma engineering. Vol. 1: Principles. 1995, Bristol and Philadelphia: Institute of Physics Publishing.

111. B. Jüttner. Formation time and heating mechanism of arc cathode craters in vacuum. *J. Phys. D: Appl. Phys.* 1981, **14**, p. 1265-1275.

112. S. Coulombe and J. -L. Meunier. Theoretical prediction of non-thermionic arc cathode erosion rate including both vaporization and melting of the surface. *Plasma Sources Sci. Technol.* 2000, **9**, p. 239-247.

113. O. R. Monteiro and A. Anders. Vacuum-Arc-Generated Macroparticles in the Nanometer Range. *IEEE Trans. Plasma Sci.* 1999, **27**, p. 1030.

114. G. Cao. Nanostructure & Nanomerials: synthesis, properties & application. 2004, London: Imperial College Press.

115. H. Kersten, H. Deutsch, E. Stoffels, W. W. Stoffels, G. M. W. Kroesen and R. Hippler. Micro-Disperse Particles in Plasma: From Disturbing Side Effects to New Applications. *Contrib. Plasma Phys.* 2001, **41**, p. 598.

116. B. Jüttner. Characterization of the cathode spot. *IEEE Trans. Plasma Sci.* 1987, **PS-15**, p. 474-480.

117. S. Stoykov and C. Eggs and U. Kortshagen. Plasma chemistry and growth of nanosized particles in a C_2H_2 RF discharge. *J. Phys. D: Appl. Phys.* 2001, **34**, p. 2160-2173.

118. J. F. Watts and J. Wolstenholme. An introduction to surface analysis by XPS and AES. 2003, Chichester: John Wiley & Sons Ltd.

119. H. Kobayashi, M. Shen and A. T. Bell. Role of halogens in plasma polymerization of hydrocarbons. *J. Macromol. Sci. -Chem.* A, 1974, **8**, p. 1345-1360.